



HAL
open science

Modelling of suspended particle transport and deposition in saturated porous media

Enze Ma

► **To cite this version:**

Enze Ma. Modelling of suspended particle transport and deposition in saturated porous media. Civil Engineering. Normandie Université, 2018. English. NNT : 2018NORMLH42 . tel-04560092

HAL Id: tel-04560092

<https://theses.hal.science/tel-04560092>

Submitted on 26 Apr 2024

HAL is a multi-disciplinary open access archive for the deposit and dissemination of scientific research documents, whether they are published or not. The documents may come from teaching and research institutions in France or abroad, or from public or private research centers.

L'archive ouverte pluridisciplinaire **HAL**, est destinée au dépôt et à la diffusion de documents scientifiques de niveau recherche, publiés ou non, émanant des établissements d'enseignement et de recherche français ou étrangers, des laboratoires publics ou privés.



Normandie Université

THÈSE

Pour obtenir le diplôme de DOCTORAT

Spécialité : Génie Civil

Préparée au sein de Normandie Université Le Havre

**Modélisation du transport et du dépôt de particules en suspension
dans un milieu poreux saturé**

**Modelling of suspended particle transport and deposition in
saturated porous media**

**Présentée et soutenue par
MA Enze**

**Thèse soutenue publiquement le 29 01 2018
devant le jury composé de**

Mme. KACEM Mariem	Maître de Conférences HDR – École Nationale d'Ingénieurs de Saint-Étienne	Rapporteur
Mme. SAIYOURI Nadia	Professeur des Universités – Université Bordeaux 1	Rapporteur
Mme. JIA Yun	Maître de Conférences – Université de Lille 1	Examinateur
M. SMAOUI Hassan	Directeur de recherche, CEREMA	Examinateur
M. OUAHBI Tariq	Maître de Conférences – Normandie Université Le Havre	Encadrant
M. WANG Huaqing	Professeur des Universités – Normandie Université Le Havre	Directeur de thèse

Thèse dirigée par M.WANG Huaqing, LOMC, UMR CNRS 6294



Remerciements

Cette thèse s'inscrit dans le projet SAHNKARST (Fonctionnement et vulnérabilité des systèmes aquifères de Haute Normandie) de la Structure Fédérative de Recherche SCALE du Grand Réseau de Recherche TERRA. Le travail présenté dans ce mémoire a été réalisé à l'Université du Havre Normandie au sein du Laboratoire Ondes et Milieux Complexes (LOMC), UMR 6294 CNRS.

Je tiens à remercier en premier lieu mon directeur de thèse, M. WANG Huaqing, pour l'aide précieuse et la confiance qu'il m'a accordé durant ces années de thèse. Je souhaiterais également exprimer toute ma gratitude au M. OUAHBI Tariq, je le remercie de m'avoir encadré, orienté, aidé et conseillé. Je suis particulièrement reconnaissant à M. AHFIR Nasre-Dine et M. ALEM Abdellah de l'intérêt qu'ils ont manifesté à l'égard de cette recherche.

Je tiens à remercier Mme. KACEM Mariem et Mme. SAIYOURI Nadia pour avoir consacré de leur temps pour rapporter sur le mémoire de cette thèse. J'aimerais remercier également Mme. JIA Yun et M. SMAOUI Hassan pour avoir accepté de faire partie de ce jury de thèse comme examinateurs.

Particulièrement je tiens à exprimer toute ma reconnaissance à Mme. JIA Yun pour ses bienveillantes recommandations et son appui pour décrocher cette thèse.

Je n'oublie pas tous mes ami(e)s ABBAR Bouamama, Ruonan BAI, HAMMADI Ahmed, KAJEIOU Meriem, LIU Wei, SONG Yue, TIAN Yue, ZHOU Zhibin, ZONG Kun.

Enfin, mes plus profonds remerciements vont à mes parents. Tout au long de mon cursus, ils m'ont toujours soutenu, encouragé et aidé. Ils ont su me donner toutes les chances pour réussir. Qu'ils trouvent, dans la réalisation de ce travail, l'aboutissement de leurs efforts ainsi que l'expression de ma plus affectueuse gratitude.

Table of contents

Résumé étendu en français.....	1
Introduction	5
Chapter 1 Theories of Particle Transport and Fate in Porous Media	9
1.1 Occurrence of subsurface groundwater.....	9
1.1.1 The zone of aeration	10
1.1.2 Different types of geological formations of the saturated zone	10
1.2 Porous medium	13
1.3 Flow in porous medium.....	17
1.4 Particle transport	18
1.5 Filtration in porous media.....	24
1.5.1 Different types of filtration	24
1.5.2 Particle retention sites	25
1.5.3 Particle – collector interaction model	26
1.5.4 Collision mechanisms and single collector model	29
1.5.5 Experiments under favorable and unfavorable deposition conditions	32
1.5.6 Deposition and re-entrainment dynamics under unfavorable deposition conditions.....	35
1.6 Conclusions and research objectives	42
Chapter 2 Transport deposition reentrainment model and numerical simulation.....	47
2.1 Transport, deposition and re-entrainment model	47
2.2 Analytic and Numerical solutions for 1D convection-dispersion equation	51
2.2.1 Analytic solution of convection dispersion equation	52
2.2.2 Numerical solution of convection dispersion equation.....	53
2.3 Numerical solutions of transport and deposition problems	63
2.4 Optimization scheme for identification of model parameters.....	64
2.4.1 Numerical Implementation	66
2.5 Inverse method algorithm.....	68
2.5.1 Program testing	68
2.6 Summary	72
Chapter 3 Modelling of particle transport, deposition and reentrainment.....	73
3.1 Pulse-input injection of Latex colloids.....	75
3.1.1 Materials and experimental methods	75
3.1.2 Mathematical model	77

3.1.3	Results	79
3.1.4	Mechanisms of Retention and Reentrainment in Flow Stagnation Zone.....	83
3.1.5	Effects of Hydrodynamic Forces	84
3.1.6	Effects of Particle Size	85
3.1.7	Interplay of Different-Sized Particles Retention.....	87
3.1.8	Conclusions.....	89
3.2	Step-input injections of kaolinite suspension	91
3.2.1	Materials and experimental methods	91
3.2.2	Mathematical Model.....	93
3.2.3	Results	96
3.2.4	The deposition dynamics parameters	101
3.2.5	Temporal and spatial evolution of the deposition rate.....	107
3.2.6	Conclusions.....	112
	Conclusions and perspectives	113
	Conclusions	113
	Perspectives	115
	References	117
	Indices	i
	List of figures	i
	List of tables	iii
	List of publications	v
	Journal publications:	v
	Conferences presentations:	v
	Poster presentations:	v

Résumé étendu en français

La compréhension des mécanismes de transport et de dépôt de particules dans les milieux poreux présente un intérêt important dans de nombreux domaines, tels que la contamination des eaux souterraines et l'assainissement des sols.

Pour maîtriser les risques liés à l'environnement et à la santé humaine, la prédiction du transport des particules dans le sol est nécessaire. Fréquemment, l'eau souterraine est utilisée sans traitement grâce à l'action filtrante due à son écoulement à travers les milieux poreux (sols, matériaux aquifères...). Néanmoins, Il a toutefois été reconnu que certaines bactéries et certains virus peuvent parcourir des distances considérables dans les aquifères et les sols saturés, ce qui peut constituer une menace non négligeable pour la contamination des eaux de surface et des aquifères. Des recherches considérables dans ce domaine ont été menées, notamment sur la compréhension des effets des facteurs physiques, chimiques et biologiques sur le transport, la propagation et l'impact des bactéries et des virus sur les eaux souterraines.

Les particules en suspension peuvent faciliter le transport des contaminants, qui sont adsorbés sur les surfaces des particules, dans les eaux souterraines. Les mécanismes facilitant le transport d'un large éventail de contaminants par les particules ont été étudiés, y compris les radionucléides, les hydrocarbures, les métaux lourds et les pesticides. Ces dernières années, les recherches menées sur les mécanismes facilitant la mobilité des contaminants se sont focalisées sur l'étude des effets de l'exclusion de taille et sur le co-transport de particules contaminées. Concernant les effets de l'exclusion de taille, la vitesse des particules peut être considérablement augmentée, jusqu'à 5 fois par rapport à la vitesse de l'eau interstitielle. Les contaminants associés aux particules peuvent se propager beaucoup plus rapidement et sur une longue distance dans les milieux poreux. La recherche sur le co-transport de particules contaminées comprend la modélisation de l'augmentation de la

mobilité des contaminants et la réduction des temps de séjour des contaminants. Une meilleure compréhension des mécanismes de transport des particules est nécessaire.

Dans ce travail, des modèles modifiés basés sur le modèle général de transport-dépôt-relargage ont été développés et appliqués à la simulation numérique d'expériences en colonnes de laboratoire. Ces modèles numériques ont permis d'étudier les effets de différents facteurs sur le comportement de transport de particules dans différents milieux poreux.

Des expériences d'injection instantanée de suspension de particules de latex artificiel ont été modélisées dans la première partie de ce travail. Les simulations numériques du modèle de couplage transport-dépôt ont été réalisées avec des coefficients cinétiques de dépôt et de relargage constants. Cela a permis de caractériser la dynamique de rétention et de relargage dans différentes conditions hydrodynamiques pour des particules de latex mono-disperses (de diamètre 3, 10 et 16 μm) et poly-disperses (mélange des trois populations mono-disperses 3, 10 ou 16 μm).

Les résultats montrent qu'une augmentation importante de la vitesse du fluide ne provoque pratiquement aucune diminution notable de la rétention en présence de grandes barrières énergétiques ($> 2000 kT$). Des augmentations systématiques des coefficients cinétiques de dépôt et de relargage ont été observées avec la vitesse du fluide et/ou la taille des particules. L'augmentation du cinétique de dépôt irréversible indique que le blocage mécanique (straining et wedging) domine le dépôt dans cette étude. Lors de l'injection de la suspension de particules poly-disperses (mélange des trois populations mono-disperses 3, 10 ou 16 μm) une rétention excessive des particules de taille 3 μm a été observée. Cela peut être expliqué par le fait que les particules plus grosses (10 et 16 μm) déposées peuvent gêner le relargage des plus petites particules (3 μm) à proximité du contact grain-grain et peuvent fournir des sites de fixation supplémentaires à ces particules.

Dans la seconde partie de ce travail, des expériences d'injection continue de particules de kaolinite naturelles ont été modélisées. Un modèle de dépôt dépendant de la distance de parcours des particules a été développé pour

étudier les effets des forces hydrodynamiques sur le transport et le dépôt de particules poly-disperses et l'évolution dans l'espace et dans le temps des cinétiques de dépôt. Les résultats obtenus montrent que le bocage mécanique (straining) et l'hétérogénéité de la population de particules jouent un rôle important dans la distribution décroissante, avec la profondeur, du coefficient cinétique de dépôt.

Des simulations numériques ont été appliquées sur une série d'expériences de colonnes de laboratoire. Différentes vitesses de fluides et trois milieux poreux de granulométries différentes ont été considérées. Les effets des forces hydrodynamiques ont été analysés à partir des variations des paramètres de dépôt du modèle proposé. En tenant compte des distributions de la rétention, de la distribution des tailles des particules retenues dans le milieu à différentes profondeurs ainsi que des évolutions spatio-temporelles des coefficients cinétiques de dépôt, les mécanismes de transport et de dépôt des particules poly-disperses ont été expliqués et clarifiés. Les rôles importants de la variation de la distribution granulométrique des populations de particules mobiles et du changement géométrique des porosités du milieu poreux dû à la rétention ont été soulignés.

Introduction

Prediction of particle transport through the subsurface is important for a wide range of environmental and human-health-related risk scenarios. Frequently, groundwater is used without treatment because of the perceived filtering action of solution flow through porous media. It has been recognized, however, that bacteria and viruses can travel considerable distances in aquifers and saturated soils, thus posing a contamination threat to surface waters and well waters. Considerable research has been devoted to understanding the effects of the physical, chemical, and biological factors that control the transport and fate of bacteria and virus in aquatic systems. The factors investigated include solution chemistry [Gannon et al., 1991; Martin et al., 1991; Jewett et al., 1995], cell type [van Loosdrecht et al., 1987a; Gannon et al., 1991], hydrophobic interactions [van Loosdrecht et al., 1987b; Schafer et al., 1998], motility [Camesano and Logan, 1998; Vigeant et al., 2002], surface charge characteristics [Gross et al., 2001], and surface features [Herald and Zottola, 1989; Walker et al., 2004].

Particles can also enhance the transport of dissolved contaminants in groundwater via their sorption onto particle surfaces. Particle-facilitated transport has been studied for a wide range of contaminants including radionuclides, hydrocarbons, heavy metals and pesticides [Denaix et al., 2001; Hammes et al., 2013; Honeyman, 1999; Kersting et al., 1999; Ma et al., 2016; Tang and Weisbrod, 2009; Yin et al., 2010]. On the effects of size exclusion, particle velocity may be drastically enhanced, even up to 5 times relative to the pore water velocity. Dissolved contaminants associated with particles can spread much faster and broadly. Research in particle-contaminant cotransport includes modeling the enhancement of contaminant mobility and reduction of residence times of dissolved contaminants [Corapcioglu and Jiang, 1993; Flury and Qiu, 2008]. Further understanding of particle transport mechanisms are required to predict the risk posed by particle-enhanced transport mechanisms.

Engineered nanoparticles (ENPs), another class of particles, possess unique properties in engineered and environmental systems compared to their micron size counterparts. Transport of ENPs are of significant interest. ENPs are an emerging environmental contaminant. ENPs released from various manufacturing or disposal points, such as landfill and wastewater treatment [Dale et al., 2015; Keller and Lazareva, 2013; Keller et al., 2013], may enter the environment and accumulate in soils and sediments [Keller et al., 2013; Liu and Cohen, 2014; Meesters et al., 2014]. ENPs can be mobilized from the topsoil zone to saturated zone due to infiltration driven by rainfall or irrigation. Prediction of ENP transport in porous media is important for assessing the risk from ENP migration in aquifers and the contamination of wells used for drinking water supply. ENP studies have involved modeling [Cullen et al., 2010; Bai and Li, 2012; Taghavy et al., 2013], pore-scale experiments [May et al., 2012; May and Li, 2013], and column experiments [Liang et al., 2013; Reng and Smith, 2013; Neukum et al., 2014].

The use of ENPs in a variety of subsurface environmental applications, such as water purification, wastewater treatment, and soil and groundwater remediation, has been widely investigated. For example, nano-zero-valent iron (nZVI) particles are injected into the subsurface at contaminated sites for the in-situ reduction of chlorinated solvents in groundwater [Johnson et al., 2013; O'Carroll et al., 2013; Tosco et al., 2014]. This novel approach has been evaluated at both the laboratory [Phenrat et al., 2009; Raychoudhury et al., 2010; Kocur et al., 2013] and pilot field scales [Johnson et al., 2013; Kocur et al., 2014].

This dissertation is presented in three chapters as following:

Chapter 1 presents the detailed literature review on the particle transport and deposition in porous media. The current basic knowledge of subsurface groundwater, water flow and particle transport and deposition processes in porous media is presented in this chapter. Deposition mechanisms under unfavorable conditions are carefully discussed.

Chapter 2 presents 1D dimension transport-deposition-reentrainment model, analytical and numerical solutions as well as optimization algorithm for identification of model parameters.

Chapter 3 presents applications of the transport-deposition-reentrainment model discussed in Chapter 2 to series of column experiments. Pulse-input of monodisperse suspension and step-input of polydisperse suspension experiments are simulated to discuss qualitatively and/or quantitatively the effects of various factors on particle transport and deposition, i.e. hydrodynamics, grain size distribution and particle size.

Chapter 1 Theories of Particle Transport and Fate in Porous Media

1.1 Occurrence of subsurface groundwater

Figure 1.1 shows the general vertical distribution of groundwater. The occurrence of subsurface water can be divided into zones of aeration and saturation by the water table. In the zone of aeration, the interstices are occupied partially by water and partially by air. Yet the zone of saturation consists of interstices totally filled with water. In the aeration zone, the hydraulic pressure is negative, inferior to atmospheric pressure, and expressed as tension. Main direction of fluid stream is vertical on the effects of gravity in the zone. In contrast, the hydraulic pressure is positive, and the stream is mainly horizontal on the effects of water head difference.

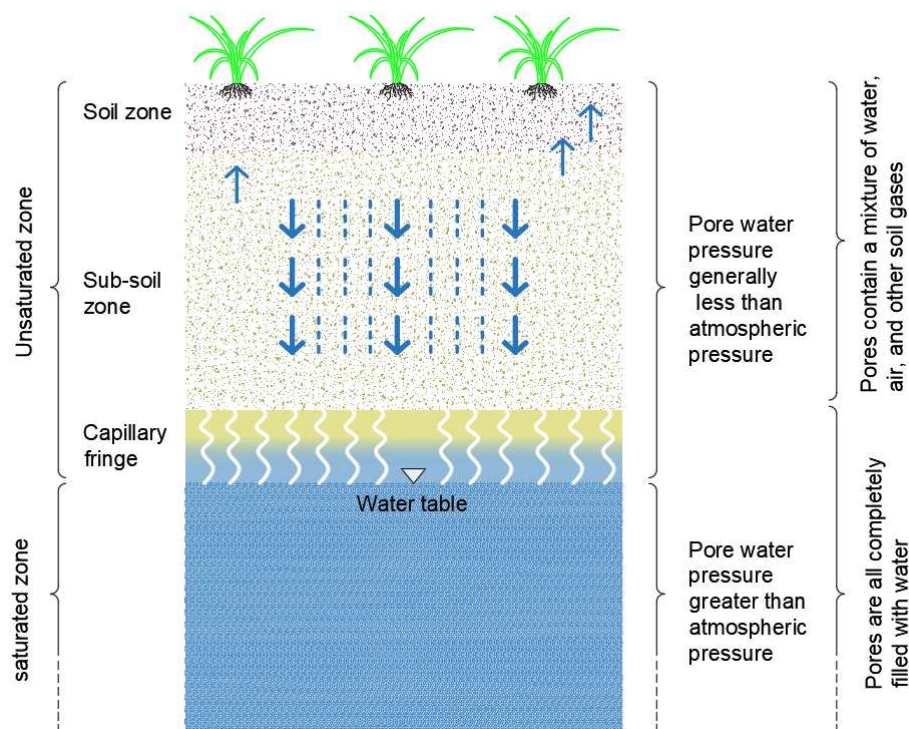


Figure 1.1 *Diagram of generalized divisions of subsurface groundwater*

1.1.1 The zone of aeration

The zone of aeration can be divided into root zone or soil moisture zone, gravitational zone and capillary fringe (Fig. 1.1).

The upper part of the unsaturated zone is called the root zone since the roots of plants can reach the zone. The root zone supports plant growth and has large numbers of living roots, animal and worm burrows and holes left by decayed roots. Except hydraulic equilibrium and soil hydraulic properties, the fluid stream is also affected by root absorption capacity, the surface weather condition as well as evaporation of the plant leaf surface, etc.

Below the root zone lies vadose zone, also called sub-soil zone. Roots cannot reach this zone, and therefore the main factors affecting on the fluid stream are gravity and soil hydraulic properties.

The lower layer of the unsaturated zone is called capillary fringe. In it, groundwater seeps up from a water table and is held in the soil by surface tension and capillarity. The soil is usually saturated, however, the hydraulic pressure is less than atmosphere.

1.1.2 Different types of geological formations of the saturated zone

Aquifers

An aquifer can be described as an underground lay composed of geologic units, such as rock, rock fractures or unconsolidated materials (gravel, sand and silt), that are saturated with water and sufficiently permeable to supply water to water wells. Aquifers have two significant functions: 1) groundwater is transmitted in aquifers from areas of recharge to those of discharge, which is a vital part of the hydrological cycle; 2) an aquifer is a groundwater reservoir which yield a large quantity of clean water up to drinking water quality standards. The amount of water of an aquifer depends on the porosity of materials composing the layer.

Unconfined aquifers

An unconfined aquifer is one in which a water table varies in undulating form

and in slope, depending on areas of recharge and discharge, pumpage from wells, and permeability. Rises and falls in the water table correspond to changes in the volume of water in storage within an aquifer. Figure 1.1 is an idealized section through an unconfined aquifer; the upper aquifer in Figure 1.2 is also unconfined. Contour maps and profiles of the water table can be prepared from elevations of water in wells that tap the aquifer to determine the quantities of water available and their distribution and movement. A special case of an unconfined aquifer involves perched water bodies, as illustrated by Figure 1.2. This occurs wherever a groundwater body is separated from the main groundwater by a relatively impermeable stratum of small areal extent and by the zone of aeration above the main body of groundwater. Clay lenses in sedimentary deposits often have shallow perched water bodies overlying them. Wells tapping these sources yield only temporary or small quantities of water.

Confined aquifers

Confined aquifers, also known as artesian or pressure aquifers, occur where groundwater is confined under pressure greater than atmospheric by overlying relatively impermeable strata. In a well penetrating such an aquifer, the water level will rise above the bottom of the confining bed, as shown by the artesian and flowing wells of Figure 1.2. Water enters a confined aquifer in an area where the confining bed rises to the surface; where the confining bed ends underground, the aquifer becomes unconfined. A region supplying water to a confined area is known as a recharge area; water may also enter by leakage through a confining bed. Rises and falls of water in wells penetrating confined aquifers result primarily from changes in pressure rather than changes in storage volumes. Hence, confined aquifers display only small changes in storage and serve primarily as conduits for conveying water from recharge areas to locations of natural or artificial discharge.

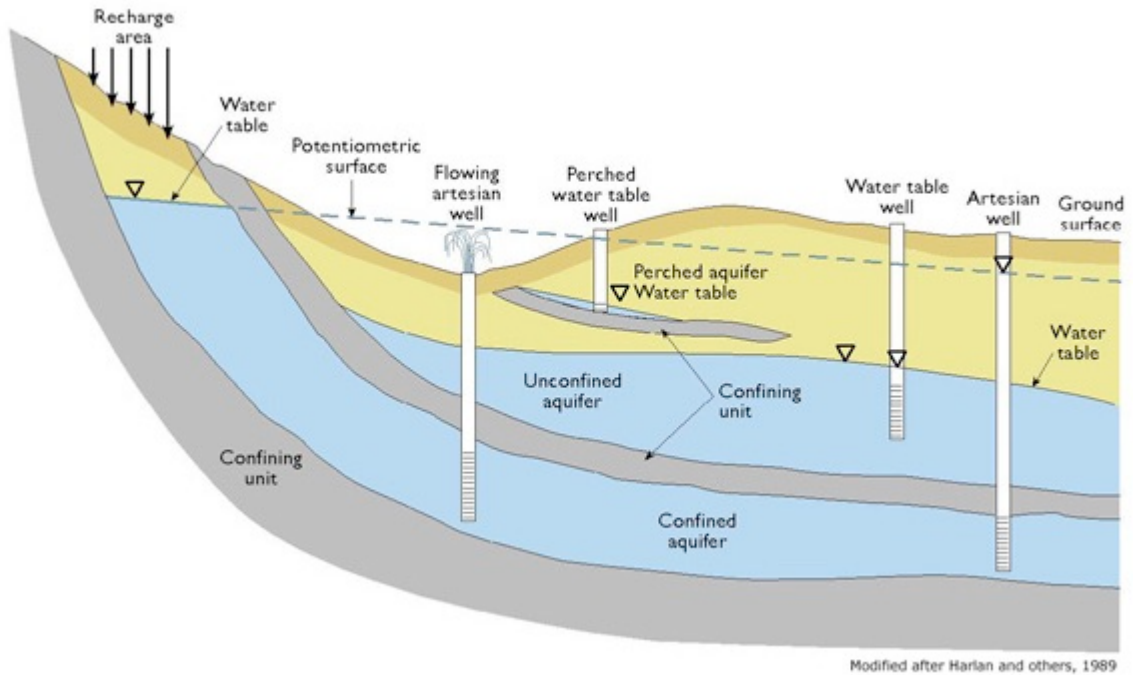


Figure 1.2 Diagram of different types of aquifers (Water Cycle and Fresh Water Supply)

Aquitard

An aquitard is a partly permeable geologic formation. It transmits water at a very slow rate, resulting in the insufficient water yield. Pumping by wells is therefore not possible. For example, sand lenses in a clay formation will form an aquitard.

Aquiclude

An aquiclude is composed of rock or sediment that acts as a barrier to groundwater flow. Aquicludes are made up of low porosity and low permeability rock/sediment such as shale or clay. Aquicludes have normally good storage capacity but low transmitting capacity.

1.2 Porous medium

A porous medium is a solid skeleton material having an empty porous interstitial space. This porous space consists of pores and constrictions (interconnections between the pores). The skeletal portion of the material is often called the "matrix" or "frame". The pores are typically filled with a fluid (liquid or gas).

Porosity

Porosity is defined as the fraction of the volume of voids over the total volume, which is a measure of the void spaces in a material. The value of porosity is between zero and one according to the definition.

Let M be a mathematical point inside the domain occupied by the porous medium. Considering a volume V much larger than a single pore or grain, for which M is at center of the volume, we can write the integral expression of porosity

$$\phi = \frac{1}{V} \int_V \varphi(M) dV \quad (1.1)$$

where $\varphi(M)$ is the indicator function of phase, 0 for solid phase and 1 for void.

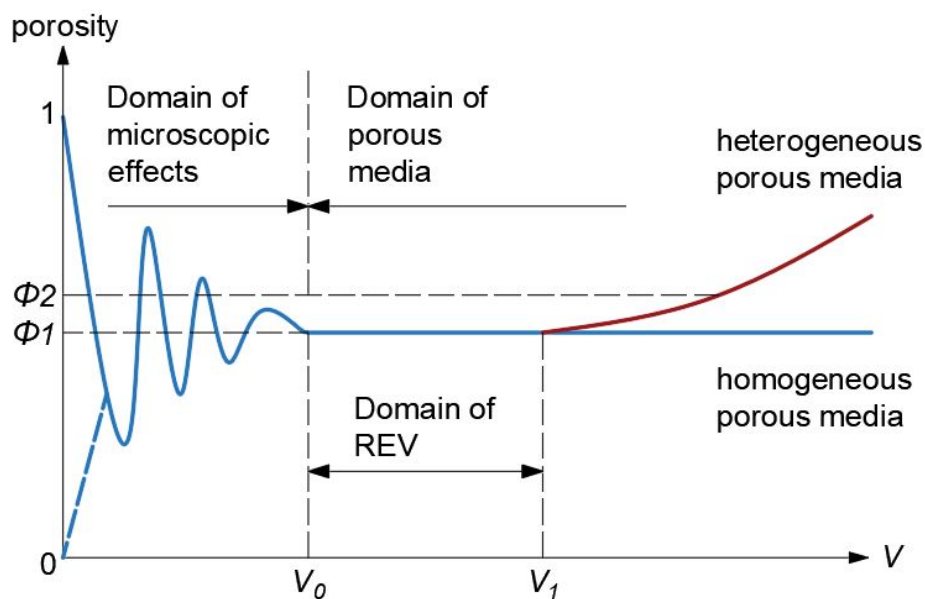


Figure 1.3 Porosity and Representative elementary volume

The evolution of the porosity as the function of V is shown in figure 1.3. For large values of V the porosity may vary gradually as V is reduced, especially when the considered domain is inhomogeneous. Below a certain value of V_1 , these changes or fluctuations tend to decay, leaving only small-amplitude fluctuations that are due to the random distribution of pore sizes in neighborhood of M . However, below a certain value V_0 large fluctuations are suddenly observed. This happens as the dimension of V approach those of a single pore. As V approaches 0, the control volume converging on the mathematical point M , the ratio of voids volume to the total volume will become either one or zero, depending on whether M is inside a pore or inside the solid matrix. Because the control volume with the volume V between V_0 and V_1 has stable and similar porosity, it can be employed as representative elementary volume (REV) to represent the characteristics of the whole porous medium. Porosity can be expressed as: $\phi = \frac{V_v}{V_t}$, where V_v is the volume of voids and V_t is the total volume.

Porosity can be measured by several methods. Strictly speaking, some tests measure the "accessible void", the total amount of void space accessible from the porous medium surface. One of the most widely used methods for measuring the accessible porosity is the so-called gas expansion method in which the porous medium is enclosed in a container filled with a gas such as air. Clearly, the gas only penetrates the accessible void space of the porous medium. The container is then connected to a second evacuated container which causes a change in its pressure. The accessible porosity of the system is then estimated from

$$\phi_A = 1 - \frac{V_1}{V_s} - \frac{V_2}{V_s} \frac{P_f}{P_f - P_i} \quad (1.2)$$

where V_1 is the volume of the container in which the porous system is enclosed, V_2 the volume of the evacuated container, V_s is the volume of the porous sample, and P_i and P_f are, respectively, the initial and final pressures of the medium.

Specific surface area

An important property of a porous medium is its specific surface area (*SSA*), defined as the ratio of the internal surface area of the voids and the bulk

volume of the porous medium that, therefore, is expressed as a reciprocal length. For instance, SSA of the porous medium with uniform particle size (d_p) can be calculated by

$$SSA = \frac{\text{Particle Surface}}{\text{Particle Volume}} = \frac{\pi d_p^2}{\pi \frac{4}{3} \left(\frac{d_p}{2}\right)^3} = \frac{6}{d_p} \quad (1.3)$$

Tortuosity

A third characteristic of a porous medium is its tortuosity τ , which is usually defined as the ratio of the true or total length L_t of the diffusion path of a fluid particle diffusing in the porous medium, and the straight-line distance L between the starting and finishing points of the particle's diffusion, $\tau=L_t/L$ that, by definition, is always greater than (or at least equal to) one.

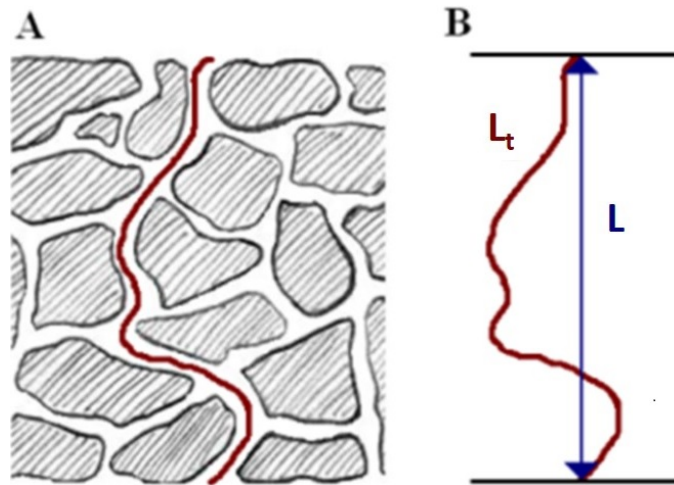


Figure 1.4 *Diagram of porous medium tortuosity.*

Pore size distribution

Like porosity, pore size distribution is another important measure of void space in a porous medium. It is defined as the probability density function that yields the distribution of pore volume by an effective or characteristic pore size. However, this definition is somewhat vague because the pores are interconnected, the volume that one assigns to a pore can be dependent upon both the experimental method and the model of pore space that one employs to interpret the data. Four methods of measuring pore size distributions are mercury porosimetry, sorption experiments, small-angle scattering, and nuclear magnetic relaxation methods. The first two methods have been used extensively, while the latter two are newer and may, under certain conditions,

be more accurate. Mercury porosimetry is a very useful characterization technique for porous materials. Pores between about $500 \mu\text{m}$ and 3.5 nm can be investigated. All instruments assume a cylindrical pore geometry using a modified Young-Laplace equation, which is most of the time referred to as the Washburn equation.

$$\Delta P = \gamma \left(\frac{1}{r_1} + \frac{1}{r_2} \right) = \frac{2\gamma \cos\theta}{r_{\text{pore}}} \quad (1.4)$$

Figure 1.5 display an example of pore size distribution measured by mercury porosimetry.

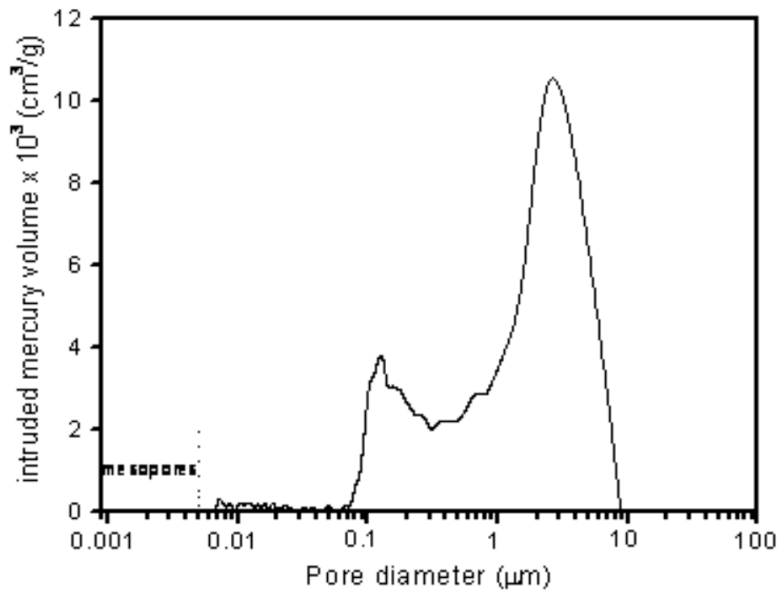


Figure 1.5 Pore size distribution measured by mercury porosimetry (Vieira et al., 2005)

Pores can be divided into two types. The first type is the pore body which occupies most of the void space in the porous medium, and the second is the pore throat, the narrow channel that connects the pore bodies. The size of pore body and pore throat is usually represented by effective radii of a sphere that has the same volume. Thus, pore bodies and pore throats are defined in terms of approximate maxima and minima of the largest-inscribed-sphere radius. The size of pore throats is an important characteristic of porous medium for the relatively large particle filtration, and the related mechanism is called clogging or straining.

1.3 Flow in porous medium

Darcy law

Darcy's law is an equation which describes the fluid flow through a saturated porous medium. When liquid such as water passes through a porous medium, the flow Darcian velocity U is positively correlated to the applied pressure difference in the linear flow case $[L \cdot T^{-1}]$. One derivation of Darcy's law is used widely to determine the flow through permeable media with the following expression:

$$U = \frac{Q}{A} = \frac{k}{\mu} \nabla P \quad (1.5)$$

where U is the Darcy velocity $[L \cdot T^{-1}]$, Q means volumetric flow rate $[L^3 \cdot T^{-1}]$, A is the cross-section area of a porous media $[L^2]$, ∇P is the pressure gradient across the medium in the flow direction $[M \cdot L^{-2} \cdot T^{-2}]$, μ is the viscosity of the flowing fluid $[M \cdot L^{-1} \cdot T^{-1}]$ and k is the intrinsic permeability of the porous medium $[L^2]$. Values of k for natural materials vary widely, for example, typical values for soils are clean gravel 10^{-7} - 10^{-9} m^2 , clean sand 10^{-9} - 10^{-12} m^2 , stratified clay 10^{-13} - 10^{-16} m^2 [Nield and Bejan, 2006]. Besides, Kozeny-Carmen equation provided a relationship between intrinsic permeability (k) and porosity (ϕ) as following [Carman, 1956]:

$$k = \frac{d_g^2}{180} \frac{\phi^3}{(1-\phi)^2} \quad (1.6)$$

where k is linked to the median grain diameter d_g [L] and the porosity ϕ [-]. For a one-dimensional, homogeneous medium, the empiric law of Darcy can be given as:

$$U = -K \frac{\partial H}{\partial x}, \quad H = h + z \quad (1.7)$$

where K is the hydraulic conductivity of a given porous medium $[L \cdot T^{-1}]$, H is the total pressure head [L], h is the pressure head [L], and z is the coordinate or elevation [L].

1.4 Particle transport

Various nonbiological and biological particles exist widely in the subsurface environments, including mineral precipitates, rock and mineral fragments and weathering products, macromolecular components of dissolved organic carbon (such as humic substances) and biocolloids. Figure 1.6 shows size range of kinds of particles present in the groundwater.

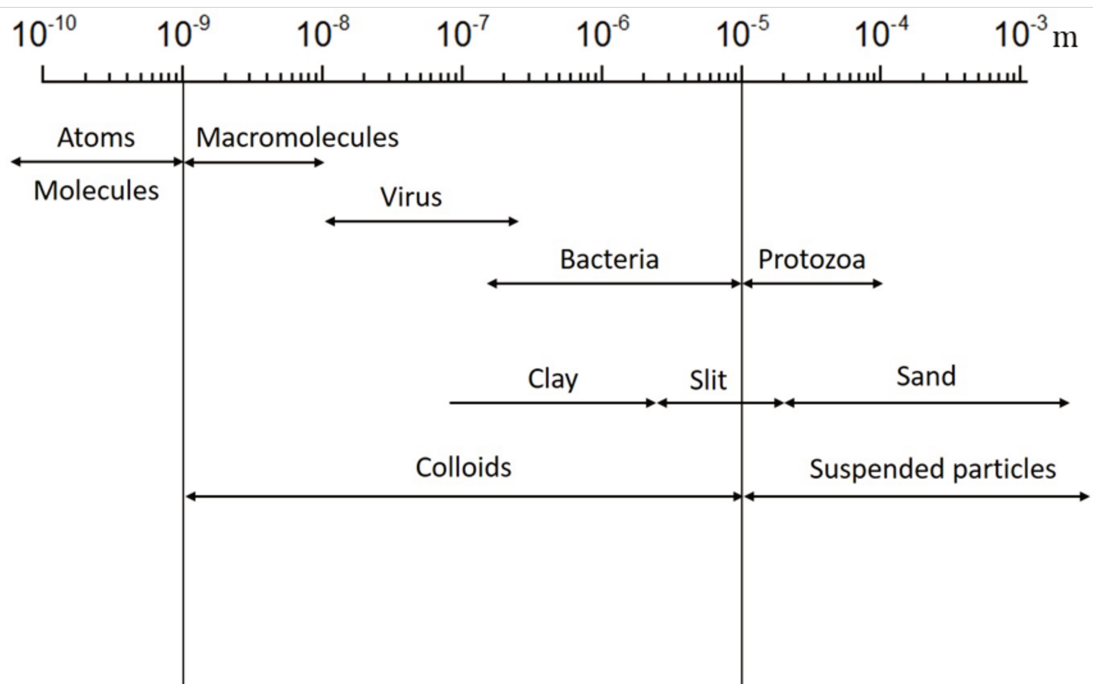


Figure 1.6 Particle size ranges of bio- and nonbiological particles present in groundwater

The particle transport in porous media is assumed to be mainly affected by three physical processes, namely advection, hydrodynamic dispersion and deposition. Hydrodynamic dispersion can be divided into mechanic dispersion and Brownian diffusion.

Convection

Convection is one of the predominant mechanisms for the suspension flow in porous media. It is a process that describes mass transport occurring at the average velocity of the groundwater by the Darcy's law. Only the effective porosity participates in the movement.

Convection can bring about translation of particle populations in the direction of water flow. The convective massive flux is a function of average pore fluid velocity (u), accessible porosity and concentration of solution (C).

$$J_c = UC \quad (1.8)$$

where U [LT^{-1}] is Darcy velocity, J_c [$MT^{-1}L^{-2}$] is the massive convective flux.

Dispersion

In the realm of particle transport in porous media, dispersion, also called hydrodynamic dispersion, includes two parts, molecular diffusion and mechanical dispersion.

Molecular diffusion

Molecular diffusion is the random motion of suspended particles in the fluid resulting from their collisions with the fast-moving molecules in the liquid. It is a physical phenomenon regardless of the fluid velocity. If the concentration of suspended particles in space is not homogeneous, the particles migrate from regions of higher concentrations to regions of lower concentrations. Thus, Fick has established the expression of the diffusive mass flux at the local scale, which is written as:

$$J_d = -\phi D_{mo} \nabla C \quad (1.9)$$

Where D_{mo} [L^2/T] is molecular diffusion coefficient, J_d [$MT^{-1}L^{-2}$] is massive diffusive flux.

The diffusion coefficient D_{mo} can be obtained by the Einstein equation:

$$D_{mo} = \frac{K_B T}{3\pi\mu d_p} \quad (1.10)$$

Where K_B [$L^2MT^{-2}\Theta^{-1}$] is the Boltzman constant; T [Θ] is the temperature; μ [$ML^{-1}T^{-2}$] is fluid viscosity; d_p [L] is particle diameter.

In a saturated porous medium, the mechanism of molecular diffusion is constrained by the geometry of the pores. The expression of the flux resulting from this phenomenon remains of the same form, but D_{mo} is replaced by a

molecular diffusion coefficient, called effective diffusion coefficient, D^* which is defined by:

$$D^* = D_{mo}\psi \quad (1.11)$$

Where D^* [L^2/T] is the effective diffusion coefficient and ψ [-] is a factor related to the tortuosity of the porous medium.

Mechanical dispersion

Due to the microstructure of the medium, the fluid velocity varies in magnitude and direction within the porous medium. This variation in velocities leads to a dilution of the suspension, called mechanical dispersion, which manifests in all directions, but mainly in the direction of flow (longitudinal or axial dispersion). The main causes of kinematic dispersion, illustrated in Figure 1.7, are:

- The existence of parabolic velocity profiles during the passage of particles within the pores. The friction causes a maximum velocity at the center of the pore while the velocity is zero on the walls of the pore (Figure 1.7a).
- Difference of apertures and path lengths results in a difference in average propagation velocities from one pore to another (Figure 1.7b).
- The locally different paths which are long (tortuosity) with respect to the direction of the average speed (Figure 1.7c).
- Variable pore geometry results in different speeds. The orientations of the mean pore axes result in a lateral distribution of the path lines (Figure 1.7d).

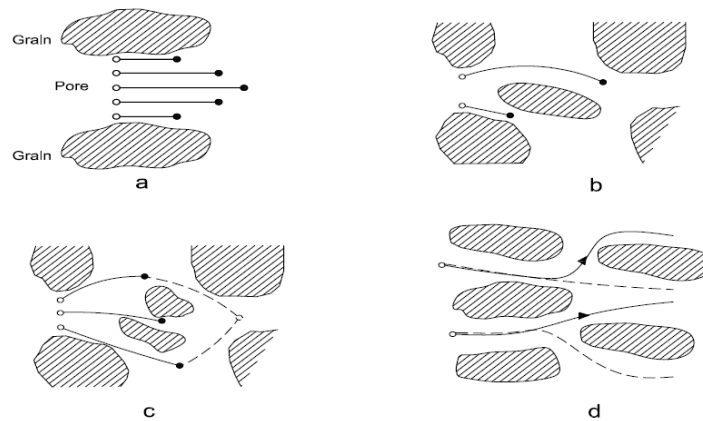


Figure 1.7 Diagram of different types of mechanical dispersion in porous media

In the porous medium, the dispersive transfer can be expressed by a law analogous to the Fick's law;

$$J_m = -\phi D' \nabla C \quad (1.12)$$

where J_m is massive mechanical dispersion flux, D' is the diffusion coefficient matrix.

Hydrodynamic dispersion

In practice, diffusive and dispersive phenomena (molecular diffusion and mechanical dispersion) are often grouped into a single term. They are generally described together by a diffusion law of Fick with a common dispersion coefficient $D_{\text{Type equation here.}}$, called the hydrodynamic dispersion coefficient, which groups together the kinematic dispersion coefficient and the molecular diffusion coefficient:

$$\begin{cases} D_L = D'_L + D_L^* \\ D_T = D'_T + D_T^* \end{cases} \quad (1.13)$$

where D_L and D_T are the longitude and transversal hydrodynamic dispersion coefficients.

In the common range of pore velocity in laboratories and fields, a linear dependence of the kinematic dispersion coefficient with respect to the modulus of the effective velocity is allowed:

$$\begin{cases} D'_L = \alpha_L u \\ D'_T = \alpha_T u \end{cases} \quad (1.14)$$

where α_L and α_T are the longitude and transversal dispersivity.

Therefore the dispersive massive flux therefore can be expressed as:

$$J_h = J_d + J_m = -\phi D \nabla C \quad (1.15)$$

Peclet Number

A Péclet number is a dimensionless number that can characterize the effects of convection and dispersion or diffusion on particle transport. The number of Péclet is defined by:

$$N_{pe} = \frac{ul}{D} \quad (1.16)$$

where l is a characteristic length of the porous medium, which can be represented by grain diameter or pore size. D is dispersive coefficient.

When the Peclet number is very small, the convection-dispersion equation reduces to a diffusion equation. In contrast, if it tends to infinity, convection transport prevails over diffusion transport.

Dispersion regimes

A variety of Péclet number definitions can be found in literature. There are two used to quantify the dispersion regimes. When D equals to D_L' , it is dynamic Peclet number (N_{pe}^{dyn}). As D equals to D^* , it is diffusive Peclet number (N_{pe}^{dif}).

In this context, five mixing regimes that correspond to variable distributions between the roles played by molecular diffusion and kinematic dispersion are defined (Fig. 1.8):

- Regime I: pure molecular diffusion. In this area the dispersion is controlled by molecular diffusion.
- Regime II: the effect of molecular diffusion is of the same order of magnitude as that of mechanical dispersion.
- Regime III: predominant kinematic dispersion. But molecular diffusion cannot be neglected because it reduces the effects of mechanical dispersion.

- Regime IV: pure kinematic dispersion. The effect of molecular diffusion becomes negligible.
- Regime V: zone outside the domain of validity of the law of Darcy.

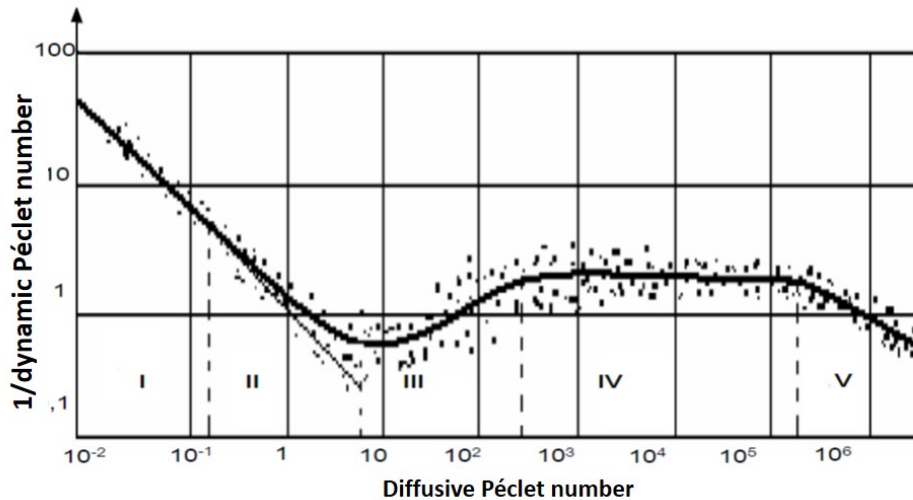


Figure 1.8 Schematic showing the different regimes of a miscible displacement flow (Adapted by Pfannkuch, 1963)

Mathematical models

The analysis of suspended particle transport through a porous medium can be represented macroscopically as a problem of solute transport through a homogeneous medium. The governing equation of this classic problem is given by the convection-dispersion equation:

$$\frac{\partial \phi C}{\partial t} = -\nabla \cdot (UC) + \nabla(\phi \mathbf{D} \cdot \nabla C) \quad (1.17)$$

where C [M/L³] is the mass concentration of suspended particles in the pore water, t [T] is time, ϕ [L³/L³] is initial porosity, D [L²/T] is the hydrodynamic dispersion coefficient, U [M/T] is the Darcy velocity.

When mass transfer occurs between the medium and the solute, a rate term can be added to the equation:

$$\frac{\partial \phi C}{\partial t} + \rho_b \frac{\partial S}{\partial t} = -\nabla \cdot (UC) + \nabla(\phi \mathbf{D} \cdot \nabla C) \quad (1.18)$$

where S [M/M] is the mass fraction of deposited particles to porous medium, ρ_b [M/L³] is the particle bulk density.

1.5 Filtration in porous media

1.5.1 Different types of filtration

A filter composed of a granular porous medium is employed to remove the particles in the fluid. The efficiency of the filter process depends on several parameters: filter (porosity, pore diameter, grain size and shape), particles in the suspension (concentration, size, shape, density and physical and chemical nature), solute characteristics (viscosity, density, pH and salinity) and flow characteristics (velocity and hydraulic pressure). There are four different filtration processes generally considered (Fig. 1.9).

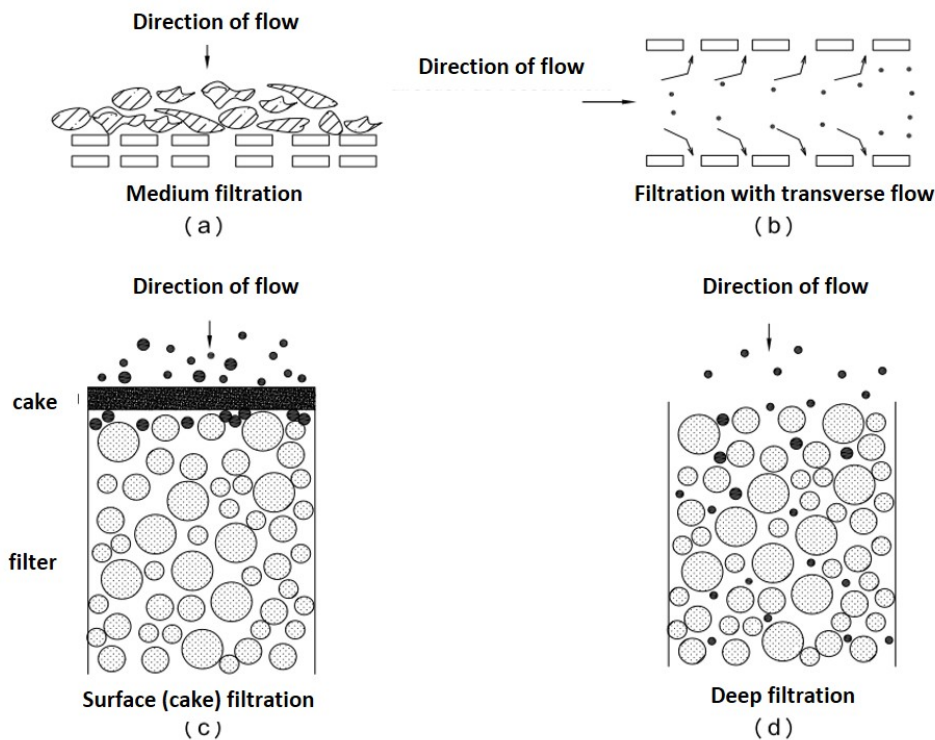


Figure 1.9 *Diagram of different filtration types*

Medium filtration

In this process, pore size is smaller than that of the particles in the suspension to be filtered. For particles larger than $50 \mu\text{m}$, the filter is used as a sieve. For small particles, membranes whose pore size is well-defined are most often used. This filtering method leads to a very rapid shut-off of the filter, which needs regular suspension of the filtration process in order to clean the filter.

Transverse filtration

In this process, a direction of the flow of the suspension parallel to the surface of the filter medium is chosen. This is ensured by a shearing rate to avoid the deposition of particles in the pores. This choice preserves the continuity of the filtration process by avoiding the clogging of the porous medium.

Cake filtration

For particles comparable in size to or larger than the porous media grain size, penetration into the media will not occur, but rather a filter cake or surface mat will form above the media. As a result, substantial particle accumulation can occur, leading to a decrease in permeability.

Deep filtration

This filtration process has been used for water clarification. In this case, the filtration is applied for particle suspension with concentration than 0.5 g/l (Tien and Payatakes, 1979) and particles should be smaller than 30 μm . The suspended particles smaller than the pore size penetrate the porous medium and circulate along the flow lines. Some of the particles exerted multiple forces are deposited at different depths of the filter medium, hence the filtration process is called deep filtration. Developed by Herzig et al. (1970), the theory is based on the study of concentration and retention profiles within porous beds.

1.5.2 Particle retention sites

The particle retention sites in porous media have been distinguished by Delanchambre (1966). It describes four main types (Figure 1.10), depending on the blockage of the particle at the middle entrance or at depth in the middle layers which are:

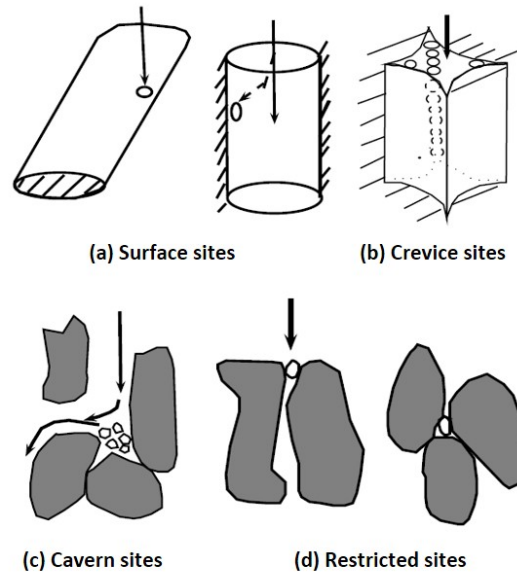


Figure 1.10 *Diagram of different types of retention sites*

- Surface sites (a): grains in a filter supply large surface, and particles in suspension can be removed by physical-chemical interactions between particle and grain surface.

- Crevice sites (b): the suspended particle is in the vicinity of the line of contact between two convex surfaces. The particle can be retained by mechanical wedging in the crevice.

- Cavern sites (c): the sites have concave shapes and are generally found in the elbows of the pores, so that the fluid therein is immobile and does not participate in the flow.

- Restricted sites (d): Particle is too large to pass the pore throat, and this mechanism is also called straining.

1.5.3 Particle – collector interaction model

Mean-field DLVO interaction forces

The mechanistic models that are utilized to predict the particle deposition depend on DLVO interactions. Classic DLVO theory (Derjaguin and Landau, 1941; Verwey and Overbeek, 1948) attempts to describe the particle-collector interactions in terms of adhesive and repulsive forces, which are the Van der

Waals interaction energies and the electrical double-layer interaction ones, respectively. The van der Waals force is a general term used to define the attraction of intermolecular forces between molecules. There are three kinds of van der Waals forces: force between permanent dipoles; force between a permanent dipole and a corresponding induced dipole; force between instantaneously induced dipoles. Electrical double-layer forces occur between charged objects across the liquid. The interaction energy between two surfaces can be expressed as: $\phi_{tot} = \phi_{dl} + \phi_{vdW}$, where, ϕ_{tot} , ϕ_{dl} and ϕ_{vdW} are the total, the double-layer and the Van de Waals interaction energies respectively.

The expression of double-layer energy can be written as (Hogg et al., 1966):

$$\phi_{dl} = \pi \varepsilon_p \varepsilon_0 r_p [2 \xi_p \xi_g \ln \left(\frac{1 + \exp(-k_D \delta)}{1 - \exp(-k_D \delta)} \right) + (\xi_p^2 + \xi_g^2) \ln (1 - \exp(-2k_D \delta))] \quad (1.19)$$

ε_p is the electric permittivity of the matrix, ε_0 is the electric permittivity of the vide, ξ_p and ξ_g are the zeta potential of particle and collector respectively, k_D is the reciprocal of the Debye length and δ is the separation distance between the particle and collector surface.

The van der Waals interaction energies can be expressed as (Bhattacharjee and Elimelech, 1997):

$$\phi_{vdW} = -\frac{H}{6} \left[\frac{r_p}{\delta} + \frac{r_p}{\delta + 2r_p} + \ln \left(\frac{\delta}{\delta + 2r_p} \right) \right] \quad (1.20)$$

r_p is the particle radius, H is the Hamaker constant.

Extended DLVO theory

Attraction forces tends to be infinite, and the separation distance can tend to be infinitesimal. However, it is impossible. As the particle approaches the plate very close, the electron clouds of the molecules on the interaction surfaces (particle and plate) would overlap, then creating large repulsion forces. This phenomenon is called steric effects arise and the repulsion is called Born repulsion. Born repulsion increases drastically with the decreasing

separation distance, of which the increase rate is far greater than that of van der Waals attraction force, therefore inhibiting the particle from approaching the plate further. Due to steric effects, the attraction force in the primary minimum well cannot be infinite, so it is possible that particles can get rid of primary minimum energy well and exit the SWI back to the bulk fluid. Between a particle and a plate, Born repulsion energy can be expressed as (Ruckenstein and Prieve, 1976):

$$\phi_{Born} = \frac{H\sigma_c^2}{7560} \left[\frac{8r_p + \delta}{(2r_p + \delta)^7} + \frac{6r_p - \delta}{\delta^7} \right] \quad (1.21)$$

Therefore, the total interaction energy can be expressed as:

$$\phi_{tot} = \phi_{dl} + \phi_{vdw} + \phi_{Born} \quad (1.22)$$

According to the equations, the total interaction energy is a function of separation distance between the particle and collector surface. In general, if the particle population and the collector surface have the unlike charges in mean-field, then existing no repulsion between particles and surface, we call it favorable deposition conditions. Otherwise, it is unfavorable conditions. Figure 1.11 presents classic DLVO interaction energy profiles for favorable and unfavorable interaction conditions. Several typical features are exhibited, such as primary energy minimum, secondary energy minimum and energy barriers. Under unfavorable conditions, a repulsive barrier limits not only physical contact between particle and collector but also the particle escaping from the primary minimum.

Outside this repulsive barrier exists a small region of attraction where particles may accumulate in a secondary minimum. In situations where particles either possesses enough energy to overcome the barrier or where no barrier exists (favorable conditions), they can enter the primary minimum (Figure 1.11) and physically attach to the surface.

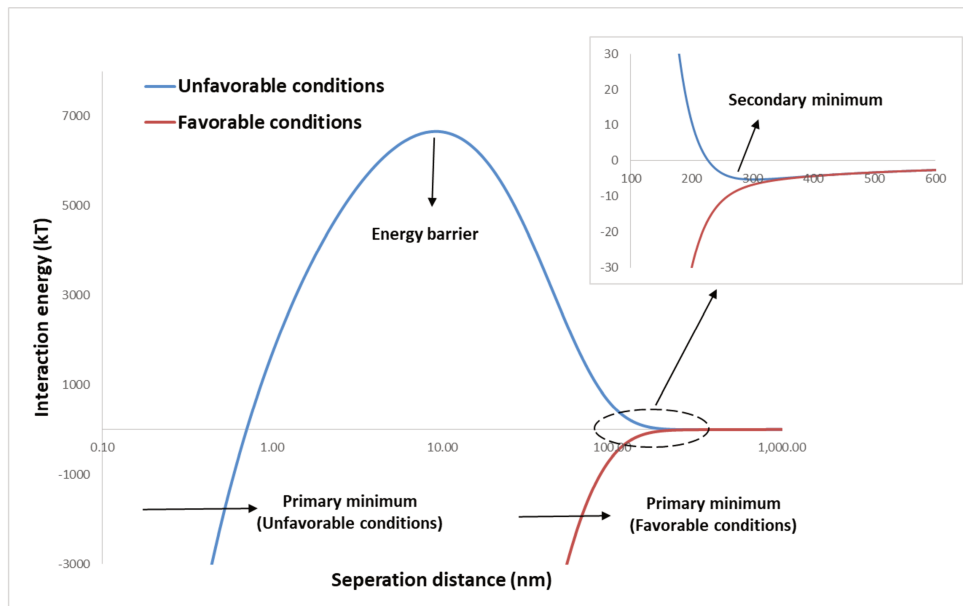


Figure 1.11 Interaction energy profiles of the function of separation distance between particle and collector surface.

1.5.4 Collision mechanisms and single collector model

The collision of particles on a surface of the medium, called "collector", can lead to the capture of the particle in a site on effects of different mechanisms. This collision is a function of several physical parameters, such as flow velocity, pore diameters, density and size of the particle, as well as some chemical ones, such as the surface charges, the pH and the ionic strength of the solute. Yao et al. (1971) proposed a single collector model, which considers interception, sedimentation and diffusion. This model has been regarded as the foundation of the colloid filtration theory (CFT) and the introduction of CFT sparked recent four decades of research from pore to field scale on particle transport and retention. Figure 1.12 presents the dominant capture mechanisms of a particle to a collector by sedimentation, direct interception and Brownian motion.

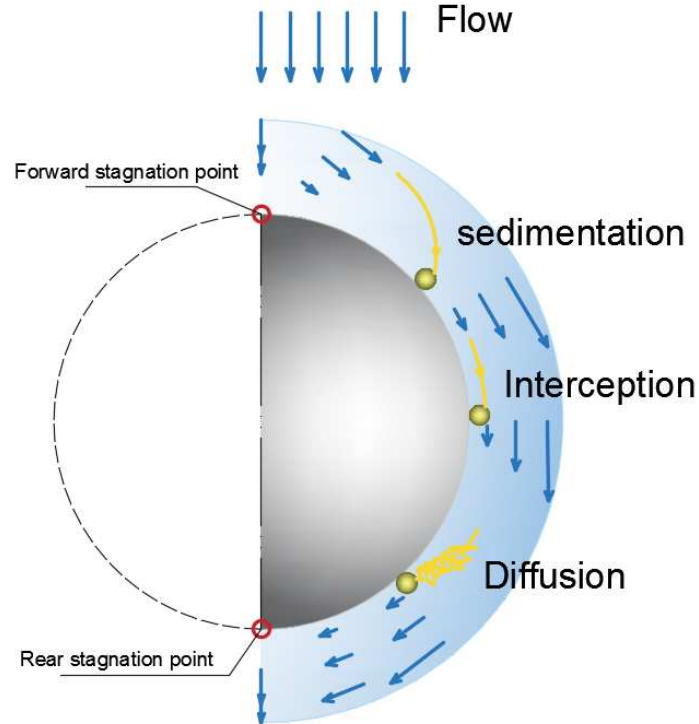


Figure 1.12 Dominant transport mechanisms of particles to the collector surface

- Sedimentation: The path of the particle is influenced by the combined effects of the buoyant weight of the particle and the hydrodynamic forces on the particle, leading a collision between the particle and the collector. The particles will be removed from the current lines in the direction of the gravitational force. The parameter which controls the gravitational sedimentation for a spherical particle with diameter d_p is the Stokes settling velocity,

$$v_s = \frac{g}{18\mu}(\rho_p - \rho_f)d_p^2 \quad (1.23)$$

where μ is the dynamic viscosity of the fluid, g is the gravitational acceleration, ρ_p and ρ_f are the particle and fluid densities, respectively. When the particle density is equal to the fluid density, the Stokes settling velocity is equal to zero and the effects of gravity can be neglected.

- Interception: a suspended particle following a streamline of the flow may come in contact with the collector due to its own size, characterized by a function of an interception parameter $(d_p/d_c)^2$, d_c is the collector diameter.

- Diffusion: For small particles, less than a few micrometers, the dominant transport to the collector surface is via Brownian motion of particles. This motion is characterized by a particle diffusivity D_p , the mathematical expression is derived by Einstein,

$$D_p = kT/3\pi\mu d_p \quad (1.24)$$

where k is the Boltzmann constant, T absolute temperature.

Correlation Equations of single-collector contact efficiency

CFT approaches based on the single collector model have two major components: i) a mechanistic force and torque model describing particle trajectory and deposition; ii) correlation equations that approximate the results of the mechanistic models. Both mechanistic models and correlations equations are broadly successful in predictions of the single-collector contact efficiency (η) under favorable conditions [Rajagopalan and Tien, 1976; Tufenkji and Elimelech, 2004]. The correlation equations divide particle transport to the collector surface into three dimensionless numbers representing interrelated mechanisms: interception, diffusion and sedimentation. The total efficiency can be expressed as the sum of the diffusion, the interception, and the gravity contributions to particle transport toward the collector:

$$\eta_0 = \eta_D + \eta_I + \eta_G \quad (1.25)$$

where η_D is the contribution from diffusion, η_I is the contribution from interception, and η_G is the contribution from gravity.

Different correlation equations of the deposition efficiency have been developed in the literature to approach the deposition dynamics. TE model is often used in efficiency approaches, the efficiencies can be expressed (Tufenkji and Elimelech, 2004):

$$\eta_D = 2.4A_s^{1/3}N_R^{-0.081}N_{Pe}^{-0.715}N_{vdW}^{0.052} \quad (1.26a)$$

$$\eta_I = 0.55A_sN_R^{1.55}N_{Pe}^{-0.125} \quad (1.26b)$$

$$\eta_G = 0.22N_R^{-0.24}N_G^{1.11}N_{vdW}^{0.053} \quad (1.26c)$$

Where A_s is a porosity-dependent parameter, N_R is the interception number, N_{Pe} is the Peclet number, N_{vdW} is London-van der Waals attractive forces number, and N_G is the gravitational number.

As mentioned previously, particle transport with mass transfer between the solid matrix and suspension at continuum scale can be expressed as:

$$\frac{\partial \phi C}{\partial t} + \rho_b \frac{\partial S}{\partial t} = -\nabla \cdot (UC) + \nabla(\phi D \cdot \nabla C) \quad (1.27)$$

The retained particle concentration (S) is written as: $S = k_d \phi C$, where k_d is deposition rate coefficient. According to the classical particle filtration theory, k_d keeps constant during particle transport and is a function of η_0 , expressed as:

$$k_d = \frac{3(1-\phi)}{2} \frac{1}{d_g} \alpha \eta_0 u \quad (1.28)$$

In Eq.1.28, $\frac{3(1-\phi)}{2} \frac{1}{d_g}$ represents the specific grain surface per unit volume or mass of porous media. Therefore, Eq. 1.28 realize the upscale of particle deposition dynamic from pore to assemblage scale, to an extent.

1.5.5 Experiments under favorable and unfavorable deposition conditions

As we introduce the particle-collector interaction model in the previous section, favorable and unfavorable deposition conditions are mentioned. Under favorable conditions, without the obstruction of energy barriers, the particle can physically contact the collector surface. Such deposition with physical contact, is referred to as attachment. Under unfavorable conditions, theoretically, only if the particle overcomes the energy barrier with great hydrodynamic forces, the particle cannot have physical contact with collector surface. Therefore, particle deposition efficiency under favorable conditions is generally much higher than that under unfavorable conditions. The height of energy barriers is influenced by several physical and chemical factors, e.g., the zeta potentials of particle and collector surface, solution pH and ionic strength, collector surface roughness and so on.

Laboratory column experiments are indirect observation methods widely used to study the particle behavior in porous media. A particle suspension is

injected into the column packed with porous media by a peristaltic or syringe pump. Effluent particle concentration at outlet is measured with a spectrophotometer or turbidimeter to produce breakthrough curves, usually abbreviated to BTCs (Fig. 1.13a,b). BTCs provide useful information to characterize the transport of particles in the porous media. Following the suspension injection, the column is disassembled and the porous medium is excavated into several sections to measure the retained mass at different positions. Spatial distributions of retention injection provide information regarding to particle retention profiles (Fig. 1.13c,d). By fitting the BTCs and retention profiles with transport and deposition mathematical model, we can get important hydrodynamic parameters, like average pore velocity and dispersion coefficient, as well as deposition kinetic parameters, such as deposition and/or re-entrainment rates, maximum deposition concentration and so on.

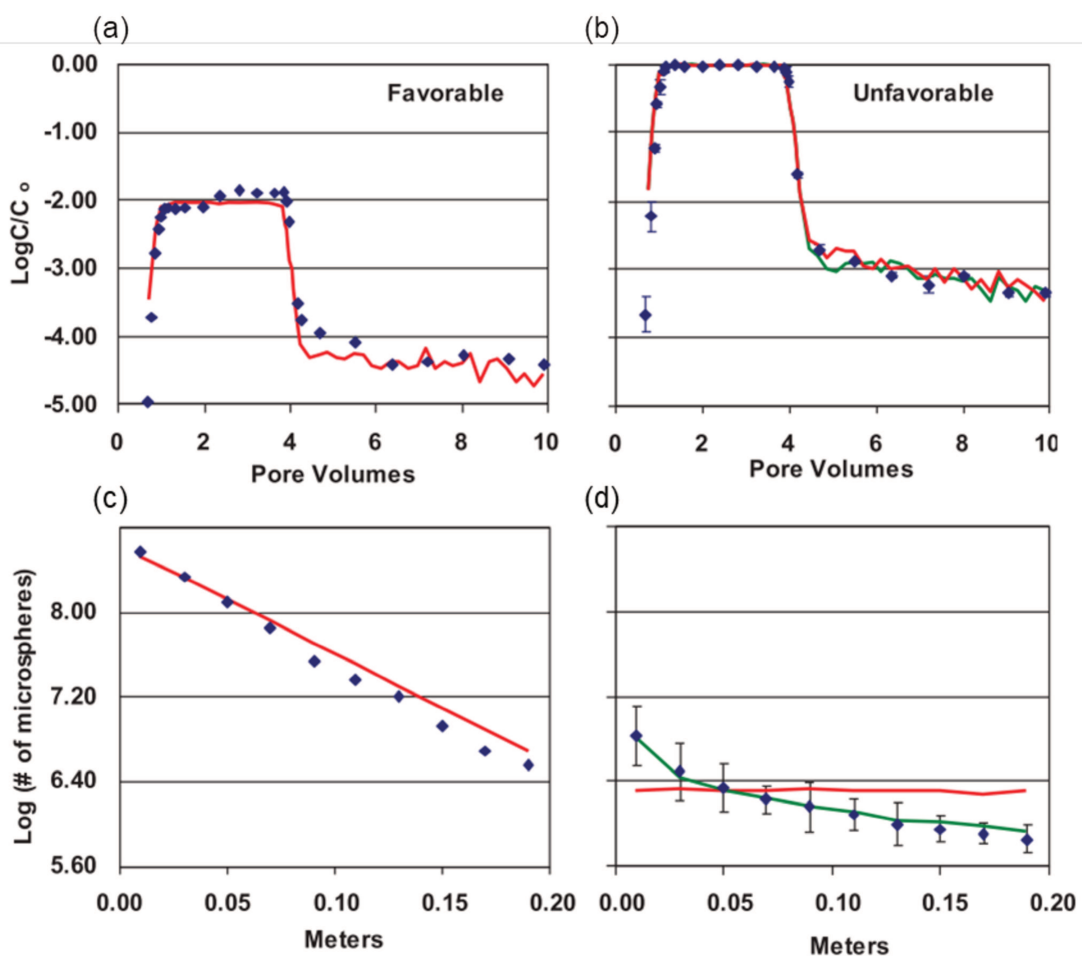


Figure 1.13 *Experimental data (symbols) for the BTCs (a,b) and retention profiles (c,d) of polystyrene latex microspheres in quartz sand in unfavorable and favorable conditions described in Li and Johnson [2005]. Lines are continuum model descriptions with a single deposition rate coefficient. The single deposition rate coefficient was used to generate a probabilistic deposition distribution. Adapted from Li and Johnson [2005]. [Molnar et al., 2015]*

Due to great differences in particle-collector interaction energies between “favorable” and “unfavorable” conditions, very different particle transport and deposition behaviors are observed in column experiments under favorable and unfavorable conditions. Column experiments conducted under favorable conditions typically exhibit relatively simple particle transport behavior: as seen in Figure 1.13a, particle breakthrough during injection reaches a steady state plateau in short-term [Elimelech et al., 2000; Li et al., 2005; Tufenkji and Elimelech, 2005]. Transport and deposition model with constant k_{dep} is capable of well fitting both BTCs and retention profiles (e.g. Fig. 1.13a,b). This indicates that deposition rate keeps approximate constant under favorable conditions, which conform to colloid filtration theory.

Very different transport and deposition behavior from those conducted under favorable conditions can be observed in those conducted under unfavorable conditions (e.g. Figure 1.13c,d). Under certain experimental conditions, the BTCs under unfavorable conditions may also reach a steady state plateau sometimes [Elimelech et al., 2000; Li et al., 2005; Jiang et al., 2012]. By contrast, nonsteady state behavior occurs more often. The effluent concentration may gradually increase over time, since mean-field repulsive interactions between particle and collector result in limited number of deposition sites, which are progressively filled (blocking) with more and more retained particles [Liu et al., 2009; Lin et al., 2011; Mattison et al., 2011; C. Wang et al., 2012; Liang et al., 2013]. Decreasing concentration during breakthrough (ripening) suggests that favorable particle-particle interactions allow already retained particles to supply additional sites for further particle retention [Tong et al., 2008; Jiang et al., 2012]. These processes can also cause the variation of filtration capacity of the porous medium with time and space. Therefore, the prediction of CFT with constant k_d has evident deviations of retained profiles with experiment or field results.

Extended tailing may be observed in the BTC during the elution phase of column experiments in the presence of energy barriers (Fig. 1.13e). Tailing results from the slow release of particles from the column outlet and is the macroscopic performance of dramatic particle re-entrainment from the collector surfaces and contacts. Tailing is often observed for microbes in the laboratory [Harter et al., 2000; Li and Johnson, 2005; Li et al., 2005], field [DeBorde et al., 1999; Ryan et al., 1999], and nonbiological particles [Li et al., 2004; Tufenkji et al., 2004; Li et al., 2005; Tong et al., 2005; Johnson et al., 2007]. In the presence of energy barriers, the reentrainment dynamics are very sensitive to hydrodynamic and chemical perturbations, including variation in ionic strength [Ryan et al., 1999; Tufenkji and Elimelech, 2004, 2005; Shen et al., 2007; Mattison et al., 2011; Jiang et al., 2012; Shen et al., 2012], variation in pH [Ryan et al., 1999; Tufenkji and Elimelech, 2004, 2005], and variation in fluid velocity [Shang et al., 2008; Pazmino et al., 2014]. Such reentrained particle population is considered to be particles retained within secondary energy minimum. The particle retained within shallow primary minima with low energy barriers, i.e. on the peak of roughness, may also contribute to the reentrainment. (Shen et al., 2012; Jin et al., 2016)

1.5.6 Deposition and re-entrainment dynamics under unfavorable deposition conditions

For more than recent four decades, the colloid filtration theory (CFT) stemming from Yao et al. (1971) has been supplying the basis for a functioning theory to predict particle transport and removal in homogeneous porous media without particle-grain repulsion. However, in aquifers, both particles and porous medium grain typically are found to be negatively charged and the subsurface water generally has a low ionic strength and neutral pH (Bradford et al, 2006). Under these conditions, the electrical double layer interaction is repulsive, yielding an energy barrier for attachment (so-called unfavorable conditions). Nearly no particle deposition is predicted by existing models derived from CFT in the presence of energy barriers because these models are constructed based on the hypothesis of totally equivalent surface characteristics (e.g. zeta potentials and surface topography) across

the whole surfaces. However significant deviations were often found between the predictions with mean-field approaches and experimental results under unfavorable conditions for both biological and nonbiological particles. (Bradford et al., 2002; Li et al., 2004; Redman et al., 2001; Tufenkji, 2007; Yang et al., 2015). Deposition mechanisms in the presence of strong energy barriers (Fig. 1.14) have been widely investigated in the literature over the last decade.

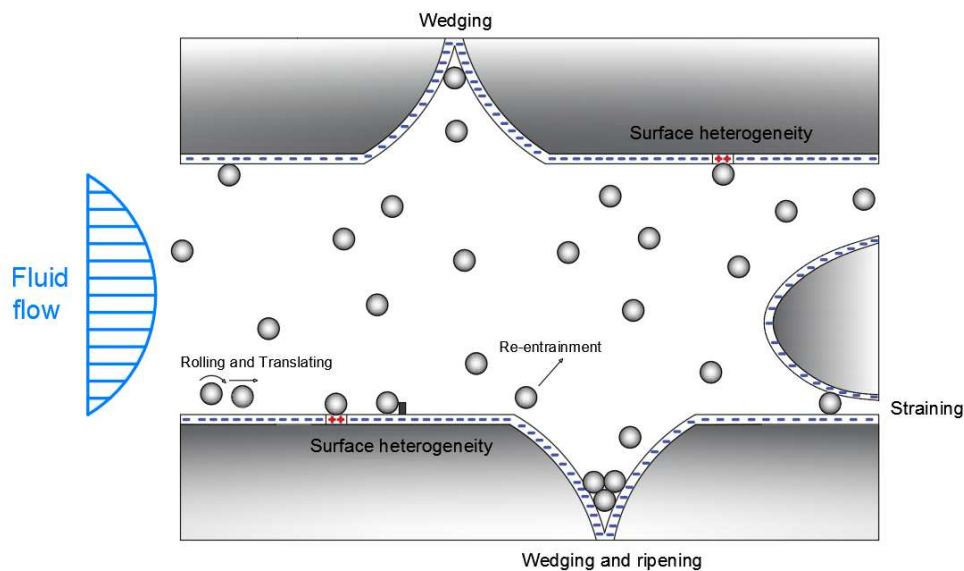


Figure 1.14. Schematic illustration of different deposition mechanisms under unfavorable deposition conditions.

Straining and wedging

In the last two decades, straining and wedging in porous media has been increasingly found to not only dominate deposition dynamics for the great size ratio of particle:collector (over 0.05 proposed by Herzig et al., 1970), but also have strong influence on particle transport in deep filtration. Straining indicates particle entrapment in pore throats too small to pass. Wedging indicates particles removed by grain-grain contacts. Straining and wedging have similar mechanisms, referring to particles entrapped by several adjacent grain surfaces. Therefore, the two mechanisms are sometimes regarded as one mechanisms and called straining. In general, straining happens when the size ratio of the particle to collector (dp/dc) is above a critical value (Knappett et al., 2008; Pelley and Tufenkji, 2008), and particle straining rates increase with larger dp/dc (Xu et al., 2008). Several critical dp/dc values are reported, e.g., 0.005 (Johnson et al., 2007a; Ma et al. 2009), 0.003 (Bradford et al., 2007), 0.008 (Xu et al., 2006) and 0.0017 (Bradford et al., 2002).

However, Johnson et al. (2007b, 2010, 2013) argued that the so-called straining with such a small particle:collector ratio might just be the removal of particles at grain-to-grain contacts, or wedging.

The occurrence of straining has many implications for particle transport in porous media. Generally, the deviation in the deposition profile from CFT induced by straining tends to increase with increasing particle size or decreasing grain media size (Bradford et al., 2006). Straining is depth-dependent and it is mainly observed at column inlets (Gargiulo et al., 2007; Johnson et al., 2007b; Bradford et al., 2006). Straining is also dependent on the concentration of strained particles, with Xu et al. (2006) observing that straining rate coefficients exponentially decrease with increasing concentration of strained particles.

Numbers of chemical, physical and hydrodynamic factors can affect and determine the occurrence of straining. Shen et al. (2008) and Mesticou et al. (2016) evaluated the role of solution ionic strength on particle straining, and confirmed that the critical dp/dc is significantly reduced at higher ionic strength due to additional straining induced by particle retention, predominantly in the grain-grain contacts.

Size exclusion

The importance of size exclusion was elucidated in considering the reasons for unexpected large migration distances of solute contaminants, such as radionuclides, in the subsurface because of their cotransport with groundwater particles. Size exclusion, also known in a more general concept as hydrodynamic chromatography, has been recognized as an underlying phenomenon for faster migration of particles compared to non-reactive solute in porous or fractured media [Xie et al., 2014; Albarran et al., 2013]. Due to this mechanism, up to 4 - 5.5 times enhancement in particle velocity compared to mean pore water velocity has been observed in micro-models [Keller and Auset, 2007, Sirivithayapakorn and Keller, 2003].

Size exclusion has occurred generally in the context of particle transport on two different scales. At pore network scale, the size exclusion concept has been referred to as the exclusion of particles larger than a portion of the pores that can be passed through by solute but not by the particles [Bradford et al.,

2006; Chrysikopoulos and Katzourakis, 2015]. At pore scale, size exclusion has been attributed to migration of particles on flow paths which are close to the center of the pore channels. Particle velocity is theoretically 1.5 times larger than the mean pore water velocity on the effects of Taylor dispersion [Grolimund et al., 1998; Keller et al., 2004].

Blocking and Ripening

The surface of porous materials may have a limited capacity for the deposition of particles and once this capacity is filled, the deposition of further particles is hindered by the presence of previously retained materials. The most well-known approach for modeling this process, which is called site-blocking effect, is to use the Langmuir approach for particle adsorption onto solid surfaces [Adamczyk et al., 1994]. This is used to model the site-blocking effect of suspended particle attachment during transport in porous media via the following relationship [Saiers et al., 1994]:

$$k_d = k_0 \left(1 - \frac{S}{S_{max}}\right) \quad (1.29)$$

where k_0 [1/T] is the initial coefficient of deposition rate; S [M/M] is the retained particles concentration, or retention; S_{max} [M/M] is the maximum concentration of retained particles.

Ripening is the opposite of the blocking phenomenon, particles deposit at additional retention sites supplied by previously retained particles with adjacent particles or grain surface. Also, in contrast to the blocking mechanism, in which the deposition rate decreases with time, ripening causes an increase in the deposition rate with time. This leads to a dropping plateau of the BTC in the case of ripening [Tong et al., 2008; Jiang et al., 2012]. Ripening has been observed from nano to micro particles.

Retention within the secondary energy minimum

Weakly adhesive interactions happen at zones where the fluid drag is low and overcome by secondary energy minimum interaction (Liu Y. et al., 2009; Li et al., 2010; Johnson and Tong, 2006). As the ionic strength increases, the magnitude of the secondary minimum is also enhanced and may be sufficient

to not only overwhelm hydrodynamic drag forces but also exceed colloidal Brownian diffusion forces (Torkzaban et al., 2007). The secondary minimum is also enhanced at pH values close to pHPZC (either particle or grain media), as the surface potential as well as EDL interaction is very small at such condition. Under these conditions, the attractive vdW interactions dominate and the secondary energy minimum depth is increased (Ryan et al., 1999; Elimelech et al., 2000; Quevedo and Tufenkji, 2009). Particles that associate with the secondary energy minimum are considered reversibly attached. Evidence in support of reversible attachment in the secondary minimum are found in studies that intentionally evaluate particle release by perturbing system conditions, e.g., eluting column with low ionic strength solution after deposition (Bradford et al., 2007; Canseco et al., 2009).

Heterogeneity

In the natural and industrial processes, particles and grains are created or produced with different form factors. These particles and grains have (depending on their chemical composition) electrical charge heterogeneities and/or topographic heterogeneities. Indeed, electrostatic "patches" due to the presence of aggregates or organic matter adsorbed on the surface can be formed, and the surface topography is not smooth, involving asperities. These heterogeneities result in changes in the shape and intensity of surface interactions (Ducker et al., 1991) and consequently have an influence on the adsorption and desorption phenomena (Elimelech And O'Melia, 1990).

Heterogeneities are confirmed to be one of dominant deposition mechanisms under unfavorable conditions, in the presence of interaction energy barriers (Φ_{max}) of several to hundreds of $k_B T$ between particles and collector surface. The effects of heterogeneities have been widely studied qualitatively and quantitatively by experiments and numerical simulations in the literature. The attachment is due to the local presence of nano to micro scale favorable sites, in spite of unfavorable deposition surface characteristics in the mean-field. Suresh and Walz (1996) have shown in their work that the average interaction repulsion has been reduced in the presence of roughness, thus promoting deposition of the particles. This reduction is related to the size

of the particles and the asperities as well as the density of the latter. The repulsion of the double layer has been found to be much reduced in the peaks of rough surfaces [Bowen et al., 2002; Bradford et al., 2013; Shen et al., 2012]. In this sense, the inter-particle interaction is not determined by the radius of curvature of the particles but by that of the surface asperities. Greater retention of latex microspheres was observed on rough glass beads, of which the collision efficiency is 30 – 50% higher than those observed in the presence of smooth beads [Shellenberger and Logan, 2002; Yoon et al., 2006].

Collector surface heterogeneity

Widespread retained particles over a large size range from 0.25 to 9 μm have been directly observed on the bulk surfaces of glass beads by Johnson et al. (2010). Negligible reentrainment has been observed for all size particles even at five times higher flow velocity. This indicates that most particles retained within the primary energy minimum with physical bonds to collector surface. However, the classical models with mean-field particle-collector interactions cannot achieve physical contact between the particle and the collector surface in the presence of significant repulsion between the bulk surfaces. The models with discrete nanoscale to microscale physical and chemical heterogeneity on the collector surface (referred as to heterodomains) have been proposed. Around the discrete heterogeneity particle-collector repulsion is locally reduced or eliminated [Duffadar and Davis, 2008; Bendersky and Davis, 2011]. Heterodomains differ from the macroscopic surface heterogeneities, they are widely distributed on grain surfaces. These heterodomains can bring particles into physical contact with the surface, then generating surface friction against the tangential hydrodynamic drag. For the particles retained within the secondary minimum, friction is considered to not exist due to no physical contact with collector surface.

Attractive or repulsive net interaction is produced with collector surface heterogeneity between different sized particles and collector surface [Pazmino et al., 2014]. Since particle-collector interactions decay rapidly with increasing separation distance, the influence of curvature of the particle surface cannot

be neglected. The zone of significant particle-collector interaction (ZOI) is a fraction of the projected area of the particle. Under unfavorable conditions, particle-collector interactions are repulsive on mean-field except for the heterodomains. The fraction of heterodomain in ZOI determines the net particle-collector interaction with the summation of attractive and repulsive interactions. Hence, the net particle-collector interaction (attractive versus repulsive) depends on the interplay of particle size, heterodomain size, and ionic strength [Pazmino et al., 2014]. With increase of particle size, the fractional coverage of ZOI in a given sized heterodomain decreases, maybe leading to net attractive interaction for the small particle, and net strong repulsion for the large particle.

Particle population heterogeneity

The heterogeneity of the particle population encompasses the physical heterogeneity (size and shape) and the physiochemical heterogeneity (surface charge and multiple energy minima). In a deep bed filtration system, where straining and size exclusion mechanism dominates deposition kinetics, the larger particles in the particle population deposits faster and correspond to greater deposition rates and retention. Since straining and size exclusion almost only depend on the size ratio of particle:collector, the particle size distribution most probably results in the distribution of the deposition rate (Shapiro and Bedrikovetsky, 2013). Due to the particle surface heterogeneity and second energy minimum, a suspension of monodisperse latex colloids injected in a homogeneous porous medium sometimes can yield a hyperexponential deposition profile in the presence of strong energy barriers [Li et al., 2004; Tong et al., 2006; Tufenkji and Elimelech, 2005]. Mathematically, the distributed deposition rate is employed to describe the effects of the heterogeneity of the particle population. The approaches with various distribution types of the deposition rate, i.e. the log-normal distribution, the power law distribution, the bimodal distribution, have been attempted to simulate the effects.

Irreversible and reversible deposition

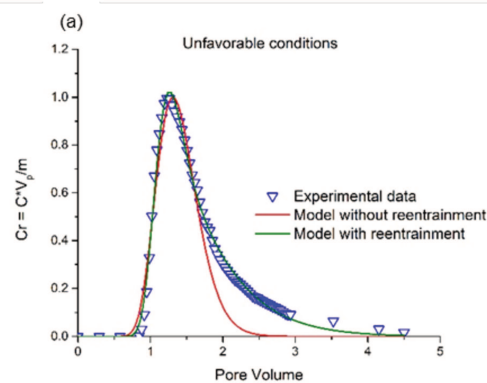
“Irreversible/reversible” is used to describe the state of deposited particles. Under favorable conditions, most of retained particles are fixed within deep primary energy minima in the absence of energy barriers. The particles have physical contacts with collector or grain surface, thus considered “reversible”. However, under unfavorable conditions, most particles, which enter in the near-surface domain, are associated with the collector surface via secondary energy minima or shallow primary minima. Many particles are not retained even temporally on the surfaces, they advance slowly with the flow by rolling and/or translation at very low velocities due to the collector surface attraction. Some particles are really fixed unstably with the weak attraction for a given condition. However, with hydrodynamic or chemical perturbations, the mechanical equilibrium is broken, and the particles escape from the near-surface domain back to the bulk fluid. For both two situations, the residence times of particles fairly increase, thus the particles are called “reversible” deposited particles. The behavior that the particles struggle to advance with the flow against the surface attraction is called “re-entrainment”.

1.6 Conclusions and research objectives

Our research group (LOMC Le Havre) has focused on the particle transport study in porous media for more than ten years. Large numbers of laboratory column experiments have been realized to study the effects of kinds of factors, such as flow rate, pH, concentration, particle size distribution, grain size distribution. In most of these experiments, natural silica particles (e.g., kaolinite particle) were used to prepare injected suspensions, and the column was packed with quartz sands as studied porous media (e.g., Seine river sand). Both silica particle and quartz sand, mainly composed by silicon dioxide, have negative surface charges. Therefore, these experiments were conducted under unfavorable conditions. To study the deposition mechanisms under unfavorable conditions by numerical methods, the experiments in the Hammadi’s doctoral research [Ahfir et al., 2016; Hammadi et al., 2017] were chosen for our modelling study. Hammadi conducted two series of laboratory

column experiments, pulse-input and step-input injections. Relative to the previous experiments, Hammadi's study has distinct improvements. Pure water was used for preparing particle suspension with extremely low pH, then eliminating the pH effects for all experiments. For pulse-input injection, polystyrene latex microspheres were used as suspended particles. In contrast to natural particles, on one hand, latex particle has similar density to low, avoiding the gravity effects; on the other hand, latex particle has a very narrow size distribution, regarded as single-sized particle, therefore the effects of particle size can be studied precisely. For step-input injection, kaolinite particles were used and particle sizes were selected between 2 to 30 μm . On one hand, particle selection eliminated clay particles ($< 2 \mu\text{m}$) and ensured studied particles within the size range of silt; on the other hand, it increased the measurement's precision of the turbidimeter at effluent.

In Hammadi's work, he tried to fit the measurements (BTCs and retention profiles) with CFT deposition model with constant k_d and obtain transport and deposition parameters. However, distinct deviations for both pulse- (Fig. 1.15a) and step-input (Fig. 1.15b,c) injection experiments were observed as the previous literature. In the pulse-input injection, CFT failed to reproduce an extended tailing of BTC. For the step-input, CFT was able to simulate the effluent concentration, however, cannot fit the retention profile, especially near the column inlet. Therefore, the specific deposition models need to be developed to simulate the experiments for better understanding of the particle behavior under unfavorable conditions.



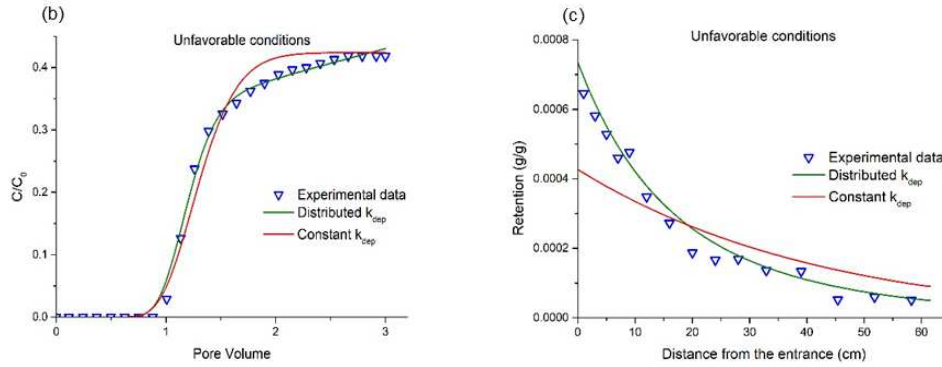


Figure. 1.15 BTCs and retention profiles under unfavorable conditions.

The overall objective of this study is aimed at have insights into the mechanisms that control particle transport and deposition under unfavorable conditions in saturated porous media by performing numerical simulations of laboratory column experiments. The specific objectives are to:

1. Develop the specific transport and deposition models under unfavorable conditions.
2. Develop the numerical models to simulate the experiments and obtain the transport and deposition parameters by inverse methods.
3. Based on the experimental and numerical results as well as evolutions of parameters' values, analyze the roles of the deposition mechanisms and effects of different physical factors on particle transport behavior.

In this chapter we present a literature review of particle transport in porous media. The definitions of different geological formations of subsurface groundwater, porous medium properties and Darcy's law to characterize the flow were introduced. Then convection dispersion equation was applied to particle suspension transport. In the last section of this chapter, we present the filtration theory, and focus on the deposition mechanisms under unfavorable conditions.

In chapter 2, based on the classic colloid filtration theory and recent study results on particle deposition in the presence of energy barriers, we will propose mathematic model to describe suspended particle behavior in saturated porous media. Then a numerical model will be developed to simulate the column experiments. The particle transport program is composed of transport and optimization modules to fit experimental measurements and

obtain best-fitted values of transport and deposition parameters in the model. In chapter 3, the developed numerical model will be applied to modelling the column experiments of Hammadi's work [Hammadi's, 2017]. With experimental and numerical results, the deposition mechanisms under unfavorable conditions will be elucidated as well as effects of different physical factors, like flow rate, particle size, etc.

Chapter 2 Transport deposition reentrainment model and numerical simulation

Depending on the descriptive scale of particle transport behavior and the precision of outcome results, modeling tools used to describing or predicting particle behavior in porous medium for laboratory experiments can be categorized in two groups, mechanistic models and continuum-scale models. Mechanistic models focus on a small number of individual particles at pore or grain scale. They consider the forces, torques, microfluid and energy of particle and contacting media. Mechanistic models supply a direct simulation to understand the effects of different factors such as collector surface physical and chemical heterogeneity at local scale. Continuum-scale models are defined as partial different equations based on the continuity principle over the bulk spatial and temporal domains of the studied system. In contrast to mechanistic approaches which deal with forces or energy, continuum models deal with rates, like initial deposition rate. In this study, we used continuum models to realize modeling of particle transport.

2.1 Transport, deposition and re-entrainment model

The particle transport through homogeneous porous media is assumed to be mainly affected by three physical processes, namely advection, hydrodynamic dispersion and deposition. For the experiments studied in the present paper, both particles and porous media grains being negatively charged, straining and wedging should be considered as the dominant mechanism in the particle deposition process in the presence of an energy barrier. As the volume of injected suspension is not considerable, the modifications of pore-network structure are slight. The parameters of porous media, such as porosity and dispersion coefficient, can be considered constant then can be put out of the derivative operation in Eq. 1.27. In this work, we will realize modelling of laboratory column experiments with the ratio of diameter:length less than 0.15, which can be regarded as 1D problem.

One-dimensional convection-dispersion equation (CDE) with a deposition term is used to describe the particle transport and retention in saturated porous medium (Corapcioglu et Jiang, 1993):

$$\frac{\partial C}{\partial t} + \frac{\rho_b}{\phi} \frac{\partial S}{\partial t} = D_L \frac{\partial^2 C}{\partial x^2} - u \frac{\partial C}{\partial x} \quad (2.1)$$

where C [M/L³] is the mass concentration of suspended particles in the pore water, t [T] is time, ϕ [L³/L³] is initial porosity, S [M/M] is the mass fraction of deposited particles to porous medium, D_L [L²/T] is the hydrodynamic longitudinal dispersion coefficient, u [M/T] is the average pore velocity, ρ_b [M/L³] is the particle bulk density.

The last term of Eq. (2.1) represents the variation of particle deposition with time. The mass exchange of particles between liquid and solid phase is quantified with the help of some rate coefficients, such as attachment and straining rate.

In this study, reversible-irreversible deposition model was utilized to describe the particle transport, deposition and re-entrainment behavior (Hendry et al., 1997):

$$\frac{\partial S}{\partial t} = \frac{\partial S_{irr}}{\partial t} + \frac{\partial S_r}{\partial t} \quad (2.2a)$$

$$\frac{\rho_b}{\phi} \frac{\partial S_{irr}}{\partial t} = k_{d,irr} C \quad (2.2b)$$

$$\frac{\rho_b}{\phi} \frac{\partial S_r}{\partial t} = k_{d,r} C - k_{r,r} S_r \quad (2.2c)$$

where S_{irr} [M/M] is the “irreversibly” retained particle concentration on the solid phase (particles per unit mass of sand), S_r [M/M] is the “reversibly” retained particle concentration, $k_{d,irr}$ [1/T] is the particle irreversible deposition rate coefficient, $k_{d,r}$ [1/T] is the particle reversible deposition rate coefficient and $k_{r,r}$ [1/T] is the particle re-entrainment rate coefficient. As the amount of retention is little, the porous medium can still be regarded “clean”, thus the deposition and re-entrainment rate coefficients considered constant. Under unfavorable conditions, due to the presence of energy barriers, the amount of deposition sites is very limited relative to favorable conditions. Deposition rates vary with the increase of retention. On the effects of blocking and

ripening, the deposition rate is sometimes time and distance dependent. For instance, the straining model proposed by Bradford et al. (2003),

$$k_d = k_0 \left(1 - \frac{S_{str}}{S_{str}^{max}}\right) \left(\frac{d_g + x}{d_g}\right)^{-\beta} \quad (2.3)$$

where k_0 [1/T] is the initial coefficient of deposition rate, S_{str} [M/M] is strained particle concentration, S_{str}^{max} [M/M] is maximum concentration of strained particles, d_g [L] is porous medium grain median diameter and β [-] is a parameter that controls the shape of the retention profiles. Here, S_{str} increases with time due to blocking, thus k_d decreases with time. The power law function of x describes the effect of straining, leading limited particle transport pore networks with distance.

The concept “reversible/irreversible” does not indicate the deposition mechanisms but reflects the state of deposited particles. Just as the literal meaning, “irreversible” retained particles are entrapped firmly at deposition sites and hardly return to the fluid and move forward; “reversible” retained particles are trapped unstably on the grain surface or contacts and able to get rid of the constraint of grain surface adhesions and leave the near-surface domain, called “reentainment”. However, given absence of chemical and hydrodynamic perturbations, most deposited particles should be approximately in mechanical equilibrium. Except some tiny particles exiting to the fluid on the effects of diffusion, the rest should stay stably at the deposition sites. However, under stable chemical and hydrodynamic conditions, many “reversible” retained particles do not stay a while on the grain surface or contacts, they roll and/or translate across the grain surface. They do not leave the surface due to the secondary energy minimum association with the surface. Although these particles are not really retained temporally by the surface adhesion, their residence times are drastically increased, and the velocities are much lower relative to the fluid flow around. By contrast, in the bulk fluid due to the Taylor dispersion, the particle’s velocity may be greater than flow. Therefore, the velocity distribution of particles is much wider than flow in the macroscopically homogeneous porous media. Fig. 2.1a shows the BTCs of particles and the dissolved tracer. We can obtain the average velocity distributions (Fig. 2.1b) according to the BTCs.

Particles' velocity is not normal distribution but somehow a log-normal one. In CDE, the dispersion term with a constant dispersion coefficient can only achieve normal distributed velocity. Although the “reversible” deposition term with $k_{d,r}$ and $k_{r,r}$ is discrete mathematically and cannot exactly describe the continuous motion of rolling and translating particles across collector surfaces. However, it does realize the redistribution of particle velocities, then being capable of fitting the extended tailings of BTCs.

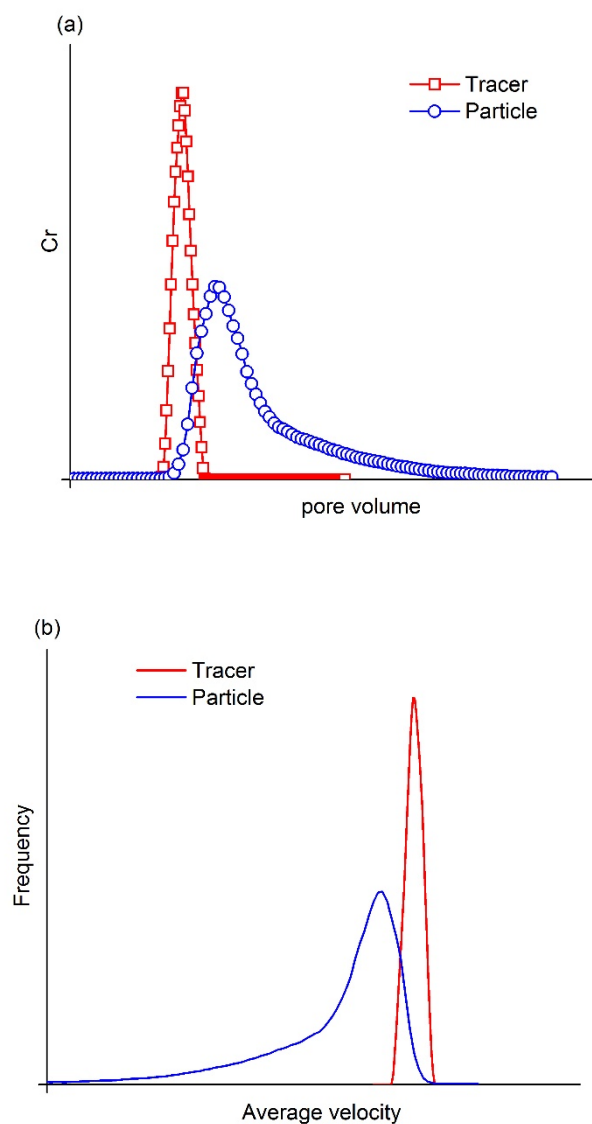


Figure 2.1 (a) Breakthrough curves of tracer and particle; (b) Average velocity distribution of tracer and particle. Adapted from Hammadi et al. [2017]

In the presence of energy barriers, re-entrainment behavior is very sensitive to the solution chemistry and flow rate. Re-entrainment of retained

particles were observed with decrease of ionic strength or increase of flow rate. Thus, mobile or immobile deposition is a relative conception, “irreversible” retained particles can become “reversible”, which needs chemical or hydrodynamic perturbations to break the mechanical equilibrium.

Normally, the transport problem in practice is almost nonlinear, which is complicated and has barely no analytic solution. We often begin with the convection dispersion equation without the source term.

2.2 Analytic and Numerical solutions for 1D convection-dispersion equation

To explore the general analytic and numerical methods of resolving the transport problem, we can begin with the simplest situation, for example, unidimensional transport of contaminants in porous media. Albeit unidimensional problem is easy to be resolved, it is very important in practice to help understanding the transport process of pesticides, pathogens, heavy metals and radionuclides in aquifers.

Mathematic model and analytic resolution

Hypothesis

Considering the transport problem in a semi-infinite column with constant concentration injection at the inlet, 4 hypotheses are proposed for this problem:

- 1) The studied domain is a semi-infinite column of porous medium, which is homogeneous, isotropic and saturated;
- 2) The fluid flow field is stationary, and the average fluid velocity is constant;
- 3) At the initial moment, no contaminant exists in the studied domain;
- 4) From the initial moment, constant concentration of the tracer is injected from the column inlet. The tracer is conservative, there is no adsorption and reaction. The convection and dispersion is

unidimensional.

Mathematic model

This problem can be described mathematically by convection dispersion equation:

$$\frac{\partial C}{\partial t} = D_L \frac{\partial^2 C}{\partial x^2} - u \frac{\partial C}{\partial x} \quad (2.4a)$$

The initial and boundary conditions are:

$$C(x, t)|_{t=0} = 0, x \in [0, +\infty) \quad (2.4b)$$

$$C(x, t)|_{x=0} = C_0, t > 0 \quad (2.4c)$$

$$C(x, t)|_{x \rightarrow +\infty} = 0, t > 0 \quad (2.4d)$$

2.2.1 Analytic solution of convection dispersion equation

This problem can be resolved by the aid of Laplace transformation. The Laplace transformation of C can be expressed:

$$C^*(x, s) = \mathcal{L}(C) = \int_0^\infty C \exp(-st) dt \quad (2.5)$$

Thus equation (2.4a) can be written as:

$$\int_0^\infty \frac{\partial C}{\partial t} \exp(-st) dt = \int_0^\infty D_L \frac{\partial^2 C}{\partial x^2} \exp(-st) dt - \int_0^\infty u \frac{\partial C}{\partial x} \exp(-st) dt \quad (2.6)$$

The term in the left side of equation (2.6) can be written as:

$$\int_0^\infty \frac{\partial C}{\partial t} \exp(-st) dt = sC^* - C|_{t=0} = sC^*$$

The terms in the right side can be written as:

$$\int_0^\infty D_L \frac{\partial^2 C}{\partial x^2} \exp(-st) dt = D_L \frac{\partial^2 C^*}{\partial x^2}, \int_0^\infty u \frac{\partial C}{\partial x} \exp(-st) dt = u \frac{\partial C^*}{\partial x}$$

Then PDE (2.4a) can be transformed to a 2nd order ODE:

$$D_L \frac{\partial^2 C^*}{\partial x^2} - u \frac{\partial C^*}{\partial x} - sC^* = 0 \quad (2.7)$$

The solution can be written as:

$$C^*(x, s) = \exp\left(\frac{ux}{2D_L}\right) \left[A \exp\left(-\frac{x}{2D_L} \sqrt{u^2 + 4D_L s}\right) + B \exp\left(\frac{x}{2D_L} \sqrt{u^2 + 4D_L s}\right) \right]$$

$$(2.8)$$

According to the boundary condition (2.4d), when $x = \infty$, $C = 0$, $C^* = 0$, thus $B = 0$. Then with the boundary condition (2.4c), when $x = 0$, $C = 0$, then

$$C^*|_{x=0} = \int_0^{\infty} C_0 \exp(-st) dt = \frac{C_0}{s}$$

thus $A = \frac{C_0}{s}$, then Eq 2.8 varies to

$$C^*(x, s) = \frac{C_0}{s} \exp\left(\frac{ux}{2D_L} - \frac{x}{2D_L} \sqrt{u^2 + 4D_L s}\right) \quad (2.9)$$

Accord to the inverse Laplace transformation, we can obtain the analytical resolution of the contaminant transport problem in the semi-infinite column:

$$C(x, t) = \frac{C_0}{2} \left[\operatorname{erfc}\left(\frac{x-ut}{2\sqrt{D_L t}}\right) + \exp\left(\frac{ux}{D_L}\right) \operatorname{erfc}\left(\frac{x+ut}{2\sqrt{D_L t}}\right) \right] \quad (2.10)$$

When the pecllet number $P_e = \frac{ux}{D_L} > 200$, we can neglect the second term on the right side of Eq (2.10). Then the resolution can be approximated as:

$$C = \frac{C_0}{2} \operatorname{erfc}\left(\frac{x-ut}{2\sqrt{D_L t}}\right) \quad (2.11)$$

2.2.2 Numerical solution of convection dispersion equation

Most of numerical methods for solving convection-dispersion equation can be categorized as Eulerian method, Lagrangian method and Eulerian Lagrangian method (Neuman, 1984; Baptista, 1987). Eulerian method solves transport equation at fixed space grid points. The solution method mainly includes finite element method and finite difference method. Euler method is very effective in water flow modeling, as one of the earliest methods employed in transport modeling, which is still widely used. Eulerian method's advantages and convenience is that with fixed grids, it usually meets the law of conservation of mass, and can accurately and efficiently deal with the dispersion dominated problem. However, as to the convection dominated problem, solving with Eulerian method easily brings about great numerical dispersions and oscillations (Pinder and Gray, 1977; Anderson, 1979).

Lagrangian method does not directly solve particle transport PDE. By contrast, this method uses a large number of moving particles approaching convection and dispersion. Lagrangian method can accurately and effectively solve convection dominated problems and practically eliminate numerical dispersion (Pricket et al., 1981; Kinzelbach, 1986; Tompson and Gelhar, 1990). However, due to lack of fixed modeling grids or coordinate system, Lagrange method would bring out numerical instability and calculation difficulty, especially for inhomogeneous porous media with several sources/sinks and complex boundary conditions (Yeh, 1990).

Mixed Eulerian-Lagrangian method attempts to associate the advantages of the previously mentioned two methods, it uses Lagrange method to solve convection term and Eulerian method to treat dispersion and other terms. However, some frequently used mixed E-L method, e.g. characteristic curve method, do not satisfy mass conservation principal.

In this work, finite difference method was employed to realize modeling of unidimensional particle transport problems. In our simulations, single running time of the program is about 30 *second* to 1 *min* for a home PC according to the mesh size. In contrast, a similar simulation needs 8 hours using the program with particle methods, coded by our group before (Wang et al., 2014). Thanks to such short single running time, identification of parameters in the transport-deposition-reentrainment model can be realized by inverse method within an acceptable time.

Simulations with finite difference method

Analytical solutions of convection dispersion equation involve closed-form expressions which gives the variation of the dependent variables continuously throughout the domain. In contrast, numerical solutions can give answers to only discrete points in the domain, called grid points. For example, consider Figure 2.2, which shows a section of a discrete grid in the x-t plane.

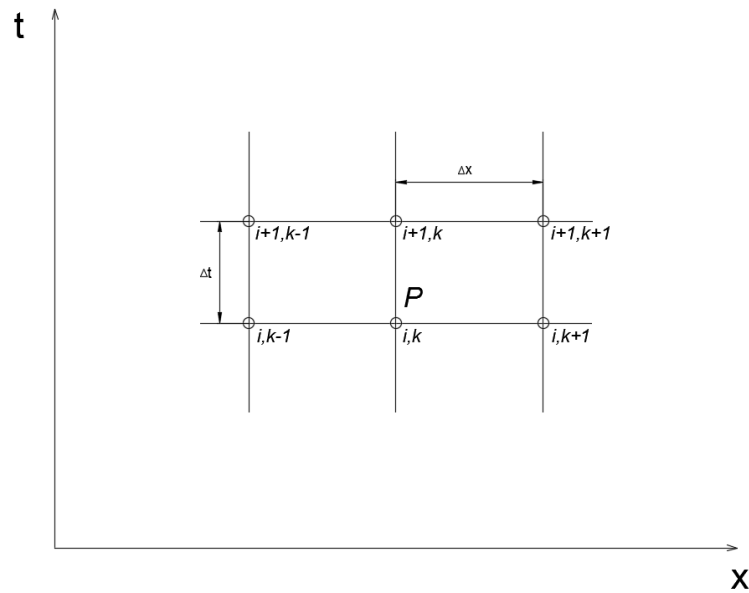


Figure 2.2 Discrete grid points

Discretization

Here, we are interested in replacing a partial derivative with a suitable algebraic difference quotient. Most common finite-difference representations of derivatives are based on Taylor's series expansions. In the convection dispersion equation, we have three partial derivative terms, two first derivative $\frac{\partial C}{\partial t}$ and $\frac{\partial C}{\partial x}$, one second derivative, $\frac{\partial^2 C}{\partial x^2}$.

Discretization in time

C_i^k donates the tracer concentration in the pore fluid at position $i\Delta x$ at time $k\Delta t$, then C_i^{k+1} at time $(k+1)\Delta t$ can be expressed in terms of a Taylor series expanded about (i, k) as follows:

$$C_i^{k+1} = C_i^k + \left(\frac{\partial C}{\partial t}\right)_i^k \Delta t + \left(\frac{\partial^2 C}{\partial t^2}\right)_i^k \frac{(\Delta t)^2}{2} + \dots \quad (2.12)$$

Equation is mathematically an exact expression for C_i^{k+1} if 1) the number of terms is infinite, and the series converges and/or 2) $\Delta t \rightarrow 0$.

Solving Eq. for $\left(\frac{\partial C}{\partial t}\right)_i^k$, we obtain

$$\left(\frac{\partial C}{\partial t}\right)_i^k = \frac{C_i^{k+1} - C_i^k}{\Delta t} - \left(\frac{\partial^2 C}{\partial t^2}\right)_i^k \frac{\Delta t}{2} + \dots \quad (2.13)$$

The first term on the right side is a finite difference representation of the partial derivative. The remaining terms on the right side constitute the truncation error. We can also write it as:

$$\left(\frac{\partial C}{\partial t}\right)_i^k = \frac{C_i^{k+1} - C_i^k}{\Delta t} + \mathcal{O}(\Delta t) \quad (2.14)$$

The symbol $\mathcal{O}(\Delta t)$ is a formal mathematical notation which represents “terms of order Δt ”.

If we neglect the terms of order, we can get approximate expression:

$$\left(\frac{\partial C}{\partial t}\right)_i^k \approx \frac{C_i^{k+1} - C_i^k}{\Delta t} \quad (2.15)$$

Similarly, C_{i+1}^k and C_{i-1}^k can be expressed as follows:

$$C_{i+1}^k = C_i^k + \left(\frac{\partial C}{\partial x}\right)_i^k \frac{\partial C}{\partial x} \Delta x + \left(\frac{\partial^2 C}{\partial x^2}\right)_i^k \frac{(\Delta x)^2}{2} + \left(\frac{\partial^3 C}{\partial x^3}\right)_i^k \frac{(\Delta x)^3}{6} + \left(\frac{\partial^4 C}{\partial x^4}\right)_i^k \frac{(\Delta x)^4}{24} + \dots (2.16)$$

$$C_{i-1}^k = C_i^k - \left(\frac{\partial C}{\partial x}\right)_i^k \frac{\partial C}{\partial x} \Delta x + \left(\frac{\partial^2 C}{\partial x^2}\right)_i^k \frac{(\Delta x)^2}{2} - \left(\frac{\partial^3 C}{\partial x^3}\right)_i^k \frac{(\Delta x)^3}{6} + \left(\frac{\partial^4 C}{\partial x^4}\right)_i^k \frac{(\Delta x)^4}{24} + \dots (2.17)$$

Solving Eq. 2.14 for $\left(\frac{\partial C}{\partial x}\right)_i^k$, we can get

$$\left(\frac{\partial C}{\partial x}\right)_i^k = \frac{C_{i+1}^k - C_i^k}{\Delta x} + \mathcal{O}(\Delta x) \quad (2.18)$$

Here this expression uses the information to the right of grid point (i,j) (Fig. 2.2); that is, it uses C_{i+1}^k and C_i^k . No information to the left of (i,j) is used. Therefore, the finite difference expression in Eq. 2.18 is called a forward difference.

Solving Eq. 2.17, we can get

$$\left(\frac{\partial C}{\partial x}\right)_i^k = \frac{C_i^k - C_{i-1}^k}{\Delta x} + \mathcal{O}(\Delta x) \quad (2.19)$$

Correspondingly, here this expression only uses the information to the left of (i,j) and it is called a rearward difference.

Here, we can find that both forward and rearward difference expressions have first-order accuracy.

If we subtract Eq. 2.16 by Eq. 2.17, after simplification we can get

$$\left(\frac{\partial C}{\partial x}\right)_i^k = \frac{C_{i+1}^k - C_{i-1}^k}{2\Delta x} + \mathcal{O}(\Delta x)^2 \quad (2.20)$$

This expression uses the information to both left and right of (i,j) and has second-order accuracy. It is called central difference.

To obtain the solution of the second derivative $\left(\frac{\partial^2 C}{\partial x^2}\right)_i^k$, we can add Eq. 2.16 by Eq. 2.17

$$\left(\frac{\partial^2 C}{\partial x^2}\right)_i^k = \frac{C_{i+1}^k - 2C_i^k + C_{i-1}^k}{(\Delta x)^2} + \mathcal{O}(\Delta x)^2 \quad (2.21)$$

This expression has second-order accuracy.

Let us write Eq. (2.1) as:

$$\frac{\partial C}{\partial t} + u \frac{\partial C}{\partial x} - D_L \frac{\partial^2 C}{\partial x^2} = 0 \quad (2.22)$$

Inserting Eqs. (2.14), (2.20) and (2.21), we have

$$\frac{C_i^{k+1} - C_i^k}{\Delta t} + u \frac{C_{i+1}^k - C_{i-1}^k}{2\Delta x} - D_L \frac{C_{i+1}^k - 2C_i^k + C_{i-1}^k}{(\Delta x)^2} = \mathcal{O}(\Delta t) + \mathcal{O}(\Delta x)^2 \quad (2.23)$$

Using $\epsilon_L = \mathcal{O}(\Delta t) + \mathcal{O}(\Delta x)^2$ to represent truncation error, we have

$$\frac{C_i^{k+1} - C_i^k}{\Delta t} + u \frac{C_{i+1}^k - C_{i-1}^k}{2\Delta x} - D_L \frac{C_{i+1}^k - 2C_i^k + C_{i-1}^k}{(\Delta x)^2} = \epsilon_L \quad (2.24)$$

ϵ_L can also expressed as:

$$\epsilon_L = -\left(\frac{\partial^2 C}{\partial t^2}\right)_i^k \frac{\Delta t}{2} + u \frac{\partial^2 C}{\partial x^2} \frac{(\Delta x)^2}{2} - D_L \frac{\partial^4 C}{\partial x^4} \frac{(\Delta x)^2}{12} \sim \mathcal{O}[\Delta t, (\Delta x)^2] \quad (2.25)$$

Writing just the difference equation from Eq. (2.24)

$$\frac{C_i^{k+1} - C_i^k}{\Delta t} = -u \frac{C_{i+1}^k - C_{i-1}^k}{2\Delta x} + D_L \frac{C_{i+1}^k - 2C_i^k + C_{i-1}^k}{(\Delta x)^2} \quad (2.26)$$

With some rearrangement, this equation can be written as

$$C_i^{k+1} = C_i^k - \frac{u\Delta t}{2\Delta x} (C_{i+1}^k - C_{i-1}^k) + \frac{D_L \Delta t}{(\Delta x)^2} (C_{i+1}^k - 2C_i^k + C_{i-1}^k) \quad (2.27)$$

It uses the information to three points at k time step to get the resolution at $k+1$ step (Fig. 2.3a). This is called explicit approach.

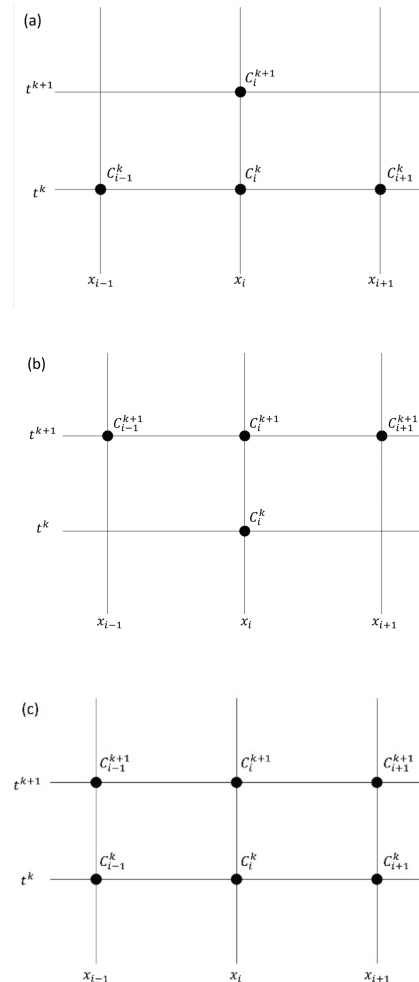


Figure 2.3 (a) An explicit finite-difference module; (b) an implicit finite-difference module; (c) A finite-difference module of Crank-Nicolson method

We can also use the information to 3 points at $k+1$ step and 1 point at k step and get

$$\frac{C_i^{k+1} - C_i^k}{\Delta t} = -U \frac{C_{i+1}^{k+1} - C_{i-1}^{k+1}}{2\Delta x} + D_L \frac{C_{i+1}^{k+1} - 2C_i^{k+1} + C_{i-1}^{k+1}}{(\Delta x)^2} \quad (2.28)$$

This is the simplest form of implicit approach (Fig. 2.3b).

For another usually used implicit approach, also called Crank-Nicolson method (Fig. 2.3c), it is written as:

$$\frac{C_i^{k+1}-C_i^k}{\Delta t} = -\frac{U}{2} \left[\frac{C_{i+1}^{k+1}-C_{i-1}^{k+1}}{2\Delta x} + \frac{C_{i+1}^k-C_{i-1}^k}{2\Delta x} \right] + \frac{D_L}{2} \left[\frac{C_{i+1}^{k+1}-2C_i^{k+1}+C_{i-1}^{k+1}}{(\Delta x)^2} + \frac{C_{i+1}^k-2C_i^k+C_{i-1}^k}{(\Delta x)^2} \right] \quad (2.29)$$

it uses the information to 3 points at k step and 3 points at $k+1$ step.

For explicit approach, we can obtain directly the solution of $k+1$ step using the results of k step. By contrast, as to implicit approaches, we must use iterative method. For convection dominated CDE like our problem, we can use chasing method to solve the equations.

Errors and stability analysis (Fourier analysis)

We recalled Eq. (2.4a),

$$\frac{\partial C}{\partial t} = D_L \frac{\partial^2 C}{\partial x^2} - u \frac{\partial C}{\partial x} \quad (2.4a)$$

And for the difference representation of this equation we choose the explicit central form (Eq. (2.26))

$$\frac{C_i^{k+1}-C_i^k}{\Delta t} = -u \frac{C_{i+1}^k-C_{i-1}^k}{2\Delta x} + D_L \frac{C_{i+1}^k-2C_i^k+C_{i-1}^k}{(\Delta x)^2} \quad (2.26)$$

The error is the difference between the solutions numerical and exact, $\epsilon_i^k = C_i^k - C_{ex}(k\Delta t, i\Delta x)$.

Exact solution also satisfies Eq. (2.26), thus we can derivate

$$\frac{\epsilon_i^{k+1}-\epsilon_i^k}{\Delta t} = -U \frac{\epsilon_{i+1}^k-\epsilon_{i-1}^k}{2\Delta x} + D_L \frac{\epsilon_{i+1}^k-2\epsilon_i^k+\epsilon_{i-1}^k}{(\Delta x)^2} \quad (2.30)$$

To ensure the stability of the solution, ϵ_i should be shrink or at least stay the same as the solution progress from step k to $k+1$. That is,

$$\left| \frac{\epsilon_i^{k+1}}{\epsilon_i^k} \right| \leq 1 \quad (2.31)$$

The solution of Eq. (2.30) can be expressed analytically by a Fourier series as follows:

$$\epsilon(x, t) = \sum_m A_m(t) e^{Ik_m x} \quad (2.32)$$

Where A_m is amplitude factor, k_m is called the wave number. It is reasonable to assume an exponential variation with time; errors tend to grow or diminish exponentially with time. Therefore, we can rewrite Eq. (2.30) as:

$$\epsilon(x, t) = \sum_m e^{at} e^{Ik_m x} \quad (2.33)$$

The behavior of each term of the series is the same as the series itself. Hence, we can deal with just one term of the series,

$$\epsilon_m(x, t) = e^{at} e^{Ik_m x} \quad (2.34)$$

Then introduce Eq. (2.34) into Eq. (2.30)

$$\frac{e^{a(t+\Delta t)} e^{Ik_m x} - e^{at} e^{Ik_m x}}{\Delta t} = -U \frac{e^{at} e^{Ik_m(x+\Delta x)} - e^{at} e^{Ik_m(x-\Delta x)}}{2\Delta x} + D_L \frac{e^{at} e^{Ik_m(x+\Delta x)} - 2e^{at} e^{Ik_m x} + e^{at} e^{Ik_m(x-\Delta x)}}{(\Delta x)^2} \quad (2.35)$$

Divide Eq. (2.35) by $e^{at} e^{Ik_m x}$

$$\frac{e^{a\Delta t} - 1}{\Delta t} = -u \frac{e^{Ik_m \Delta x} - e^{-Ik_m \Delta x}}{2\Delta x} + D_L \frac{e^{Ik_m \Delta x} - 2 + e^{-Ik_m \Delta x}}{(\Delta x)^2} \quad (2.36)$$

To simplify the equation, we introduce two following dimensionless number $\alpha = \frac{u\Delta t}{\Delta x}$, $\beta = \frac{D_L \Delta t}{(\Delta x)^2}$. After simple rearrangement, we have

$$e^{a\Delta t} = 1 - 2\beta + \beta(e^{Ik_m \Delta x} + e^{-Ik_m \Delta x}) - \frac{\alpha}{2}(e^{Ik_m \Delta x} - e^{-Ik_m \Delta x}) \quad (2.37)$$

Recalling the trigonometric identity $e^{Ik_m \Delta x} + e^{-Ik_m \Delta x} = 2\cos(k_m \Delta x)$ and $e^{Ik_m \Delta x} - e^{-Ik_m \Delta x} = 2I\sin(k_m \Delta x)$, then Eq. (2.37) varies to

$$e^{a\Delta t} = 1 + 2\beta(\cos(k_m \Delta x) - 1) - \alpha I \sin(k_m \Delta x) \quad (2.38)$$

The amplitude factor is

$$G = \left| \frac{\epsilon_i^{k+1}}{\epsilon_i^k} \right| = e^{a\Delta t} \quad (2.39)$$

Introducing $y = \cos(m\Delta x)$ to Eq. (2.38), we can get

$$G^2(y) = \left\| \frac{\epsilon_i^{k+1}}{\epsilon_i^k} \right\|^2 = (1 + 2\beta(y - 1))^2 + \alpha^2(1 - y^2), \quad y \in [-1, 1] \quad (2.40)$$

Thus, $G^2(-1) = (4\beta - 1)^2$, $G^2(1) = 1$.

the derivative is

$$\frac{dG^2}{dy} = (8\beta^2 - 2\alpha^2)y - 4\beta(2\beta - 1) \quad (2.41)$$

It is equal to $\frac{dG^2}{dy}(1) = 4\beta - 2\alpha^2$ with $y=1$.

To make sure $G^2(y) < 1$ within $y \in [-1,1]$, it should satisfy the following conditions:

$G^2(-1) < 1$ and $\frac{dG^2}{dy}(1) \geq 0$ which are equivalent to $2\beta \geq \alpha^2$ and $2\beta \leq 1$, then $\alpha^2 \leq 2\beta \leq 1$.

Finally, we obtain the stable condition:

$$\begin{cases} \frac{D_L dt}{(\Delta x)^2} \leq \frac{1}{2} \\ \frac{u^2 dt}{D_L} \leq 2 \end{cases} \quad (2.42)$$

Oscillation of convection dominated problems

As known, a numerical solution for the convection-dispersion equation needs to deal with the convection part of the governing equation in addition to diffusion. When numerical Peclet number (P_e^{num}) exceeds a certain value, the spurious oscillations result in space.

For a given constant spatial increment Δx and a time step Δt , Eq. (2.22) may be rewritten in a general discretized form using the finite difference algorithm (Wang and Lacroix, 1997):

$$\frac{C_i^{k+1} - C_i^k}{\Delta t} + \{u[\kappa\Delta_x^- + (1 - \kappa)\Delta_x^+] - D_L\Delta_{xx}\}[\theta C_i^{k+1} + (1 - \theta)C_i^k] = 0 \quad (2.43)$$

Where the mathematical operator symbols Δ_x^- , Δ_x^+ and Δ_{xx} are defined by

$$\begin{cases} \Delta_x^- C_i = (C_i - C_{i-1})/\Delta x \\ \Delta_x^+ C_i = (C_{i+1} - C_i)/\Delta x \\ \Delta_{xx} C_i = (C_{i+1} - 2C_i + C_{i-1})/\Delta x^2 \end{cases} \quad (2.44)$$

θ is the time weighting coefficient ($0 \leq \theta \leq 1$); κ is the spatial weighting coefficient ($0 \leq \kappa \leq 1$). Three numerical schemes ($\kappa = 0.5, 0.65$ and 1) are realized and compared with the exact solutions with different numerical Peclet

number ($P_e^{num} = 2$ and 25). As $\kappa = 0.5$, the convection term is discretized using central difference form. As $\kappa = 1$, the convection term is discretized using forward difference form. With the low Peclet number ($P_e^{num} = 2$), all three numerical results are accurate enough to be considered satisfactory (Fig. 2.4a). In contrast, when the Peclet number is high ($P_e^{num} = 25$) (Fig.2.4b), the space-centred scheme ($\kappa = 0.5$) shows a strong numerical oscillation. The upwind scheme ($\kappa = 1$) is still stable, but an important numerical dispersion appears. With $\kappa = 0.65$, we obtain intermediate results between the above two schemes.

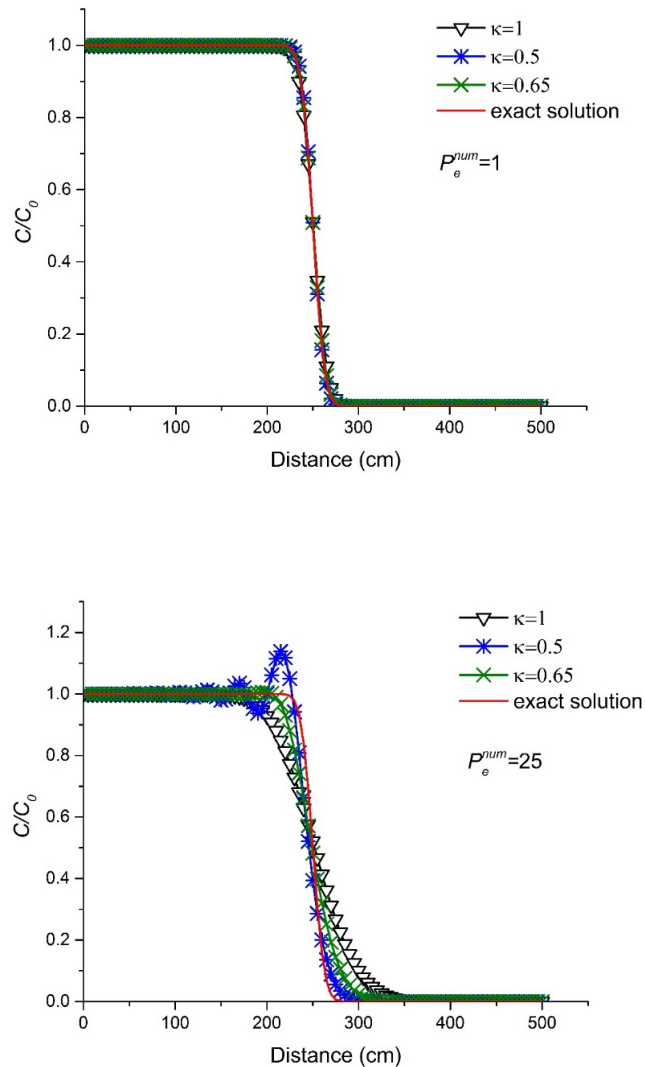


Figure 2.4 Comparisons of the exact and numerical solutions of a one-dimensional transport with a boundary condition of a continuous injection with (a) a low Peclet number ($P_e^{num} = 2$) and (b) a high Peclet number ($P_e^{num} = 25$).

2.3 Numerical solutions of transport and deposition problems

Based on the study of numerical solution of convection dispersion equation, in this thesis, we can apply the similar method to resolve the transport and deposition problems. Recall the equations 2.1 and 2.2,

$$\frac{\partial C}{\partial t} = D_L \frac{\partial^2 C}{\partial x^2} - u \frac{\partial C}{\partial x} - \frac{\rho_b}{\phi} \frac{\partial S}{\partial t} \quad (2.1)$$

$$\frac{\partial S}{\partial t} = \frac{\partial S_{irr}}{\partial t} + \frac{\partial S_r}{\partial t} \quad (2.2a)$$

$$\frac{\rho_b}{\phi} \frac{\partial S_{irr}}{\partial t} = k_{d,irr} C \quad (2.2b)$$

$$\frac{\rho_b}{\phi} \frac{\partial S_r}{\partial t} = k_{d,r} C - k_{r,r} S_r \quad (2.2c)$$

According to the equation 2.43, the equations 2.1 and 2.2 can be rewritten using the finite different scheme:

$$\frac{C_i^{k+1} - C_i^k}{\Delta t} + \{u[\kappa \Delta_x^- + (1 - \kappa) \Delta_x^+] - D_L \Delta_{xx}\} [\theta C_i^{k+1} + (1 - \theta) C_i^k] = - \frac{\rho_b (S_i^{k+1} - S_i^k)}{\phi \Delta t} \quad (2.45a)$$

$$\frac{\rho_b (S_i^{k+1} - S_i^k)}{\phi \Delta t} = \frac{\rho_b (S_{irr,i}^{k+1} - S_{irr,i}^k)}{\phi \Delta t} + \frac{\rho_b (S_{r,i}^{k+1} - S_{r,i}^k)}{\phi \Delta t} \quad (2.45b)$$

$$\frac{\rho_b (S_{irr,i}^{k+1} - S_{irr,i}^k)}{\phi \Delta t} = k_{d,irr} C_i^{k+1} \quad (2.45c)$$

$$\frac{\rho_b (S_{r,i}^{k+1} - S_{r,i}^k)}{\phi \Delta t} = k_{d,r} C_i^{k+1} - k_{r,r} S_{r,i}^{k+1} \quad (2.45d)$$

The concentration and retention of each time step are calculated by the iterative method.

2.4 Optimization scheme for identification of model parameters

After developing the finite difference scheme, we need the optimization tool to obtain best-fitted values of parameters in the model. Modelling approaches involve curving-fitting testing data, and in our case, we have BTC and retained profiles. Such curve-fitting is mathematically a non-linear least-squares problem. Standard methods like the Levenberg-Marquadt (LM) method (Levenberg, 1944; Marquadt, 1963) are usually employed for non-linear curve-fitting to realize parameter identification.

In our study, we usually need to fit the BTC curves to obtain the values of kinetic rates and hydrodynamic coefficients. The BTC curve exhibits the evolution of column effluent particle concentration with time. The concentration C is therefore a function of time, t .

In fitting the simulated concentration $\hat{C}(t_i; \mathbf{p})$ of injection time t and a vector of n parameters \mathbf{p} to a set of m measured data points (t_i, C_i) , it is customary and convenient to minimize the sum of the weighted squares of the errors between the measured data $C(t_i)$ and the curve-fit $\hat{C}(t_i; \mathbf{p})$. This is scalar-valued goodness of fit measure is called the chi-squared error criterion, written as:

$$\chi^2(\mathbf{p}) = \sum_{i=1}^m [f_i(\mathbf{p})]^2 = \|\mathbf{f}(\mathbf{p})\|^2 = \mathbf{f}(\mathbf{p})^T \mathbf{f}(\mathbf{p}). \quad (2.46)$$

And $f_i(\mathbf{p}) = f(t_i; \mathbf{p}) = \frac{C(t_i) - \hat{C}(t_i; \mathbf{p})}{\omega_i}$, where the value ω_i is a measure of the error in measurement $C(t_i)$. For BTC curve, the minimization of χ^2 with respect to the physical parameters in the transport and deposition model needs to be carried out iteratively. The goal of each iteration is to find a perturbation \mathbf{h} to the parameters \mathbf{p} that reduces χ^2 ; that is, $\mathbf{p}^* = \operatorname{argmin}_{\mathbf{x}} \{\chi^2(\mathbf{p})\}$.

Provided that f has continuous second partial derivatives, we can write its Taylor expansion as

$$\mathbf{f}(\mathbf{p} + \mathbf{h}) = \mathbf{f}(\mathbf{p}) + \mathbf{J}(\mathbf{p})\mathbf{h} + \mathcal{O}(\|\mathbf{h}\|^2) \quad (2.47)$$

where $\mathbf{J} \in \mathbf{R}^{m \times n}$ is the Jacobian. This is a matrix containing the first partial derivatives of the function components,

$$(\mathbf{J}(\mathbf{p}))_{ij} = \frac{\partial f_i}{\partial p_j}(\mathbf{p}) \quad (2.48)$$

The partial derivatives of χ^2 is

$$\frac{\partial \chi^2}{\partial p_j}(\mathbf{p}) = \sum_{i=1}^m f_i(\mathbf{p}) \frac{\partial f_i}{\partial p_j}(\mathbf{p}) \quad (2.49)$$

Thus, the gradient is

$$\chi^{2'} = \mathbf{J}(\mathbf{p})^T \mathbf{f}(\mathbf{p}) \quad (2.50)$$

For small $\|\mathbf{h}\|$ we see from the the Taylor expansion that

$$\mathbf{f}(\mathbf{p} + \mathbf{h}) \simeq \boldsymbol{\ell}(\mathbf{h}) \equiv \mathbf{f}(\mathbf{p}) + \mathbf{J}(\mathbf{p})\mathbf{h} \quad (2.51)$$

Then we can get the approximate equation of the Taylor expansion of

$$\begin{aligned} \chi^2(\mathbf{p} + \mathbf{h}) &\simeq \mathcal{L}(\mathbf{h}) \equiv \boldsymbol{\ell}(\mathbf{p})^T \boldsymbol{\ell}(\mathbf{p}) \\ &= \mathbf{f}^T \mathbf{f} + 2\mathbf{h}^T \mathbf{J}^T \mathbf{f} + \mathbf{h}^T \mathbf{J}^T \mathbf{J} \mathbf{h} \\ &= \chi^2(\mathbf{p}) + 2\mathbf{h}^T \mathbf{J}^T \mathbf{f} + \mathbf{h}^T \mathbf{J}^T \mathbf{J} \mathbf{h} \end{aligned} \quad (2.52)$$

The Gauss-Newton step \mathbf{h}_{gn} minimizes $\mathcal{L}(\mathbf{h})$,

$$\mathbf{h}_{gn} = \operatorname{argmin}_{\mathbf{h}} \{\mathcal{L}(\mathbf{h})\} \quad (2.53)$$

It is easily seen that the gradient

$$\mathcal{L}'(\mathbf{h}) = \mathbf{J}^T \mathbf{f} + \mathbf{J}^T \mathbf{J} \mathbf{h} \quad (2.54)$$

The minimizer of $\mathcal{L}(\mathbf{h})$ can be found by solving

$$[\mathbf{J}^T \mathbf{J}] \mathbf{h}_{gn} = -\mathbf{J}^T \mathbf{f} \quad (2.55)$$

Now we insert $C(t_i)$ and $\hat{C}(t_i; \mathbf{p})$

$$(\mathbf{J}(\mathbf{p}))_{ij} = \frac{\partial f_i}{\partial p_j}(\mathbf{p}) = \frac{\frac{1}{\omega_i} \partial(C(t_i) - \hat{C}(t_i; \mathbf{p}))}{\partial p_j} \quad (2.56)$$

$$(\mathbf{J}_c(\mathbf{p}))_{ij} = \frac{\partial \hat{C}(t_i; \mathbf{p})}{\partial p_j} \quad (2.67)$$

then

$$\mathbf{J}^T \mathbf{J} = \mathbf{J}_c^T \mathbf{W} \mathbf{J}_c \quad (2.58)$$

The weighting matrix \mathbf{W} is diagonal with $W_{ii} = 1/\omega_i^2$

$$\mathbf{J}^T \mathbf{f} = -\mathbf{J}_c^T \mathbf{W} (\mathbf{c} - \hat{\mathbf{c}}) \quad (2.59)$$

The resulting normal equations for the Gauss-Newton perturbation are

$$[\mathbf{J}_c^T \mathbf{W} \mathbf{J}_c] \mathbf{h}_{gn} = \mathbf{J}_c^T \mathbf{W} (\mathbf{c} - \hat{\mathbf{c}}) \quad (2.60)$$

The Levenberg-Marquardt algorithm adaptively varies the parameter updates between the gradient descent update and the Gauss-Newton update,

$$[\mathbf{J}_c^T \mathbf{W} \mathbf{J}_c + \lambda \text{diag}(\mathbf{J}_c^T \mathbf{W} \mathbf{J}_c)] \mathbf{h}_{lm} = \mathbf{J}_c^T \mathbf{W} (\mathbf{c} - \hat{\mathbf{c}}) \quad (2.61)$$

where small values of the algorithmic parameter λ result in a Gauss-Newton update and large values of λ result in a gradient descent update. The parameter λ is initialized to be large. If an iteration happens to result in a worse approximation, λ is increased. As the solution approaches the minimum, λ is decreased, the Levenberg-Marquardt method approaches the Gauss-Newton method, and the solution typically converges rapidly to the local minimum.

2.4.1 Numerical Implementation

Initialization and update of the L-M parameter,

In each iteration i , the step \mathbf{h} is evaluated by comparing $\chi^2(\mathbf{p})$ to $\chi^2(\mathbf{p} + \mathbf{h})$. The step is accepted if ρ_i , defined in following, is greater than a user-specified value, ϵ_4 ,

$$\rho_i(\mathbf{h}) = (\chi^2(\mathbf{p}) - \chi^2(\mathbf{p} + \mathbf{h})) / \left(2\mathbf{h}^T \left(\lambda_i \mathbf{h} + \mathbf{J}_c^T \mathbf{W} (\mathbf{c} - \hat{\mathbf{c}}(\mathbf{p})) \right) \right) \quad (2.62)$$

If in an iteration $\rho_i(\mathbf{h}) > \epsilon_4$ then $\mathbf{p} + \mathbf{h}$ is sufficiently better than \mathbf{p} , \mathbf{p} is replaced by $\mathbf{p} + \mathbf{h}$, and λ is reduced by a factor. Otherwise λ is increased by a factor, and the algorithm proceeds to the next iteration. That is,

$$\text{if } \rho_i(\mathbf{h}) > \epsilon_4: \mathbf{p} \leftarrow \mathbf{p} + \mathbf{h}; \lambda_{i+1} = \max[\lambda_i/L, 10^{-7}];$$

$$\text{Otherwise: } \lambda_{i+1} = \min[\lambda_i L, 10^7].$$

Convergence criteria

Convergence is achieved when one of the following three criteria is satisfied,

1. Convergence in the gradient, $\max|\mathbf{J}_c^T \mathbf{W}(\mathbf{C} - \hat{\mathbf{C}})| < \epsilon_1$;
2. Convergence in parameters, $\max|h_i/p_i| < \epsilon_2$; or
3. Convergence in χ^2 , $\chi^2/(m - n + 1) < \epsilon_3$.

Otherwise, iterations terminate when the iteration count exceeds a pre-specified limit.

Error Analysis

Once the optimal curve-fit parameters \mathbf{p}_{fit} are determined, parameter statistics are computed for the converged solution using weight values, ω_i^2 , equal to the mean square measurement error, σ_c^2 ,

$$\omega_i^2 = \sigma_c^2 = \frac{1}{m-n-1} (\mathbf{C} - \hat{\mathbf{C}}(\mathbf{p}_{\text{fit}}))^T (\mathbf{C} - \hat{\mathbf{C}}(\mathbf{p}_{\text{fit}})) \quad (2.63)$$

The parameter covariance matrix is then computed from

$$\mathbf{V}_p = [\mathbf{J}_c^T \mathbf{W} \mathbf{J}_c]^{-1} \quad (2.64)$$

The asymptotic standard parameter error is a measure of how unexplained variability in the data propagates to variability in the parameters, and is essentially an error measure for the parameters. The standard error of the fit is given by

$$\sigma_p = \sqrt{\text{diag}([\mathbf{J}_c^T \mathbf{W} \mathbf{J}_c]^{-1})}. \quad (2.65)$$

The standard error of the fit indicates how variability in the parameters affects the variability in the parameters and is essentially an error measure for the parameters. The standard error of the fit is given by

$$\sigma_{\hat{\mathbf{C}}} = \sqrt{\text{diag}(\mathbf{J}_c [\mathbf{J}_c^T \mathbf{W} \mathbf{J}_c]^{-1} \mathbf{J}_c^T)} \quad (2.66)$$

2.5 Inverse method algorithm

After the development of simulation and optimization methods, we can construct a complete program (with **matlab**) of inverse method and obtain best-fitted parameter values with the input of experimental measurements. The following diagram presents the flow chart of inverse method algorithm:

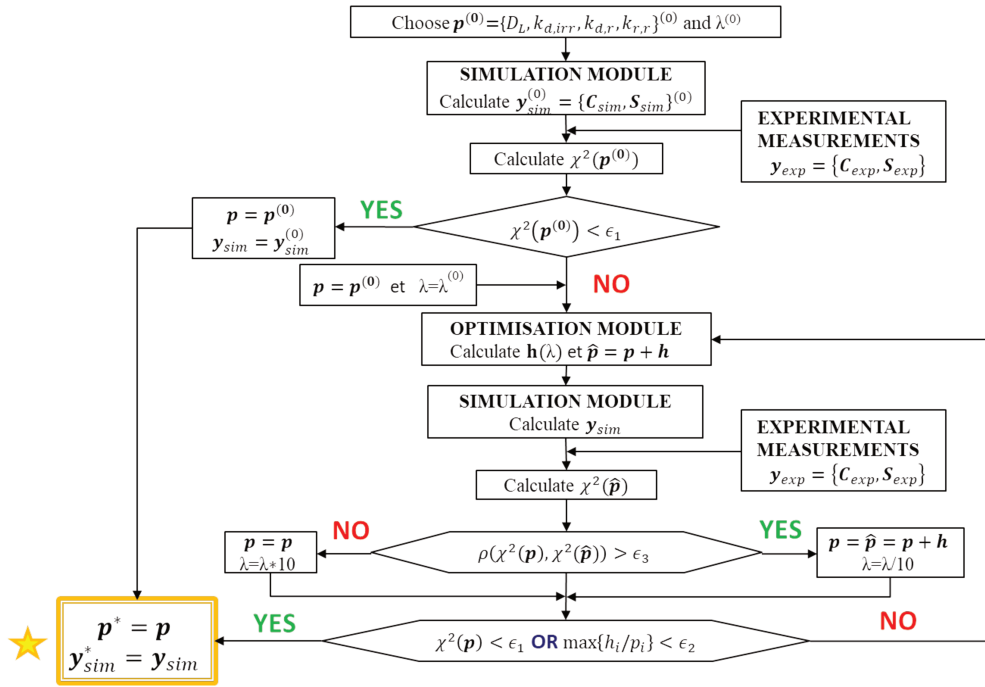


Figure 2.5 Flow chart of inverse method algorithm

2.5.1 Program testing

The robustness of the LM least square code is tested by BTC curving-fitting of a simulated pulse input. The porous media column with the length of 32 cm and the diameter of 4 cm is used. The porosity is 0.393. For the suspension, the injected concentration is 6 g/l and the injected volume is 1 ml. The flow rate is 20 ml/min. Following the pulse injection of colloid suspension, 4 pore volume deionized water is injected. The values of these experimental parameters refer to the pulse-input experiments conducted by Hammadi (2016).

We recall the convection-dispersion equation with deposition term,

$$\frac{\partial C}{\partial t} + \frac{\rho_b}{\phi} \frac{\partial S}{\partial t} = D_L \frac{\partial^2 C}{\partial x^2} - U \frac{\partial C}{\partial x} \quad (2.45)$$

To simplify the problem, we do not consider the immobile deposition, and only two kinetic parameters are employed. The deposition term therefore is expressed as:

$$\frac{\rho_b}{\phi} \frac{\partial S}{\partial t} = k_d C - k_r S \quad (2.46)$$

Experimental measurements are simulated by the breakthrough curve with a set of “true” parameter values. Two hundred measurements ($m=200$) are collected from the BTC. Three parameters ($n=3$) are identified, D_L , k_d and k_r , therefore the vector $p = (p_1, p_2, p_3)$.

The “true” parameter values p_{true} , the initial parameter values $p_{initial}$, resulting curve-fit parameter values p_{fit} and standard errors of the fit parameters σ_p are shown in Table 2.1. The true parameter values lie within the confidence interval $p_{fit} - 1.96 \sigma_p < p_{true} < p_{fit} + 1.96 \sigma_p$. The R^2 fit criterion is 98 percent. The standard parameter errors are less than one percent of the parameter values. The parameter correlation matrix is given in Table 2.2.

The χ^2 error criterion is calculated and plotted as a surface over the k_d - k_r plane in Figure 2.6a. This shape is funnel and has a single minimum.

The convergence of the parameters and the evolution of χ^2 and λ are shown in Figure 2.6b.

The data points, the curve fit, and the curve fit confidence band are plotted in Figure 2.6c. Extended-tailing is produced with the reversible deposition model. The numerical results with best-fitted parameter values have good coincidence with the simulated experimental measurements.

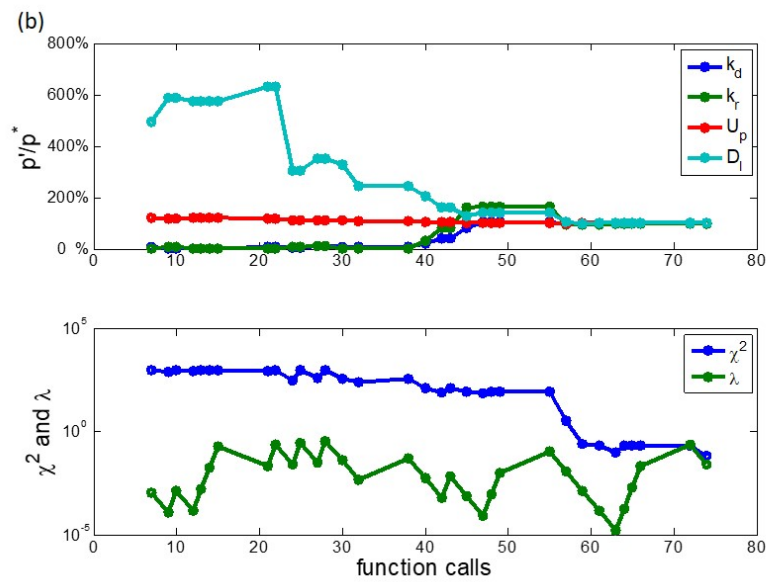
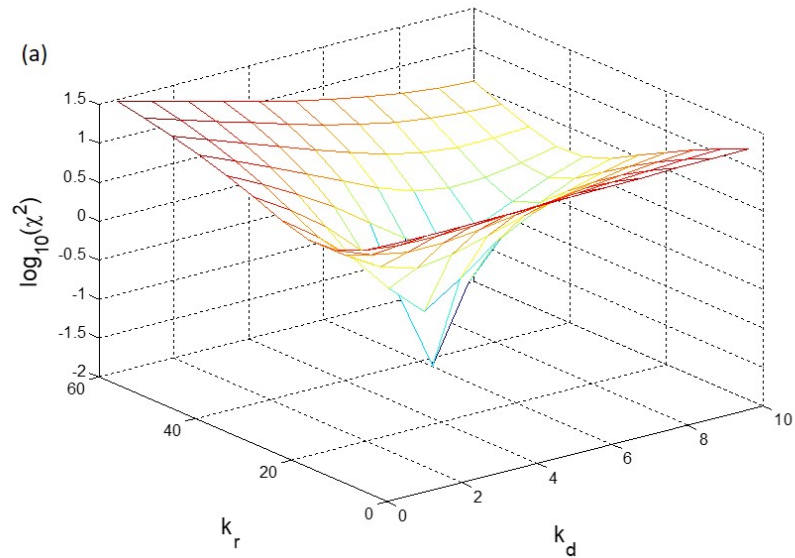
A histogram of the difference between the data values and the curve-fit is shown in Figure 2.6d.

Table 2.1. Parameter values and standard errors.

	$p_{initial}$	p_{true}	p_{fit}	σ_p	$\sigma_p / p_{fit} (\%)$
$p_1 (D_L)$	0.027	0.0135	0.0137	2.9e-4	0.143
$p_2 (k_d)$	2	5	4.8533	0.0104	0.214
$p_3 (k_r)$	5	30	29.1725	0.0657	0.225

Table 2.2. *Parameter correlation matrix*

	p_1	p_2	p_3
p_1	1.00	-0.82	-0.55
p_2	-0.82	1.00	0.85
p_3	-0.55	0.85	1.00



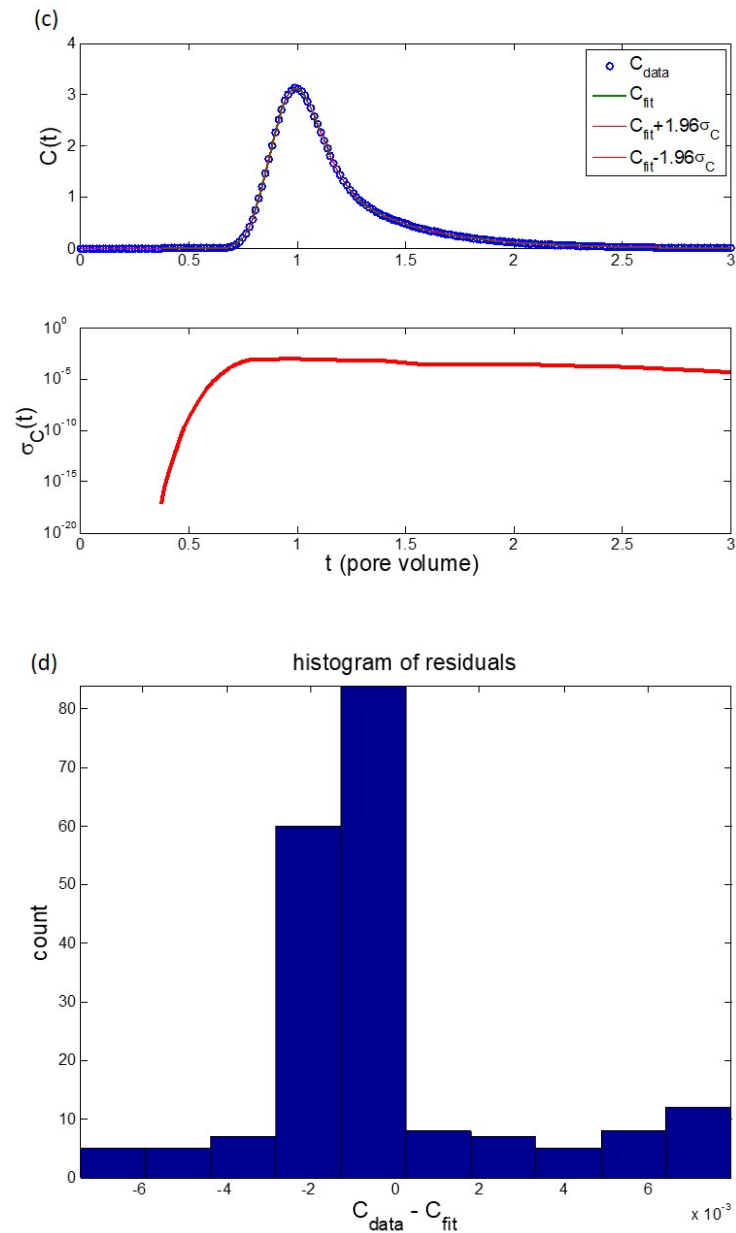


Figure 2.6. (a) The squared errors as a function of kd and kr . (b) Top: the convergence of the parameters with each iteration, (b) Bottom: values of χ^2 and λ each iteration. (c) Top: Measured data C , curve-fit \hat{C} , curve-fit+error, and curve-fit-error; (c) Bottom: standard error of the fit, $\sigma_{\hat{C}}$. (d) Histogram of the errors between the data and the fit.

2.6 Summary

This chapter presents the modeling of particle transport, deposition and reentrainment. First the adopted physical model is presented, it is based on the dispersion convection equation with the consideration of reversible and irreversible deposition. The analytical solution of this equation is then developed. The numerical model developed ~~by the candidate~~ to solve the equation is described. The method of finite differences is used for numerical modeling. In this section, different aspects of numerical model are discussed, including the stages of discretization, the analysis of stability and errors as well as the choice of parameters to limit the digital oscillations. The model optimization for the identification of the parameters is subsequently presented. Finally, a test is performed on experimental data known to verify the validity of the model and the error on the identification of three parameters: dispersion coefficient, kinetic coefficients of deposition and reentrainment.

In next chapter, the developed numerical model will be applied to modelling pulse- and step- input injection experiments [Ahfir et al., 2017; Hammadi et al., 2017]. With experimental and numerical results, the deposition mechanisms under unfavorable conditions will be elucidated as well as effects of different physical factors, such as particle population sizes, grain size distribution, etc.

Chapter 3 Modelling of particle transport, deposition and reentrainment

For more than recent four decades, the colloid filtration theory (CFT) stemming from Yao et al. (1971) has been supplying the basis for a functioning theory to predict particle transport and removal in homogeneous porous media without particle-grain repulsion. However, in aquifers, both particles and porous medium grain typically are found to be negatively charged and the subsurface water generally has a low ionic strength and neutral pH (Bradford et al., 2006a). Under these conditions, the electrical double layer interaction is repulsive, yielding an energy barrier for attachment (so-called unfavorable conditions). Nearly no particle deposition is predicted by existing models derived from CFT in the presence of energy barriers because these models are constructed based on the hypothesis of totally equivalent surface characteristics (e.g. zeta potentials and surface topography) across the whole surfaces. However significant deviations were often found between the predictions with mean-field approaches and experimental results under unfavorable conditions for both biological and nonbiological particles. (Bolster et al., 1999; Bradford et al., 2002; Li et al., 2004; Redman et al., 2001; Tufenkji, 2007; Yang et al., 2015). A variety of explanations for the observed retention in the presence of strong energy barriers have been proposed and corroborated in the literature over the last decade. According to these studies, retention mechanisms can be broadly classified into two types: straining and non-straining. As to non-straining mechanisms, three main mechanisms were considered: retention at physically and chemically heterogeneous bulk surface, wedging at grain-to-grain contacts and retention via secondary energy minimum (see Fig. 3.2) association. Since 2002, straining has been argued to be the main mechanism dominating the particle retention under unfavorable conditions over a threshold particle:collector ratio of only 0.002 to 0.005 (Bradford et al., 2003, 2006a; Xu et al., 2006) rather than 0.154 (Herzig et al., 1970). However, Johnson et al. (2007b, 2010, 2013) argued that the so-called straining with such a small particle:collector ratio might just be the removal of

particles at grain-to-grain contacts, or wedging. Straining and wedging are the mechanisms engendered by pore space geometry, like pore throats and grain-to-grain contacts, which are not considered in the single collector model. As for the retention on bulk surface, nano to micro scale discrete roughness and chemical heterogeneity have been reported to contribute to particle retention, both in the presence of energy barriers (Assemi et al., 2006; Bradford and Torkzaban, 2012, 2013; Bradford et al., 2013; Duffadar et al., 2009; Pazmino et al., 2014a,b; Torkzaban and Bradford, 2016) and in absence of energy barriers (Jin et al. 2015a,b; Jin et al. 2016).

Furthermore, the fluid flow is much weaker near collector surface and grain-to-grain contact, or flow stagnation zones relative to bulk fluid domain. Thence particle transport and removal at separation distance corresponding to secondary energy minimum has been proved to have an important influence in particle retention. The retained particles in secondary energy minimum are very sensible to hydrodynamic and chemical conditions and easy to be released back to the bulk fluid or to translate along the collector surface (Li et al., 2005; Tong and Johnson, 2006; Johnson et al., 2007a; Torkzaban et al., 2015). Such retention is called reversible retention, which would dramatically increase the particle residence times and yield extended tailing observed during the elution phase in the column experiment.

Most previous literature concerns the monodisperse particle, but however natural particles in underground water are often polydisperse or continuously distributed. Blocking and ripening are found to result in time- and concentration-dependent attachment behavior. Under unfavorable conditions, the reduction of attachment resulting from blocking is significant due to very few attachment sites relative to favorable conditions. The tangential flow along a deposited particle may create a shadow zone behind the particle, and blocking effects are therefore significantly enhanced. The hydrodynamic shadow effects were observed to be increased with increasing particle size and fluid velocity, thus resulting in a higher blocking rate (Ko and Elimelech, 2000). For the polydisperse particle, surface retained large particles would enhance the effects of blocking on the attachment of small ones. The ripening was observed to be negligible on the smooth surface in the presence of

energy barriers but increase with the number and length of grain-to-grain contacts (Tong et al., 2008). Wedging and straining of large particles would supply excess number of contacts with collector surface, thus enhancing the ripening of small particles. Some researchers (Ahfir et al., 2016; Bradford et al., 2006b; Yoon et al., 2006) conducted sand-packed column experiments of size continuously distributed particles. To identify the retention mechanisms of particles with continuous size distribution, the particle cumulative size distribution was measured in influent and effluent. Furthermore, to exhibit the characteristics of retained particles more clearly, the particle size distribution of retained particles at different positions was also measured in Ahfir et al. (2016) and Abbar et al. (2017). However, the interplay of different-sized particles retention cannot be elaborated clearly in such experiments. Xu and Saiers (2009) utilized bidisperse particles (3.1 and 5.1 μm) as injected particle and observed that the larger particle could enhance the retention of the smaller particle. The shortcoming of the experiment is that the studied particle sizes are so close that the retention mechanisms might be similar.

To understand particles transport and fate in saturated porous media and the deposition and re-entrainment mechanisms on the effects of different factors, the proposed models were applied to series of laboratory column experiments with pulse-input and step-input injections of particle suspension. Column experiments are classical method utilized to study particle transport in porous media. They can supply indirect observation of the particle behavior.

3.1 Pulse-input injection of Latex colloids

3.1.1 Materials and experimental methods

Under constant flow conditions, injections of a short pulse of particle suspension were performed in a horizontal Plexiglas column (inner diameter of 4 cm and length of 32 cm). The porous medium that filled the column during the experiments consists of quartz sand collected from the Seine River (France), with grain size selection being performed by sieving. The grain size distribution of sand is 630-800 μm with a median diameter of 715 μm and uniformity coefficient of 1.13. The porosity and bulk density are equal to

0.393(\pm 0.005) and 1.58 g/cm^3 , respectively. Experimental set-up is exhibited in Figure 3.1.

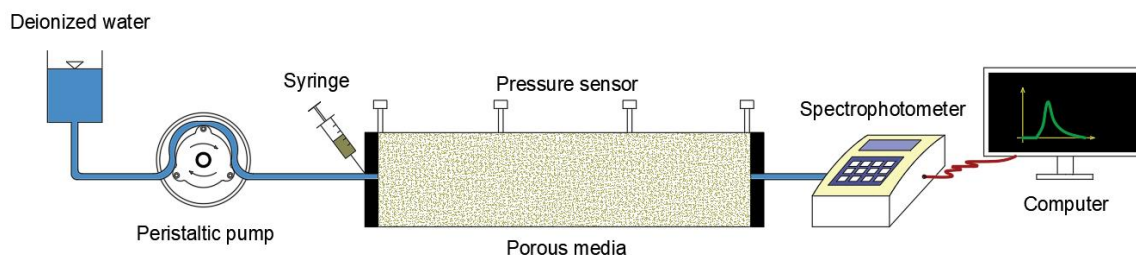


Figure 3.1 Pulse input of latex suspension experimental set-up

Carboxylate-modified polystyrene latex microspheres (Invitrogen ThermoFisher SCIENTIFIC) of three sizes (3, 10 and 16 μm) were used in the experiments. In addition to the monodisperse particles, the tridisperse particle constituted by the three sizes particles was also used as injected particle, designated as MIX (3, 10, 16 μm). The particle density is equal to 1.05 g/cm^3 . The influent particle concentrations (C_0) in monodisperse and tridisperse suspensions are equal to 6 g/l . In addition, the tridisperse suspension is prepared by mixing the three monodisperse suspensions (3+ 10 + 16 μm) in equal volume proportion. The zeta potential of the porous medium grain is -25.3 (\pm 2.6) mV , and the average value of zeta potential particles is -55.0 (\pm 5.6) mV (at pH=6.7). The interaction energy has been calculated, made summation of equations for electrical double-layer, van der Waals interaction and Born repulsion, according to the extended-DLVO theory (Figure 3.2). The heights of the energy barrier are equal to 2040, 6599 and 10332 kT at the distance of around 10 nm between particle and collector surface for 3, 10 and 16 μm , respectively. The depths of the secondary energy minimum are equal to -1.12, -5.32 and -9.20 kT at the distance of around 300 nm (Fig. 3.2).

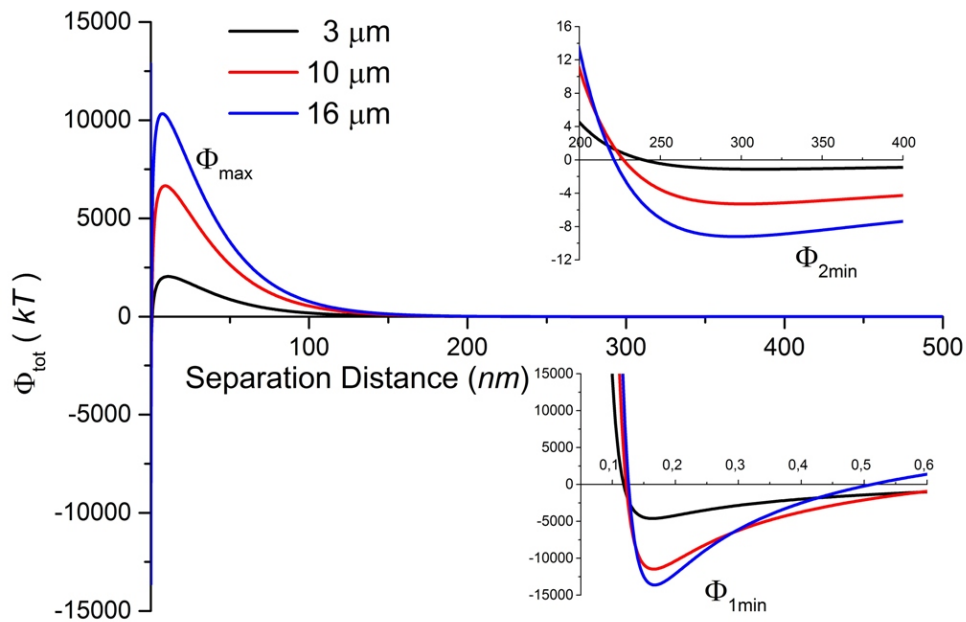


Figure 3.2. Extended-DLVO Interaction energy profiles for all tested particles as functions of the separation distance between the particle and grain: (Φ_{min}) is the interaction energy associated with the primary minimum (Φ_{1min}) or the second minimum (Φ_{2min}), (Φ_{max}) is the interaction energy associated with the energy barrier.

Following 1 ml volume injection of particle suspension, the porous medium was flushed with about 4.5 pore-volume particle-free pure water (pH of 6.7 ± 0.2) with 1 mM NaCl for each experiment. The measured pH of effluent at equilibrium was always around 6.7 in every experiment. Therefore, the experiments were always carried on under unfavorable deposition conditions. Six average pore velocities (from 0.086 to 0.502 cm/s) were tested and are designated as $U1$ (0.0885 ± 0.0025 cm/s), $U2$ (0.179 ± 0.009 cm/s), $U3$ (0.238 cm/s), $U4$ (0.348 cm/s), $U5$ (0.397 cm/s) and $U6$ (0.488 ± 0.025 cm/s).

3.1.2 Mathematical model

The transport of particle through homogeneous porous media is assumed to be mainly affected by several physical processes, namely advection, hydrodynamic dispersion and retention and re-entrainment dynamics. Under unfavorable retention conditions, the model of irreversible, reversible retention and re-entrainment is a simplification of behaviors of the particles genuinely or not genuinely attached in flow stagnation zones.

The one-dimensional continuum-scale model is used to describe particle transport and fate with first-order kinetics considering reversible and irreversible retention sites (Hendry et al., 1997):

$$\frac{\partial C}{\partial t} + \frac{\rho_b}{\phi} \frac{\partial S_{irr}}{\partial t} + \frac{\rho_b}{\phi} \frac{\partial S_r}{\partial t} = D_L \frac{\partial^2 C}{\partial x^2} - u \frac{\partial C}{\partial x} \quad (3.1)$$

$$\frac{\rho_b}{\phi} \frac{\partial S_{irr}}{\partial t} = k_{d,irr} C \quad (3.2)$$

$$\frac{\rho_b}{\phi} \frac{\partial S_r}{\partial t} = k_{d,r} C - k_{r,r} \frac{\rho_b}{\phi} S_r \quad (3.3)$$

where C [M/L³] is the particle concentration in the pore fluid, D_L [L²/T] is the longitudinal hydrodynamic dispersion coefficient, u [L/T] is the average pore fluid velocity, x [L] is the distance from the particle injection point, S_{irr} [L/L] is the “irreversibly” retained particle concentration on the solid phase (particles per unit mass of sand), S_r [L/L] is the “reversibly” retained particle concentration, ρ_b [M/L³] is the bulk density, θ [L³/L³] is the porosity, $k_{d,irr}$ [1/T] is the particle irreversible deposition rate coefficient, $k_{d,r}$ [1/T] is the particle reversible deposition rate coefficient and $k_{r,r}$ [1/T] is the particle re-entrainment rate coefficient.

A one-dimensional finite difference scheme for finite column with a first-type boundary condition at the column inlet and a second-type boundary condition at the outlet was used to approximate the equations (3.1-3.3) in the coupled transport and deposition model. We quantified the kinetics deposition of particle by fitting numerical solutions of equations (3.1-3.3) to the particle BTCs. This code is coupled to a nonlinear least squares optimization routine based upon the Levenberg-Marquadt least squares algorithm to find the best fit values of D_L , $k_{d,irr}$, $k_{d,r}$ and $k_{r,r}$. The numerical codes for simulating the coupled transport-retention-reentrainment and of optimization are developed by the authors. Values of the average pore velocities were calculated from experimental measurements.

3.1.3 Results

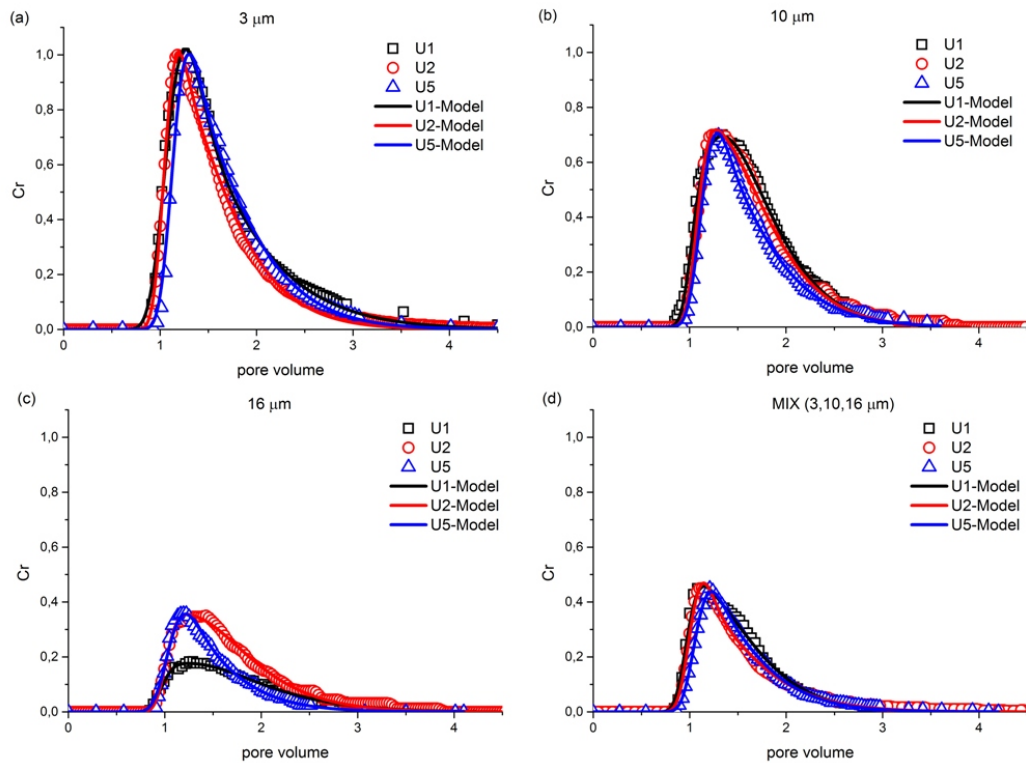
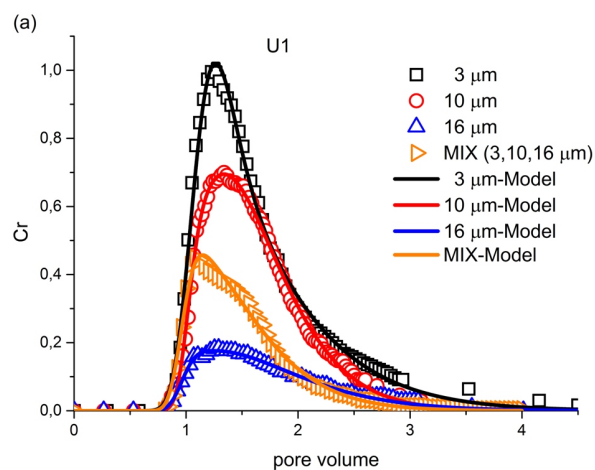


Figure 3.3 BTCs at different fluid velocities of (a) $3 \mu\text{m}$, (b) $10 \mu\text{m}$, (c) $16 \mu\text{m}$, and (d) MIX (3, 10 and 16 μm). C_r is the relative particle concentration in effluent, expressed as $C_r = \frac{C_e \cdot V_p}{m}$. Where, C_e is particle concentration in effluent, V_p is the pore volume equal to the product of the sand column volume and the porous medium porosity, m is the total injected particle mass.



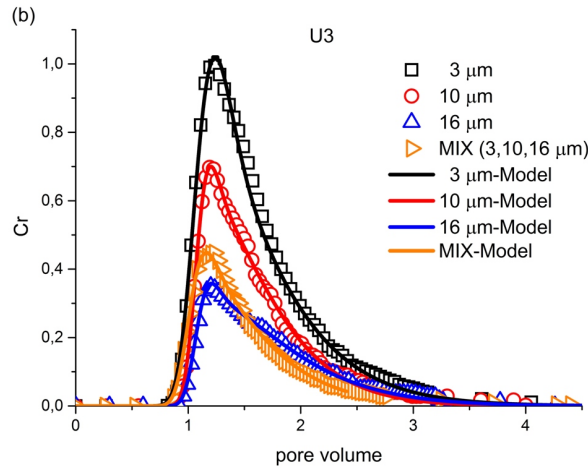


Figure 3.4 BTCs of different-sized and mixed particles at $U=U1$ (a) and $U=U3$ (b).

Figure 3.3 and 3.4 show good descriptions of BTCs with the reversible – irreversible retention model for all particle injection experiments. In the figures the y-axis title, C_r is the relative particle concentration in effluent, expressed as $C_r = \frac{C_e \cdot V_p}{m}$. Where, C_e is particle concentration in effluent, V_p is the pore volume equal to the product of the sand column volume and the porous medium porosity, m is the total injected particle mass. Hence, this model could be used to explain the observed fluid velocity and particle size dependent transport, retention and re-entrainment behavior of microspheres. Extended tailings of BTCs were well reproduced by the simulations with this model, which reflect long residence time of reentrained particle population.

Figure 3.3 indicates that over the entire range of fluid velocities examined, hydrodynamic forces globally have negligible influence on retention except for 16 μm particle. For monodisperse particles, retention increases with the increase in particle size at a given fluid velocity (Fig. 3.4). In addition, the retention of MIX is always between that of 10 and of 16 μm .

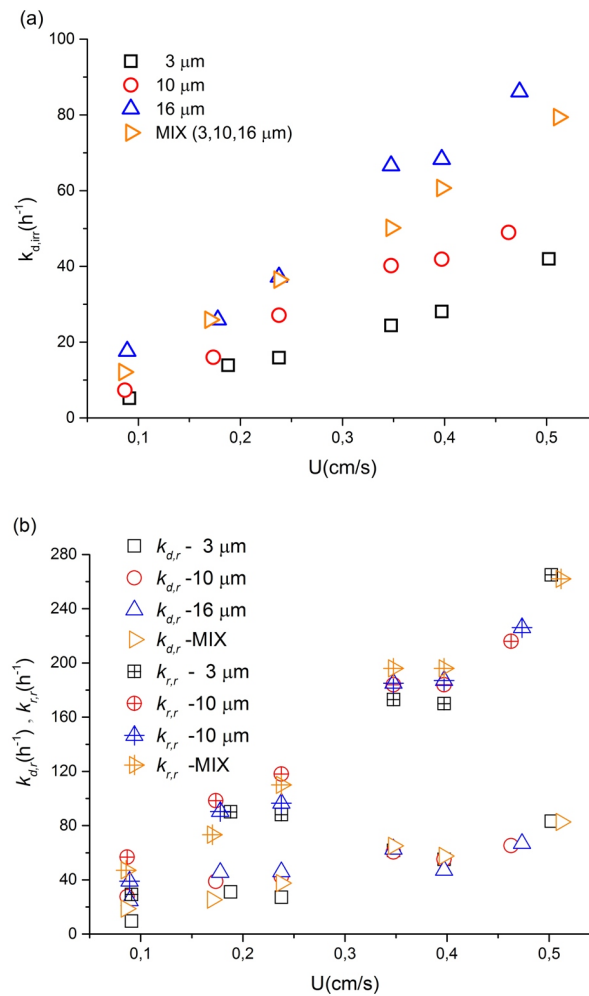


Figure 3.5. A plot of fitted irreversible deposition rate ($k_{d,irr}$) (a) and reversible deposition ($k_{d,r}$) and re-entrainment ($k_{r,r}$) rate values (b) of different-sized and mixed particles as a function of fluid velocity

Table 3.1 Optimal Parameter Values Estimated from BTCs of monodisperse and polydisperse particles. M_E (%) refers to percent recovery of injected microspheres via effluent.

Particle	U (cm/s)	D_L (cm^2/s)	$k_{d,irr}$ (h^{-1})	$k_{d,r}$ (h^{-1})	$k_{r,r}$ (h^{-1})	M_E (%)
3 μm	0.091	0.033	5.19	9.48	29.2	72.7
	0.188	0.029	13.9	31.1	90.1	80.0
	0.238	0.063	15.9	27.1	88.1	75.6
	0.348	0.039	24.4	61.8	173	78.6
	0.397	0.072	28.1	55.1	170	78.8
	0.502	0.051	42	83.2	265	80.1
10 μm	0.087	0.010	7.32	27.6	56.7	56.6
	0.173	0.023	16	38.8	98.5	59.4

	0.238	0.026	27.1	42.3	118	55.9
	0.348	0.040	40.2	60.6	184	51.6
	0.397	0.073	41.9	55.2	184	56.1
	0.463	0.085	49	65.3	216	51.3
16 μm	0.089	0.017	17.6	24.5	39	16.9
	0.178	0.026	25.9	45.4	90.4	30.3
	0.238	0.027	37.2	45.9	96.5	29.4
	0.348	0.040	66.6	62.6	185	28.2
	0.397	0.115	68.3	47.1	187	27.7
	0.473	0.079	86.1	66.8	226	27.4
MIX (3+10+16)	0.086	0.016	12.1	18.7	47.1	36.4
	0.170	0.031	25.9	25.4	73.3	35.1
	0.238	0.044	36.5	37.6	110	32.0
	0.348	0.067	50.2	65.1	196	36.3
	0.397	0.084	60.7	57.6	196	35.8
	0.512	0.076	79.4	82.7	262	37.4

The best-fitted parameter values of $k_{d,irr}$, $k_{d,r}$ and $k_{r,r}$ are exhibited in Figure 3.5 and Table 3.1. $k_{d,irr}$, $k_{d,r}$ and $k_{r,r}$ vary respectively between 5.19 and 86.1 h^{-1} , 9.48 and 83.2 h^{-1} as well as 29.2 and 265 h^{-1} . With increasing fluid velocity, all three parameters generally increase for a given monodisperse or polydisperse particle (Fig. 3.5). At the same flow rate (Q), $k_{d,irr}$ has a similar trend with effluent mass recovery $M_E(\%)$ expressed as $M_E\% = \frac{\int c_e Q dt}{m}$, increasing with increased particle size (Fig. 3.5 and Table 3.1). Moreover, deposition rate coefficients calculated on the basis of CFT and T-E equations (Tufenkji and Elimech, 2004) were found to have similar increasing trends with the $k_{d,irr}$ in this model in the range of fluid velocities and particle sizes examined.

3.1.4 Mechanisms of Retention and Reentrainment in Flow Stagnation Zone

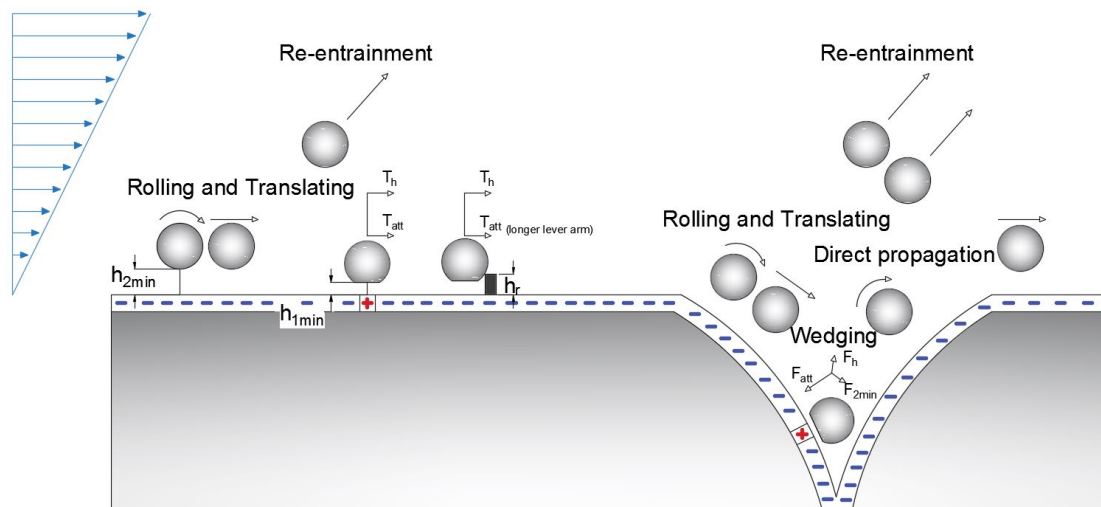


Figure 3.6 Schematic illustration of particle behaviors and torques and forces exerted on the particles in fluid stagnation zones, near-surface and grain-to-grain contact. h_{2min} , h_{1min} and h_r represent separately the distance corresponding to the local secondary energy minimum, the distance corresponding to the local primary energy minimum and the height of roughness; T_h , T_{att} represent hydrodynamic and attachment (primary minimum) adhesive torques; F_h , F_{att} , F_{2min} represent hydrodynamic, attachment (primary minimum) and ‘non-contact’ (secondary minimum) adhesive forces (Modified from Bradford et al., 2013, Darbha et al., 2012, Johnson and Hilpert, 2013)

Generally, retention mechanisms under unfavorable conditions can be divided into two types: straining and non-straining. Straining is usually defined as retention in pore throats too small to pass (McDowell-Boyer et al., 1986; Bradford et al., 2004; Foppen et al., 2005; Tufenkji et al., 2004). As for non-straining retention mechanisms, there are mainly three types: attachment on open surface at physical and chemical heterogeneity, wedging at grain-to-grain contacts, and retention without attachment via secondary energy minimum association in zones of low fluid drag (Ma et al., 2011). Straining and wedging are the mechanisms of removing particles in liquid phase by the aide of typical pore constriction geometry; as to surface heterogeneity and secondary energy minimum interaction, particles are retained reversibly or irreversibly due to relatively larger surface adhesion to the hydrodynamic force and torque in the given local conditions. Straining is used to describe that one or several particles are entrapped in a too small pore throat to pass, which is independent on fluid velocity and energy barriers. Relative to the deterministic nature of straining, wedging has a partly probabilistic nature due

to complex hydrodynamic field and semi-open geometric structure near grain-to-grain contacts (Johnson et al., 2010). Both chemical and physical heterogeneity can reduce or eliminate the energy barrier due to the decreased electrostatic forces and increased Van der Waals attraction (Suresh and Walz, 1996). In addition, surface roughness declines the lever arm for hydrodynamic torque and drastically increases that for resisting adhesive torque (Bradford et al., 2013; Burdick et al., 2005; Li et al., 2005). Hydrodynamics have significant impacts on heterogeneous surface particle removal mechanisms relative to the pore constriction deposition. Figure 3.6 illustrates the particle motion in the flow stagnation zones in the presence of energy barriers. Figure 3.6 illustrates the particle motion in the flow stagnation zones in the presence of energy barriers. Particles within the fluid near the forward stagnation axis probably enter the near-surface domain and then skim (translate and/or roll) across surface via secondary minimum association without attaching. Most skimming particles would exit the stagnation zone back to the bulk fluid during crossing surfaces and the vicinity of grain-to-grain contacts due to diffusion and local hydrodynamic field fluctuation (Bradford et al., 2011; Johnson et al., 2007a), like flow vortices. Some skimming particles would be trapped in flow vortices (Torkzban et al., 2008; Li et al., 2010a,b) or propagate directly to the downward particle surface (Johnson and Hilpert, 2013; Ma et al., 2011).

3.1.5 Effects of Hydrodynamic Forces

Figure 3.3 displays similar BTC profiles at different velocities for a given particle size except for the 16 μm particle at $U1$. All three dynamic parameters ($k_{d,irr}$, $k_{d,r}$ and $k_{r,r}$) increase approximately linearly with increased fluid velocity (Figure 4). No distinct variations in the effluent mass recovery were observed with increased velocities (Table 3.1). This indicates that most of irreversible retained particles via non-straining mechanisms (surface heterogeneity and wedging) are fixed stably (Fig. 3.2) at locations with heterodomains (Ma et al., 2011) in the range of fluid velocities examined at the assemblage scale except for the 16 μm particle at $U1$. Johnson et al. (2010) also found negligible detachment from smooth glass bead surfaces with increase in fluid velocity up to a factor of 64 times or more by direct observation.

In this model, $k_{d,r}$ and $k_{r,r}$ were utilized to make a simplified quantitative description of the dynamics of the reentrained particle population in the flow stagnation zones (near grain surface and grain-to-grain contacts). However, in the absence of perturbations, unlike the process of attachment-detachment of biological particles, for nonbiological particle, rolling and translation dominate the reversible deposition mechanisms along the surface at separation distance corresponding to the secondary energy minimum. The long residence time of the retained particle population in fluid stagnation zones results in the particle retardation and extended tailings of BTCs. The linear increase in $k_{d,r}$ and $k_{r,r}$ with fluid velocity (Fig. 3.5b) therefore indicates that the increased velocity reduces systematically the residence time of the particle population in the flow stagnation zones. Meanwhile similar tailings of BTCs with the increase in fluid velocity are observed.

3.1.6 Effects of Particle Size

In contrast to negligible influence of velocity on retention, Figure 3.4 and Figure 3.5a show respectively greater retention and higher irreversible deposition rate for larger particles. Average retained mass recovery ($(100 - M_E)\%$) of 3, 10 and 16 μm particles are 22.4, 44.85 and 75.35% (Table 1), respectively, increasing exponentially with particle size. A similar trend with particle diameter can be observed for the $k_{d,irr}$ for every fluid velocity. For instance, $k_{d,irr}$ are equal to 5.19, 7.32 and 17.6 h^{-1} for 3, 10 and 16 μm particles at $U1$, respectively. Bradford (2003 and 2006) and Xu (2006 and 2008) also found that straining and wedging rate is power law or linear function of the ratio of particle:collector as the ratio is beyond some threshold value. This indicates that the dominance of straining and wedging in deposition increases with the increased particle size in the presence of energy barriers. Straining is usually defined as one or several particles definitely blocked in a too small pore throat regardless of the fluid velocity and energy barrier repulsion (Herzig et al., 1970; Johnson et al., 2010). The ratio of particle size to pore throat size is almost the only factor determining this removal mechanism. Retention by straining are argued to be important for particles with diameter 10 μm and 16 μm due to the pore throats with the

dimension less than 1.8 times particle diameter (Auset and Keller, 2006). As the smallest average ratio of particle:collector is 0.0042 in this study, beyond the threshold of wedging (0.004) (Johnson et al., 2007b), wedging is one of the main retention mechanisms for all particle size. Moreover, quartz sands composed by angular grains have increased length and number of contacts relative to glass beads, enhancing wedging at the contacts (Tong and Johnson, 2006). The motion of large particles is restricted critically relative to small ones and fluid vortices have less impact on large one. Large particles therefore would be removed from the fluid more efficiently by the grain-to-grain contact. Thence both wedging and straining were found to be enhanced with increased particle size in our study (Figure 3.4 and 3.5) and the previous literature (Bradford and Bettahar, 2006; Chalk et al., 2012; Johnson et al., 2007b; Porubcan and Xu, 2011; Tong and Johnson, 2006; Xu et al., 2006, 2008).

Widespread attachment on the open surface in the presence of energy barriers were observed at multiple focus plans for particles across a wide range of particle sizes from 0.25 to 9 μm in the article of Johnson et al. (2010). Collector surface removal of particles therefore is argued to also play a role in retention in this study. For both the chemical and physical heterogeneity with a given size, the hydrodynamic torques increase more rapidly than adhesive torques with increased particle size according to earlier torque balance calculations (Burdick et al., 2005; Bradford et al., 2013). Correspondingly, the fraction of collector surface area contributing to particle deposition was found to decrease with particle size (Bradford et al., 2013). In this study, excess retention of 16 μm at $U1$, which is not found for 3 and 10 μm , corroborates that fluid velocity has a large impact on retention with large particles (Bradford et al., 2013; Pazmino et al., 2014b). Yet the higher effluent mass recovery except for 16 μm at $U1$ was not observed. It indicates that, within the studied range, the increase in fluid velocity did not result in reducing the fraction of collector surface area contributing to the irreversible retention in the presence of energy barriers at assemblage scale. Hence a certain critical fluid velocity may exist between $U1$ and $U2$ for 16 μm , once beyond which hydrodynamic torques overcome adhesive torques for a large number of particles at column

scale. This inference of critical velocity needs to be tested and verified further with different ranges of tested velocities and particle sizes.

In general, particle size has opposite effects on heterogeneous surface retention and on pore constriction retention in the presence of energy barriers. $k_{d,irr}$ is observed to increase with increasing particle size (Figure 3.5a), indicating that straining and wedging dominates deposition in this study. In contrast to $k_{d,irr}$, $k_{d,r}$ and $k_{r,r}$ do not have any systematic variation with increased particle size (Figure 3.5b).

3.1.7 Interplay of Different-Sized Particles Retention

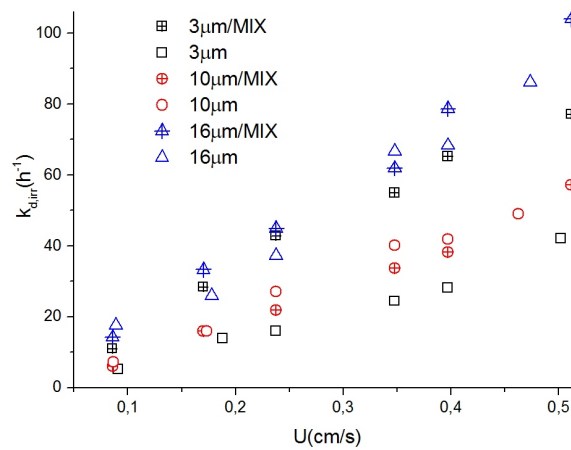


Figure 3.7. Comparison of irreversible deposition rate ($k_{d,irr}$) values of different-sized particles in monodisperse experiments and in polydisperse experiments. 3 $\mu\text{m}/\text{MIX}$ means the 3 μm particle in the tridisperse particle.

Figure 3.5a shows that $k_{d,irr}$ of MIX is between that of 10 and of 16 μm particle and much closer to 16 μm relative to 10 μm . However, as stated previously, the average retained mass recovery is 22.4, 44.85 and 75.35% for 3, 10 or 16 μm in the monodisperse suspension, respectively, and the average recovery of the MIX is 47.5% a little higher than 10 μm . This implies that polydisperse particle size distribution may result in excess retention of one or more size particles. Therefore, to gain insight into the interplay of different-sized particle retention of the tridisperse particles, effluent mass recovery M_E (%), of every size particle was measured (Table 3.1). Depending on this data, $k_{d,irr}$ of each size particle was calculated as follow:

$$k_{d,irr_i} = \frac{1}{3} \frac{(1-M_{E,i})}{(1-M_{E,M})} k_{d,irr_M} \quad (3.4)$$

Subscript $i = 1, 2, 3$ represents separately 3, 10 or 16 μm particle and M means MIX. $k_{d,irr}$ of 10 μm or 16 μm particle in MIX almost has no change comparing that of the monodisperse particle (Figure 3.7). This means that retention of 3 μm did not have any important influence on that of larger particles due to different retention mechanisms elucidated previously. Nevertheless, $k_{d,irr}$ of 3 μm in MIX suspension is significantly enhanced by approximate one time, from 22% to 58% on average relative to the monodisperse suspension of 3 μm (Figure 3.7). Obviously larger particles retention improves the filtration performance of quartz sands for the smaller particles. The injected concentration of every single-sized particle in MIX suspension are only equal to 1/3 of the concentration in the monodisperse suspensions. The retained mass recovery was observed to almost remain constant with decreasing injected concentration when ionic strength is too low or too high, but increase at intermediate ionic strength (Bradford et al., 2009). In this study ionic strength is only 1 mM , and therefore excess retention of 3 μm particle in MIX cannot be ascribed to the effects of injected concentration. In addition, excess retention was not observed for 10 or 16 μm particle indeed in our experiments. Potential origins of this excess deposition of 3 μm particle are examined. On one hand, considerable particles would exit the flow stagnation zone back to the bulk flow in the vicinity of the grain-to-grain contact (Fig. 3.6) according to earlier pore-scale simulations (Johnson and Hilpert, 2013). Thence, relatively little retention of 3 μm , only about 22%, was obtained after the injections of monodisperse particles. Whereas, for the injection of tridisperse particles, the wedged larger particle with the adjacent two collectors form relatively confined space. The shade of the larger particle almost inhibits the flow vortices from mixing with the bulk fluid. Thence the flow velocity should be extremely low and substantial small particles cannot gain enough momentum to escape back to the bulk flow. On the other hand, straining and wedging of larger particles with the adjacent collector can create excess contact sites (wedging) for smaller particles. In general, the retained larger particles due to pore space geometry (straining and wedging) changed the structures of pore throats and grain-to-grain contacts, yielding excess retention of smaller particles (Muresan et al., 2011; Xu and Sainers, 2009).

Figure 3.8 illustrates retention of $3 \mu\text{m}$ particle without or with retained larger particles near the grain-to-grain contact. As stated previously, between the wedged larger particles (10 and $16 \mu\text{m}$) and the grain-to-grain contact, the flow velocities are drastically reduced and extremely low relative to the same zone without retention of larger particles. Considerable small particles are trapped within the fluid in this zone. This situation is analogous to the particle behaviors in the immobile region of fractured porous medium. Moreover, excess wedging sites are also shown in Figure 3.8b

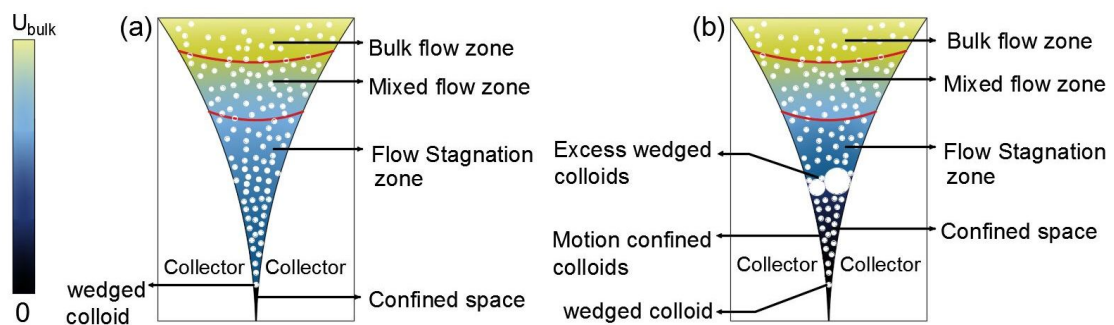


Figure 3.8. Illustrations of $3 \mu\text{m}$ particle behaviors near grain-to-grain contact of (a) without and (b) with retained 10 and $16 \mu\text{m}$ particles. U_{bulk} represents the bulk fluid velocity.

3.1.8 Conclusions

In this section, an irreversible-reversible retention model is applied in order to simulate the transport, retention and re-entrainment of particle (Carboxylate-modified polystyrene latex microspheres) under unfavorable conditions in the sand column. The systematic variations of parameters values of the retention model identify precisely the effects of hydrodynamics and particle size as well as the interplay of different-sized particles retention. Furthermore, the regular trends of parameter values help to bring in-depth insight into the particle transport and retention mechanisms at pore size scale.

Similar profiles of BTCs indicates that the increase in fluid velocity within the studied velocity range does not result in the distinct decrease of the favorable deposition fraction of collector surface area in the presence of energy barriers at assemblage scale. Excess retention for $16 \mu\text{m}$ at $U1$ corroborates that fluid velocity has a large impact on deposition with large

particles. Increased $k_{d,irr}$ with particle size indicates that straining and wedging dominate particle deposition.

Pore constriction structure changes resulting from retention of larger particles are argued to provoke excess retention of the smallest particle. On one hand, wedged larger particles prevent re-entrainment of smaller particles near the grain-to-grain contacts; On the other hand, wedged or strained large particles with the bonding grain surfaces form extra retention sites for smaller particles.

3.2 Step-input injections of kaolinite suspension

3.2.1 Materials and experimental methods

Under constant flow conditions, particle injections were performed in a horizontal Plexiglas column (inner diameter of 4.4 cm and length of 62 cm) using step-input injection technique. The porous medium that filled the column during the experiments consists of quartz sand collected from the Seine River (France), with grain size selected by sieving. Three sands with different grain size distributions were used: Fine sand (315-630 μm), Coarse sand (630-800 μm) and the MIX sand obtained by mixing the Coarse and Fine sands in the equal weight proportion. Coarse, MIX and Fine sands have the median grain diameter (d_g) of 715, 570, and 440 μm respectively and the uniformity coefficient (C_u) of 1.13, 1.80 and 1.37. Using a zetameter (ZetaCAD – CAD Instruments), the measured zeta potentials are -36.44 (± 1.2), -25.31 (± 2.6), or -29.80 (± 1.6) mV for Fine, Coarse and MIX sands, respectively. Experiment set-up is displayed in Figure 3.9.

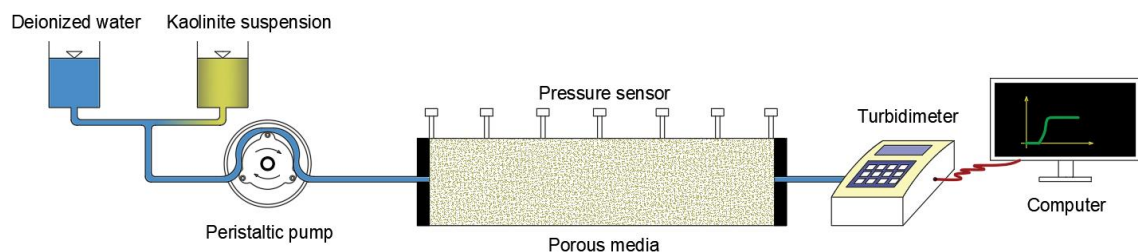


Figure 3.9 Step input of kaolinite particle suspension experimental set-ups.

Size-selected Kaolinite P300 particles with a density of 2.65 g/cm^3 were used as the injected particle in the different porous media tested. The diameter of the injected particle ranged between 2 and 30 μm with the median particle size ($d_{p,50}$) of 10 μm and C_u of 2.5. The zeta potential was measured using a zetameter (ZetaCompact - CAD Instruments) and equal to -35.6 (± 1.4) mV. For polydispersed particles, the span of the size distribution, defined as $S_{pan} = (d_{90}-d_{10})/d_{50}$, is a parameter to show the width of the size distribution (HORIBA INSTRUMENTS, 2016). The interaction energies of the particles with three characteristic diameters of d_{10} , d_{50} and d_{90} , equal to 4.8, 10.2 and 19.4 μm , respectively, are calculated, made summation of equations for

electrical double-layer, van der Waals interaction and Born repulsion, according to the extended-DLVO theory. The heights of the energy barrier are equal to 2674, 5684 and 10808 kT at the distance of around 5 nm between particle and collector surface for d_{10} , d_{50} and d_{90} , respectively. The depths of the secondary energy minimum are equal to -2.28, -5.74 and -11.88 kT at the distance of around 300 nm (Fig. 3.10).

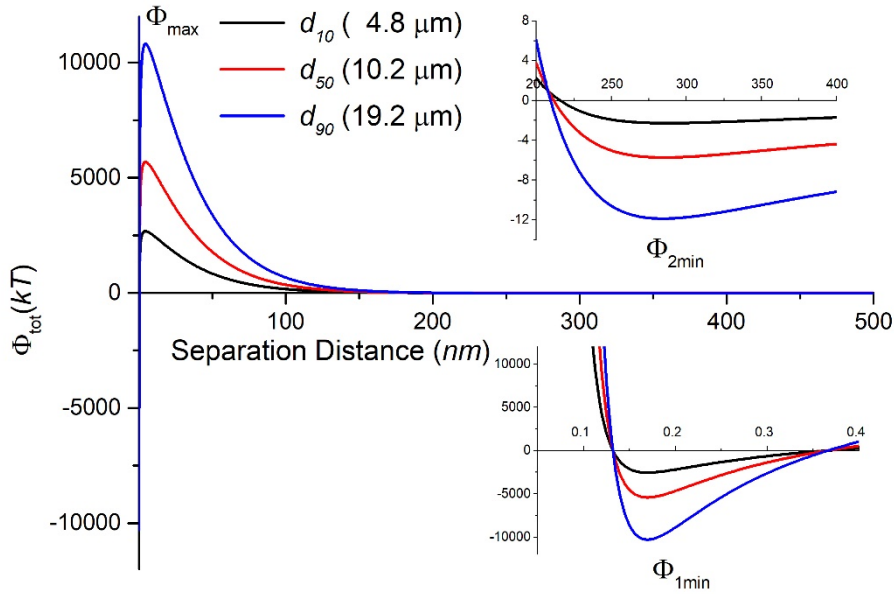


Figure 3.10. Extended-DLVO Interaction energy profiles for kaolinite particles with characteristic diameters of d_{10} , d_{50} and d_{90} as functions of the separation distance between the particle and grain: (Φ_{min}) is the interaction energy associated with the primary minimum (Φ_{1min}) or the second minimum (Φ_{2min}), (Φ_{max}) is the interaction energy associated with the energy barrier.

For each experiment, three pore volumes were injected. The initial influent particle concentration was $C_0 = 0.5$ g/l. Five velocities (0.045, 0.067, 0.089, 0.137 and 0.160 cm/s) were tested for each porous medium and are designated as $U1$, $U2$, $U3$, $U4$ and $U5$, respectively.

Following each column experiment, the dirty sand filling the column was excavated and divided into fifteen different sections with respective thicknesses from the entrance: 5×2 cm, 5×4 cm, 1×6 cm, and 4×6.5 cm.

The mass of the deposited particles in each section was then determined using the following procedure: the dirty sand from each section was dried and weighed and then thoroughly washed. The clean sand was dried and weighed; the difference in weight between the dirty and clean sand represented the accumulated weight of the retained particles. This procedure allows us to determine the spatial distribution of retained particles in the porous media. Finally, a mass balance was conducted using the masses of particles in the effluent, retained in the porous medium, and injected into the column. Table 3.2 presents the calculated particle mass percentages that were recovered in the effluent (M_E), sand (M_S) and the total ($M_T = M_E + M_S$) system.

To understand the evolution of the polydisperse particle population during the transport and deposition process in porous media, particle size distribution (PSD) was measured for particles in the effluent and retained particles using a Coulter Multisizer II particle counter, respectively. For the effluent, samples of 45 ml for PSD analysis were collected at the column outlet. As for retained particles, PSD was measured for the retained particles for every section of the column.

3.2.2 Mathematical Model

The particle transport through homogeneous porous media is assumed to be mainly affected by three physical processes, namely advection, hydrodynamic dispersion and deposition. For the experiments studied in the present paper, both particles and porous media grains being negatively charged, straining and wedging should be considered as the dominant mechanism in the particle deposition process in the presence of an energy barrier. Meanwhile, surface mass removal of particles due to rough or chemically heterogeneous grain surfaces cannot be neglected (Johnson et al., 2010), especially at low flow velocity in the case of kaolinite particles with a specific density of 2.65 g/cm³. Due to the platy morphology (Benosman, 2012) and relatively large density of the used kaolinite P300 particle as well as relatively little particle injection volume (3 pore volume), re-entrainment of retained particles is not considered across the temporal and spatial scales of

column experiments (Johnson et al., 2010). Therefore, pore constriction (wedging and/or straining) and surface deposition can be described by only one deposition parameter.

The one-dimensional advection-diffusion equation with a deposition term is used to describe the transport and retention of particles in a saturated porous medium (Corapcioglu et Jiang, 1993):

$$\frac{\partial C}{\partial t} = D_L \frac{\partial^2 C}{\partial x^2} - u \frac{\partial C}{\partial x} - \frac{\rho_b}{\phi} \frac{\partial S}{\partial t} \quad (3.5)$$

where C [M/L³] is the mass concentration of suspended particles in the pore water, t [T] is time, ϕ [L³/L³] is the porosity, S [M/M] is retained particle concentration, D_L [L²/T] is the hydrodynamic longitudinal dispersion coefficient, u [M/T] is the average pore velocity, and ρ_b [M/L³] is the bulk density. Due to a small injected volume of particle suspension, the most important retention (occurrence at the column inlet of Fine sand at $U1$) was less than 0.2% in volume, therefore negligible influence on porosity and fluid velocity.

Due to large density and plate-shape of kaolinite particle, reentrainment behavior at assemblage scale can be neglected. Correspondingly, extended tailings of BTCs were not observed and the numerical model without reversible retention term was capable of well fitting the experimental measurements in previous literature [Bennacer et al., 2013, 2017]. Therefore, $k_{d,r}$ and $k_{r,r}$ are considered null in this model. The deposition term can therefore be expressed as follows:

$$\frac{\rho_b}{\phi} \frac{\partial S}{\partial t} = k_{d,irr}(x, t)C \quad (3.6)$$

$$k_{d,irr}(x, t) = k_0 \psi(x, t), \quad (3.7)$$

where k_{dep} [1/T] is the deposition rate and k_0 [1/T] is a constant rate coefficient that quantifies deposition kinetics under clean bed conditions; $\psi(x, t)$ is a dimensionless particle deposition function and can be modeled as follows:

$$\psi(x, t) = e^{-S/S_c} \cdot \left(\frac{L_c}{L_c + x} \right) \quad (3.8)$$

where x [L] is the distance from the column inlet and S_c is a characteristic retention with the same units as S [M/M] that quantifies the exponential decline in deposition rates (Xu et al., 2006). In this work, particle transport and deposition occur in the presence of energy barriers in mean-field; thus, deposition at pore constrictions, like grain-to-grain contacts and pore throats, plays an important role. Despite the repulsion between particles, ripening still occurs at pore constrictions (Tong et al., 2008; Xu et al., 2006), which slows down the decrease in deposition rate due to blocking. Hence, we chose the exponential function ($\exp(-S/S_c)$) (Xu et al., 2006) rather than a linear Langmuirian approach ($1 - S/S_{max}$). In addition, in contrast to other nonlinear approaches like polynomial functions, S_c in the exponential function has a similar physical meaning with S_{max} . Both characterize the porous medium filtration capacity. L_c [L] is the characteristic length. The function $L_c/(L_c+x)$ is used to achieve the decrease in the deposition efficiency with the increasing distance (Wang et al., 2014), analogous to the power law function of $\left(\frac{d_g+x}{d_g}\right)^{-\beta}$ proposed by Bradford et al. (2003) in the straining model. This spatial function reflects the effects of straining and the heterogeneity of the particle population. The particle population heterogeneity encompasses the particle size heterogeneity and the particle-surface interaction heterogeneity (Yuan and Shapiro, 2010). The decreasing trend of particle population sizes with distance brings about two main effects on the deposition dynamics. On one hand, in the respect of deposition, the larger particles in the particle population deposit faster and correspond to greater deposition rate. This can be ascribed to i) Straining and wedging highly depend on particle size; ii) the particle flux to flow stagnation zones of large particles is greater than that of small ones, especially for the studied silt particles with great density. Therefore, decreased particle sizes of suspended particle populations with distance contribute to the decreased deposition rates. On the other hand, in the respect of transport, strained particles at upstream produce dead-end pores and limit particle transport pore networks at downstream. Decreased particle sizes reduce the limitation effects of straining on particle transport with increased distance.

According to CFT, the deposition rate coefficient can also be calculated as follows [e.g., Logan et al., 1995]:

$$k_0 = \frac{3(1-\omega_0)}{2} \frac{\alpha \eta u}{d_g} \quad (3.9)$$

where α is the sticking efficiency and η is the single-collector contact efficiency.

For polydispersed particles in this study, the equivalent deposition rate coefficient under favorable conditions is expressed as $k_{0,eq} = \int_{r_{p,min}}^{r_{p,max}} k_0(r_p) f(r_p) dr_p$ with $\alpha=1$, where r_p is the particle radius; $f(r_p)$ is the probability density function of the particle size distribution; $r_{p,max}$ and $r_{p,min}$ are the maximum and minimum of particle size. α under unfavorable conditions is equal to the ratio of the best-fitting k_0 of the experiment results to the calculated $k_{0,eq}$.

A one-dimensional finite difference with the optimal weighting coefficient (Wang and Lacroix, 1997) for a finite column at the outlet was used to approximate the equations [3.5-3.8] in the coupled transport and deposition model. Both the first-type and third-type boundary conditions can be used at the column inlet in the case of same values of (D_L/u) (Van Genuchten, 1980). In this study, a first-type boundary condition was employed at the inlet and a second-type boundary condition was employed at the outlet.

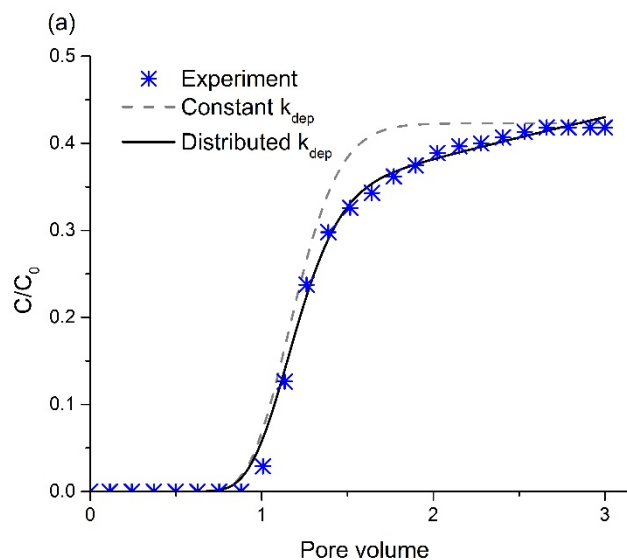
We quantified the kinetics deposition of particles by fitting numerical solutions of equations [3.5-3.8] to the particle breakthrough curves (BTCs) and retention data. This code is coupled to a nonlinear least squares optimization routine based on the Levenberg-Marquadt least squares algorithm to find the best fit values of D_L , k_0 , L_c and S_c . The numerical codes for simulating the coupled transport-deposition and for the optimization are developed by the authors. Values of the average pore velocities were calculated from experimental measurements.

3.2.3 Results

First-order and the time-distance-dependent deposition kinetics

In Figure 3.4, the dotted-line curves present the results of the simulation with constant k_{dep} ; the solid-line curves display the numerical results of the present proposed model. The analytical model is capable of simulating

roughly the effluent concentration data but cannot achieve the slight increase in the BTCs after approximately 1.5 pore volumes (Fig. 3.11a). In many other studies (Bradford et al., 2002, 2006b; Xu et al., 2006; Sun et al., 2015), the steady-state breakthrough plateaus were not observed either, indicating that straining and blocking occurred during the experiments (Bradford et al., 2002). The model with a constant deposition rate is not able to simulate the hyperexponential retention profiles (Fig. 3.11b). For all experiments, regardless of the fluid velocity and the porous medium, deviations of retention profiles are always observed between experimental data and the simulation results of the constant k_{dep} model. In contrast, simulations with the time-distance-dependent deposition rate are capable of fitting the retention profiles well (Fig. 3.11b). In this work, we will focus on understanding the spatiotemporal evolution of the deposition rate based on the experimental results and best-fit parameter values of the proposed model.



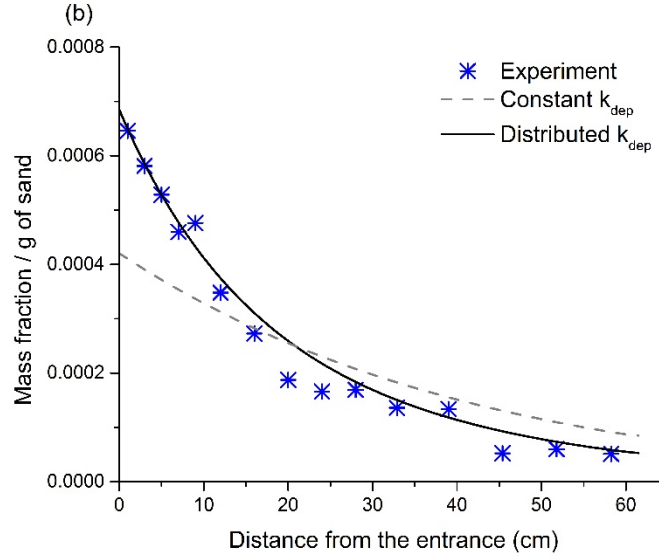


Figure 3.11 Effluent breakthrough curves (a) and retention profiles (b) at the Darcy velocity of $U4$ in the Coarse sand column. Simulations with constant deposition rate (dashed line) are contrasted against those with time-distance-dependent deposition rate (solid line).

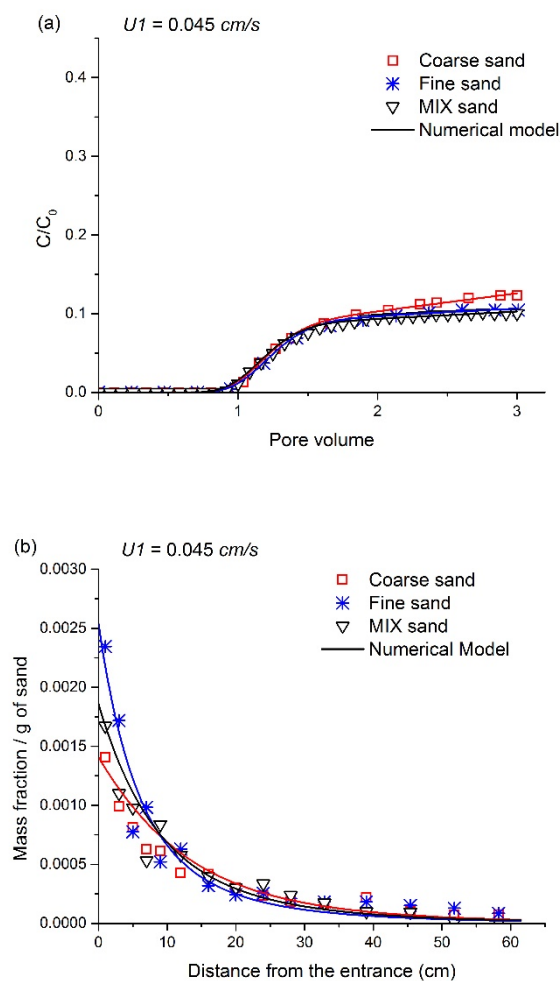
Simulations of the time-distance-dependent deposition

As is displayed in Figure 3.11, the time-distance-dependent deposition was determined to have a good prediction of effluent concentration and retention in the porous medium. Hence, it might be used to explain the observed fluid velocity-dependent transport and deposition behavior in the different porous media. The deposition coefficients were fitted to each experimental BTC and retention profiles exhibited in Figure 2. The agreement between modeled and observed relative concentration (C/C_0) is generally good, and the apparent decrease in retention profiles is clearly reproduced. Table 3.2 summarizes the values of model parameters as well as the results of mass balance. Values of M_T ranged from 98% to 105%, which can be ascribed to measurement errors.

Figure 3.12 displays breakthrough curves and retention profiles of the three studied porous media at $U1$ (Fig. 3.12a,b) and $U4$ (Fig. 3.12c,d). For the same porous medium, higher velocity results in higher effluent mass recovery M_E (Fig. 3.12a,c and Table 3.2), and the retention curve decreases relatively gently at the higher velocity (Fig. 3.12b,d). The M_E of the MIX sand is the highest and that of the Fine sand is higher than that of the Coarse sand at every fluid velocity. However, the Fine sand is observed to have the most

retention near the column entrance and the steepest retention profiles (Fig. 3.12b,d).

The best-fit values of parameters for the different experiments are exhibited in Table 1. k_0 varies between 33 h^{-1} and 83 h^{-1} , L_c ranges from 10 to 22 cm , and S_c is between $30 \cdot 10^{-5}$ and $287 \cdot 10^{-5}$. With the increase in fluid velocity, k_0 increases systemically (Fig. 3.13a), and in contrast, S_c decreases. For different porous media, k_0 increases, but L_c decreases with decreasing median grain diameter.



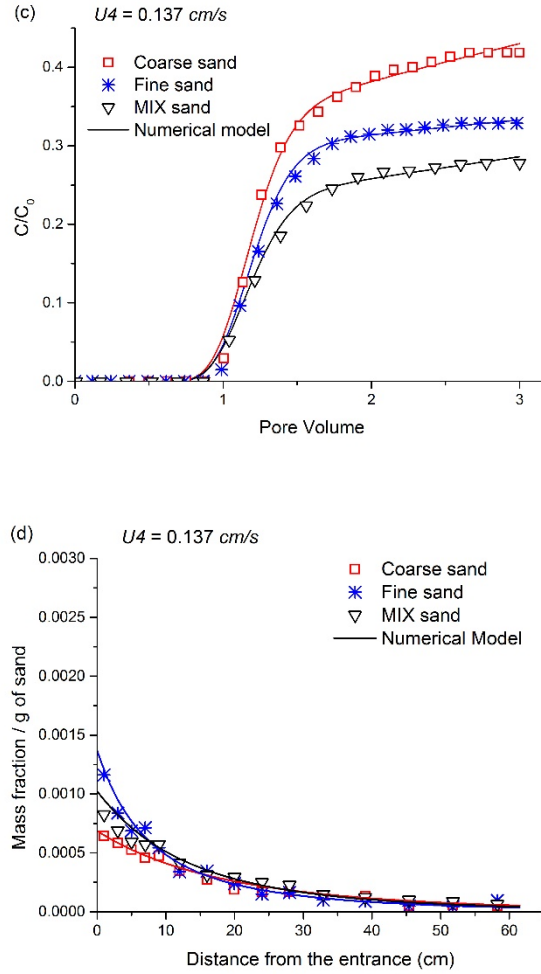


Figure 3.12. Observed and simulated effluent breakthrough curves and retention profiles of the Coarse, Fine and MIX sand at Darcy velocities of U_1 (a,b) and U_4 (c,d).

Table 3.2 Optimal Parameter Values Estimated from BTCs and Retention. r_e^2 , r_s^2 : coefficients of determination for BTC and retained profile, respectively; the Recovered Effluent (M_E), Sand (M_S) and the Total Particle Mass Fraction (M_T)

Sand	U_{Darcy} (cm/s)	D_L (cm ² /s)	L_c (cm)	$S_e 10^{-5}$ (cm ³ /cm ³)	k_0 (hr ⁻¹)	$k_{0,eq}(\alpha=1)$ (hr ⁻¹)	r_e^2	r_s^2	M_E (%)	M_S (%)	M_T (%)
Coarse sand (630-800 μ m)	0.045	0.10	25	102.13	29.7	933.0	1	0.94	12.2	91.0	103.2
	0.067	0.13	25	59.87	39.4	907.2	0.98	0.95	18.0	80.3	98.3
	0.089	0.18	25	57.53	34.3	892.9	0.99	0.98	34.4	70.3	104.7
	0.137	0.28	25	56.27	44.1	879.6	0.99	0.99	41.8	62.2	104.0
	0.160	0.35	25	29.61	46.3	877.9	0.97	0.89	51.8	52.4	104.2
Fine sand (315-630 μ m)	0.045	0.10	10	286.97	49.8	1544.4	1	0.97	10.7	94.1	104.8
	0.067	0.15	10	203.72	64.7	1540.7	0.99	0.94	14.5	86.4	100.9
	0.089	0.21	10	183.81	59.2	1553.5	0.99	0.87	25.0	73.7	98.7
	0.137	0.29	10	178.75	81.5	1605.8	1	0.95	33.0	71.6	104.6

	0.160	0.34	10	146.38	86.0	1636.7	0.99	0.99	37.7	67.0	104.7
MIX sand (315-800 μm)	0.045	0.10	20	252.36	34.5	1378.1	1	0.96	10.2	94.0	104.5
	0.067	0.13	20	104.27	52.5	1359.5	1	0.93	11.8	88.9	100.7
	0.089	0.22	20	67.41	49.7	1356.6	0.99	0.95	21.5	79.6	101.1
	0.137	0.32	20	105.24	65.8	1374.1	0.98	0.99	27.8	74.5	102.3
	0.160	0.41	20	91.66	74.9	1388.5	0.94	0.94	30.2	73.7	103.9

3.2.4 The deposition dynamics parameters

In the presence of energy barriers, η describes quantitatively the dynamics of particles that enter the near-surface domain (Johnson and Hilpert, 2013). Interception (η_I), diffusion (η_D) and sedimentation (η_G) are three main modes according to single-collector theory. η of d_{10} , d_{50} and d_{90} (4.8, 10.2 and 19.4 μm) are calculated to characterize the particle population flux dynamics to the fluid stagnation zone. For all three characteristically sized particles, due to the large particle density (2.65 g/cm^3) relative to fluid, sedimentation is the absolutely dominant mechanism at every fluid velocity according to the calculation from the T-E equations (Tufenkji and Elimelech, 2004). η_G is 10 times η_I and 1000 times η_D , on average, and therefore, interception and diffusion can be neglected. η increases exponentially with particle size, and η_{d90} is roughly 3 times η_{d50} and 10 times η_{d10} (Fig. 3.13b). Moreover, η_{eq} , the equivalent contact efficiency of polydispersed particles, expressed as $\eta_{eq} = \int_{r_{p,min}}^{r_{p,max}} \eta(r_p) f(r_p) dr_p$, is higher than η_{d50} by 25%. This indicates that large particles can much more easily enter the near-surface domain, so size heterogeneity in the particle population plays an important role in deposition for polydispersed particles.

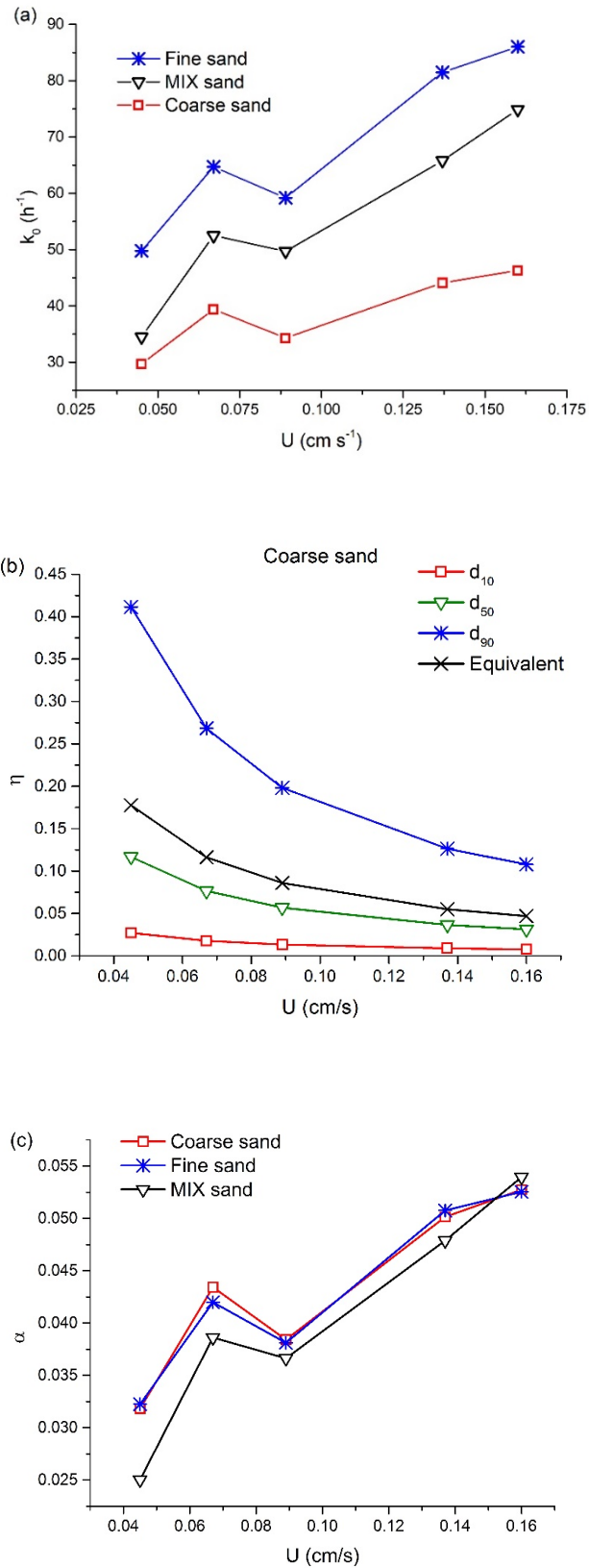


Figure 3.13 Plots of fitted values of a) the initial deposition rate (k_0), b) the single-collector contact efficiency for the Coarse sand, and c) the sticking efficiency of different porous media as a function of fluid velocity.

η of the three characteristic sizes as well as the equivalent efficiency (η_{eq}) decrease exponentially with velocity. Higher velocity decreases the particle flux to the collector surface because stronger hydrodynamic forces counteract the effects of gravity in our situation. The sticking efficiency, α , increases generally with the velocity (Fig. 3.13c) and has similar increased trends to those of k_o (Fig. 3.13a) because k_{dep} under favorable conditions ($\alpha=1$) calculated from Eq.[3.9] has no distinct changes with the increased velocity within the studied range (Table 3.2). α at the grain-to-grain contacts (wedging) was observed to increase with velocity, and in contrast, α in the near-surface domain decreased in the presence of energy barriers according to the previous simulations (Johnson et al., 2007). The total α , the summation of α values of surface deposition and straining and wedging, increases with velocity (Fig. 3c) indicates that the contribution of straining and wedging to the total retention increases progressively with velocity. However, the increased trend of α does not mean that there is an increase in the number of deposition sites with fluid velocity. In fact, the increased α results from the underestimation of η especially at high velocities (Fig. 3.13b) because the single collector model does not take account the pore constriction geometry. Straining is used to describe that one or several particles are entrapped in a pore throat independent of fluid velocity and energy barriers. As for wedging, despite its somewhat probabilistic nature relative to straining (Johnson et al., 2007, 2010), wedging is relatively insensitive to the increased velocity in contrast to heterogeneous surface deposition. The potential origins are i) relative to the near-surface domain, in the grain-to-grain contact region, average fluid velocities were reduced promptly (50%-70%) according to previous pore-scale simulations (Ma et al., 2011); ii) a wedged particle exerts adhesions by two bonding surfaces, which is more stable than the deposited particles with a single surface. The increased fluid velocity therefore has much less influence on wedging and straining efficiency than it does on surface deposition. Hence, α of wedging and straining was observed to increase with velocity. As for deposition at surface heterogeneity, the increased fluid velocity with stronger hydrodynamics can decrease the favorable deposition

fraction of the collector surface area in the presence of energy barriers (Bradford et al., 2013). Hence, α of surface deposition decreases with velocity under unfavorable deposition conditions. α decreases obviously as the fluid velocity increases from $U2$ to $U3$ (Fig. 3.13b). It indicates that the favorable deposition surface fraction declines significantly at assemblage scale with the increase in velocity from $U2$ to $U3$, indicating that with increased hydrodynamic torques, a fairly large number of particles can overcome the adhesive torques (e.g., chemical and physical heterogeneities and the secondary interaction energy minimum well) and exit the near-surface domain back to the bulk fluid. The surface characteristics of the three studied porous media are roughly the same, for instance, the similar measured zeta potential and calculated η ; in contrast, the geometry of pore constrictions (e.g., grain-to-grain contacts and pore throats) is totally different. The decreases in α and k_0 at $U3$ for the three porous media regardless of d_g (Fig. 3.13b) therefore corroborates the theory that these decreases should be the effects of increased fluid velocity on the surface deposition rather than straining and wedging, to an extent.

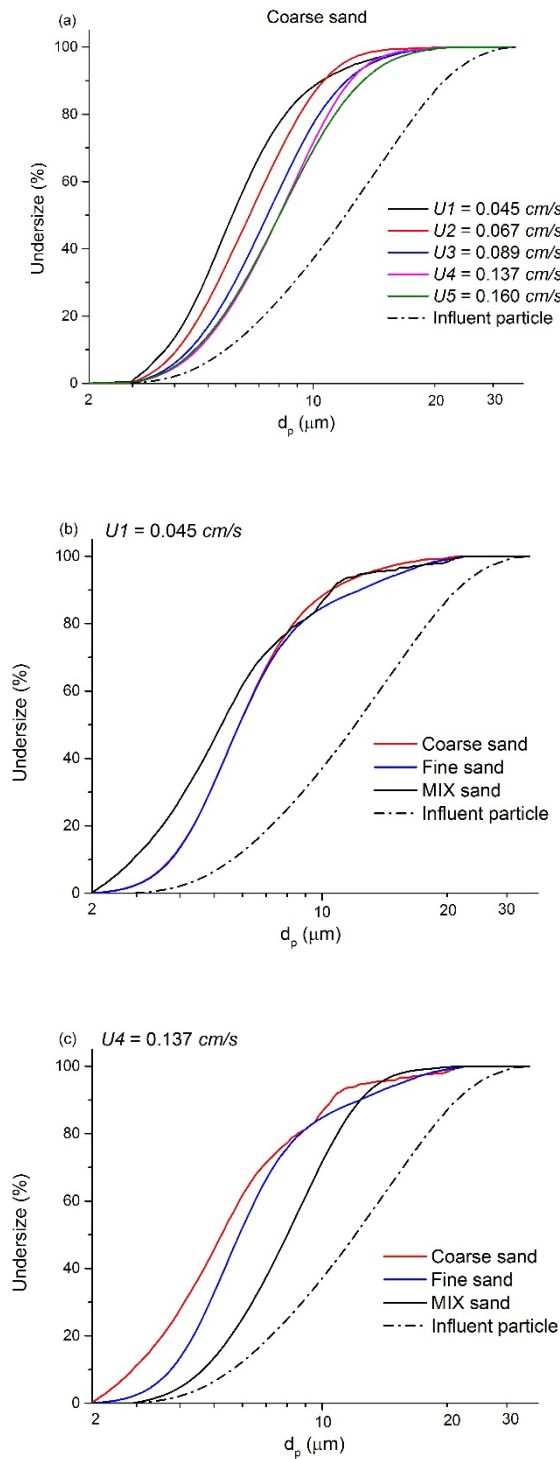


Figure 3.14 PSD of the particles in the effluent at 3 pore volumes: (a) with different Darcy velocities of Coarse sand and in different porous media at (b) $U1$ and (c) $U4$.

Figure 3.14a shows that an increasing proportion of large particles is observed in the effluent with a higher velocity. The contact efficiency of large particles declines much more promptly with the higher velocity relative to that of small particles (Fig. 3.13b). The right shift of the PSD curves with increased

velocity is consistent with the greater decreasing rate of η for large particles according to the calculation of the single-collector model. Figure 3.14b and c display the PSD in the effluent for the three sands at low and high velocity, respectively. The right shift of the PSD curve for the MIX sand column is greater relative to the other two sands at the higher velocity. In fact, due to the different spatial distributions of the deposition rate of different sands, the filtration behavior of the sand column fairly depends on its length. Thus, the PSD in the effluent cannot reflect the effects of the grain size distribution or pore size distribution on particle transport and deposition accurately.

S_c is also found to decrease generally by about 30-70% relative to $U1$ with velocity in the three porous media (Table 3.2), indicating that the increased velocity reduces the number of deposition sites of the porous medium. This can be ascribed to three potential origins. Firstly, funneling of flow into grain-to-grain was observed directly to drive ripening in the presence of energy barriers (Tong et al., 2008; Yoon et al., 2006). Especially for polydispersed particles, large particles retained at pore constrictions (straining and wedging) can supply excess deposition sites for small particles, enhancing ripening (Ma et al., 2017; Xu et al., 2009). Increased fluid velocity would reduce the ripening at grain-to-grain contacts (Tong et al., 2008), thereby decreasing the number of deposition sites. Secondly, the high fluid velocity enlarges the shadow zone formed downstream of the deposited particles (Ko and Elimelech, 2000; Yang et al., 2015), especially for large ones, which also can reduce the particle flux to the surface. Thirdly, as mentioned previously, increased velocity can reduce the favorable deposition surface fraction. L_c remains approximately constant with velocity for every porous medium. On the one hand, straining is affirmed to be independent of fluid velocity. On the other hand, although the higher fluid velocity facilitates the large particles' advancement deeper in the column (Alem et al., 2013), it also decreases the deposition probability for the same particle size due to stronger hydrodynamics.

In the presence of energy barriers, at a given fluid velocity, wedging and straining were observed directly or indirectly to be enhanced with the increased ratio of $d_{p,50}/d_g$ beyond the threshold value (0.002-0.008) in

previous numerical simulations and experiments, and in contrast, deposition on the collector surface either stayed roughly invariant or even decreased (Bradford et al., 2003; Bradford and Bettahar, 2006; Johnson et al., 2007; Xu et al., 2006). Correspondingly in this study, k_0 increases with the ratio of $d_{p,50}/d_g$, also indicating that wedging and straining dominate the retention in the studied situations. In addition, S_c , which is analogous to the maximal deposition capacity, displays a similar trend with the increasing ratio of $d_{p,50}/d_g$ (Table 3.2) because wedging and straining are enhanced with the increasing number and length of the grain-grain contacts (Tong et al., 2008). Approximate calculated values of η for the three porous media result from the slight effects of the sand grain curvature with a very low ratio of $d_{p,50}/d_g$. That there is no remarkable difference in α between the three studied porous media (Fig. 3.13c) indicates that the number of favorable deposition sites is proportional to $1/d_g$ (Eq. 3.9).

3.2.5 Temporal and spatial evolution of the deposition rate

Like many previous studies of deep filtration, the apparent decreased distributions of deposition rates are also illustrated in this article. To discuss the origin of the spatial decrease in the deposition rate, some possible reasons have been proposed, such as straining, the decrease in particle population sizes in the flow as well as the removal of large particles and those near the pore perimeter at the inlet of the column. It can be affirmed that wedging and straining take an important place collectively with a ratio d_p/d_g over 0.014 in this study, far beyond the threshold value of 0.003 to 0.008 (Bradford et al., 2003; Johnson et al., 2007; Xu et al., 2006). Regarding the effects of straining, the transport of particles is restricted in only larger pore networks after the first few centimeters. In addition, the particle size distribution in the effluent is much smaller than that of the injected particles. This indicates that the sizes of the mobile particle population in the fluid decline with increasing transport distance, which enhances the retention near the particle injection source by two mechanisms. On the one hand, large particles are easily removed from particle suspension relative to the small particles. On the other hand, wedged and strained large particles can supply

excess retention sites for the small particles. Furthermore, Li et al. (2004) proposed that removal of particles from the pore water adjacent to pore walls is an additional possible mechanism resulting in this decrease in deposition rate. For the experiments simulated in this work, the flow direction is perpendicular to gravity. Therefore, it can be inferred that large particles can more easily enter the near grain surface domains due to the effect of gravity (Li et al., 2015) and then are retained by surface heterogeneities and grain-to-grain contacts.

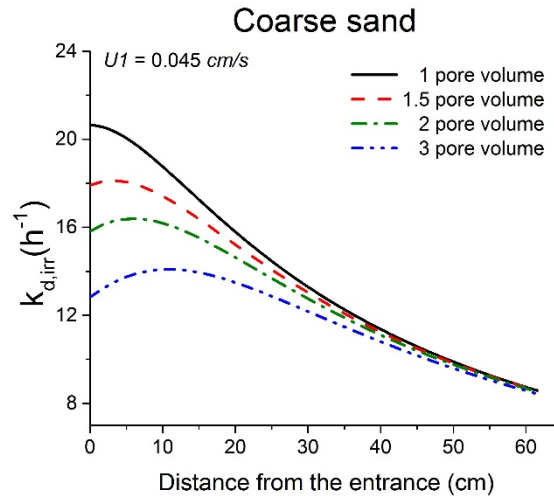


Figure 3.15 Evolution of the deposition rate with time in the Coarse sand column at the Darcy velocity of $U1$.

The temporal evolution of the deposition rate during the injection process at $U1$ in the Coarse sand column is shown in Figure 3.15. The k_{dep} decreases promptly with the increased injection volume near the entrance. The decrease rate declines obviously with increased distance. It can be observed that the maximum value moved forward from the entrance with the increased volume of injected particle suspension. At the beginning of the injection, the highest k_{dep} near the injection source results from the high concentration of large particles and the effects of straining. With the increased injected particle volume, a large number of deposited particles near the injected point bring about a remarkable decrease in the number of deposition sites (blocking), rapidly reducing the deposition rate. Regarding the effects of blocking near the entrance, the large particle concentration of the mobile particle population therefore increases gradually with time away, which slows down the decrease in k_{dep} with increased retention in the downstream.

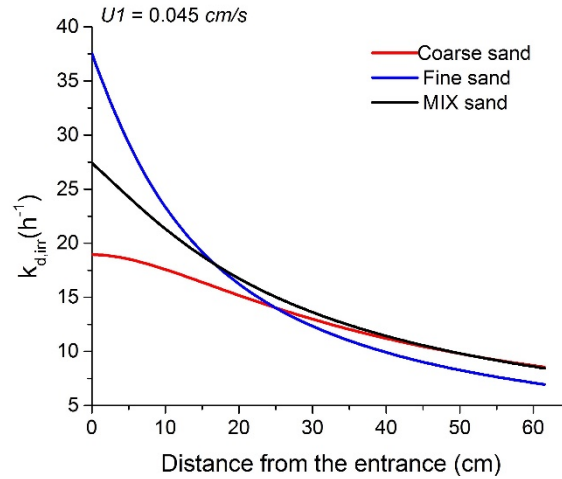


Figure 3.16 The spatial distribution of the temporal average deposition rate coefficient of the three porous media at $U1$, which can be expressed from the numerical results data as: $\bar{k}_{dep}|_{x=x} = \frac{1}{T} \int k_{dep}(x, t) dt$.

To gain insights into the spatial evolution of the deposition rate for the polydispersed particles, the retention characteristics with distance for the three studied porous media with different sand grain size distributions should be analyzed carefully. Figure 3.15 displays the temporally averaged deposition rates (\bar{k}_{dep}) of the three porous media at $U1$, which is expressed as:

$$\bar{k}_{dep}|_{x=x} = \frac{1}{T} \int k_{dep}(x, t) dt.$$

The retention distributions with particle size for the Coarse, Fine and MIX sands are exhibited for the three parts of the column, 0-10 cm (Fig. 3.17a), 10-30 cm (Fig. 3.17b) and 30-62 cm (Fig. 3.17c), respectively. As mentioned above, the sand was excavated and divided into 15 sections to obtain the retained mass and PSD at different positions. We summarized the retained mass and PSD of every five sections (1-5 (0-10 cm), 6-10 (10-30 cm) and 11-15 (30-61.5 cm)). Then, the retention size distribution is the product of the PSD of retained particles and the mass of retention for the three parts of the column. L_c increases with the increased d_g and is equal to 10, 20 and 25 cm for the Fine, MIX and Coarse sand, respectively. Correspondingly, the decrease rate \bar{k}_{dep} for the Fine sand is greater than the MIX and Coarse sand. In the first ten centimeters, the \bar{k}_{dep} ranking from high to low is the Fine, the MIX and the Coarse sand (Fig. 3.16), which is consistent with the decreasing trend of k_0 with d_g (Fig. 3.13a). In Figure 6a, it is clearly observed that the Fine sand has the highest filtration efficiency over the range of all particle sizes due to the large number of small pore throats

and grain-to-grain contacts. However, \bar{k}_{dep} of the Fine sand decreases promptly with the increasing distance from the injection source. Although a large number of small pore throats result in the excellent filtration performance of the Fine sand, straining near the entrance creates many more dead-end pores, making the particle transport restricted to the more limited large-pore networks relative to the Coarse and MIX sands. Limited transport pore networks are the reason why small pores in the Fine sand make very limited contributions to the particle filtration in the second part of the column (Fig. 3.16b). Meanwhile, the Fine sand near the entrance removes the most particles with large sizes, and the concentration of large particles within the mobile particle populations therefore declines promptly with the increased distance and then enhances the decrease in the deposition rate. Correspondingly, the decrease in \bar{k}_{dep} and retention of the Fine sand is therefore more remarkable than the Coarse and MIX sand (Fig. 3.12b,d and Fig. 3.16). As for the MIX sand, on the one hand, the Fine sand constituent evidently improves the particle removal performance on large particles ($d_p > d_{p,50} = 10 \mu m$) relative to the Coarse sand; on the other hand, by virtue of the Coarse constituent, more conductive transport pore networks are conserved in the first ten centimeters (Fig. 3.17a) relative to the Fine sand, and then a greater number of large particles can advance deeper in the column. Meanwhile the Fine sand constituent of the MIX supplies sufficient small pore throats and grain-to-grain contacts to remove the excess large particles in the middle part of the sand column (Fig. 3.17b). As a result, the MIX sand has good filtration performance after the first ten centimeters (Fig. 3.16). Correspondingly, the value of L_c for the MIX sand (20 cm) is much higher than that of the Fine sand (10 cm) and more similar to that of the Coarse sand (25 cm) (Table 3.2). As for the Coarse sand, although the mobile particle population in the column middle part has the most large particles relative to the Fine and MIX sand, higher filtration efficiency has not been observed because there are fewer small pores and grain-to-grain contacts. The three porous media have similar retention distributions with particle size regardless of d_g for 30-62 cm of the column (Fig. 3.17c), indicating that heterogeneous surface deposition may be the main deposition mechanism at

positions relatively far away from the particle source (Bradford et al., 2002). In general, the spatial distribution of the deposition rate is determined by the interplay of the particle size distribution of particle populations and the geometrical change of the porous medium (straining and blocking).

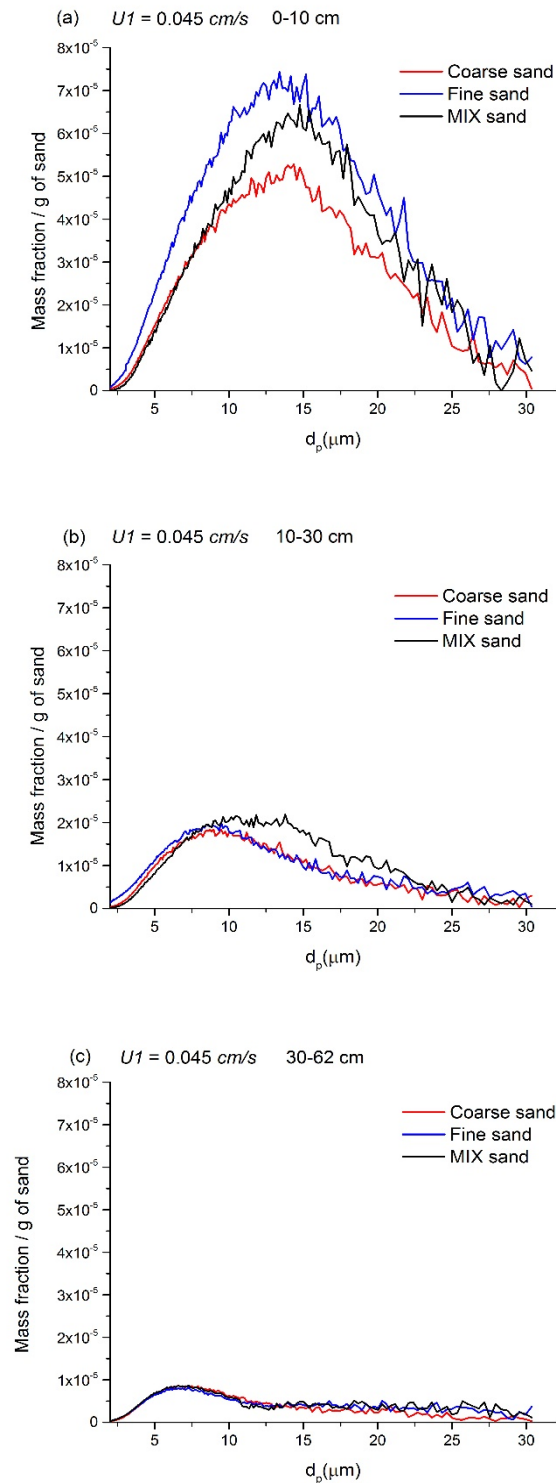


Figure 3.17 Retention distribution with particle size of the three parts of the sand columns: 0-10 cm (a), 10-30 cm (b) and 30-62 cm (c).

3.2.6 Conclusions

In this section, a time-distance-dependent deposition model is applied to simulating the transport and deposition of polydispersed particles under unfavorable conditions in the sand column. Straining and the heterogeneity of the particle population are considered to determine the decreasing distribution of deposition rates. The systematic variations in the values of three parameters that govern this model identify precisely the effects of fluid velocity and the evolution of deposition rate with time and distance:

1. Continuous decrease of BTC plateau concentration implies that surface retained particles play an important role in retention in this work, especially at low velocities. The total α increases with velocity indicates that the contribution of straining and wedging to the total retention increases progressively with velocity. Great retention even at the highest velocity ($U5 = 0.160 \text{ cm/s}$) implies that straining and wedging play an important role in deposition mechanisms at all velocities. S_c decreases with the velocity due to the reduced ripening at grain-to-grain contacts and the enhanced hydrodynamic shadow effects. S_c decreased with increased d_g , reflecting the higher filtration efficiency of the finer porous medium due to the larger number of small pores and grain-to-grain contacts.

2. The temporal and spatial evolutions of k_{dep} in the three porous media with different grain size distributions exhibit the effects of varied particle population sizes as well as straining and blocking on the polydispersed particle deposition. The spatial function with L_c reflects these effects. The interplay of the variation of the size distribution of mobile particle populations and the geometrical change in porous medium due to retention determines the deposition kinetics of polydispersed particles.

Conclusions and perspectives

Conclusions

The objective of this work is to develop a numerical model for modeling of transport and fate of mono- and poly-disperse particles in saturated porous media. Identification of hydrodynamic and deposition kinetic parameters is realized by inverse method. Analysis of experiment data, i.e. particle breakthrough curves and retention profiles, and with best-fitted parameters help to bring insights into the particle's behavior with fluid flow in porous media.

A review of literature concerning the particle transport and deposition in porous media is presented above all. The current basic knowledge of subsurface groundwater, water flow and particle transport and deposition processes in porous media is presented in this chapter. Deposition mechanisms under unfavorable conditions are carefully discussed. Then, Chapter 2 discusses the proposed transport-deposition-reentrainment model and the numerical solution and the used inverse method for identification of parameters.

The modified models based on the general model have been applied to series of pulse-input and step-input injection column experiments in Chapter 3.

In pulse-input experiments, an artificial monodisperse particle (Carboxylate-modified polystyrene latex microspheres) is employed as tested particles, which has relatively homogeneous surface property. In addition, due to narrow size distribution, latex particle is often employed to prepare monodisperse suspension. Since the injection volume is only 1 ml, the modifications of porous media due to retained particles is negligible. Therefore, in this simulation, deposition and reentrainment parameters are considered to be constant. The systematic variations of parameters values of the deposition model identify precisely the effects of hydrodynamics and particle size as well as the interplay of different-sized particles retention.

Similar profiles of BTCs indicates that the increase in fluid velocity within the studied velocity range does not result in the distinct decrease of the favorable deposition fraction of collector surface area in the presence of energy barriers at assemblage scale. Excess retention for $16 \mu m$ at $U1$ corroborates that fluid velocity has a large impact on deposition with large particles. Increased $k_{d,irr}$ with particle size indicates that straining and wedging dominate particle deposition. Pore constriction structure changes resulting from retention of larger particles are argued to provoke excess retention of the smallest particle. On one hand, wedged larger particles prevent re-entrainment of smaller particles near the grain-to-grain contacts; On the other hand, wedged or strained large particles with the bonding grain surfaces form extra retention sites for smaller particles.

In step-input experiments, a natural silt particle (kaolinite P300) was employed as tested particles, which has relatively stable structure (low shrinkage/swelling) and widely used in the study of particle transport in aquifers. Due to great density of kaolinite particle relative to water, reentrainment behavior is not obvious. Therefore, reversible deposition is not taken in account in this simulation. The CFT predictions with constant k_{dep} have important deviations in retention profiles from experimental results. Large injected volume of particle suspension relative to pulse-input experiments results in important variations of porous medium filtration capacity, then bringing about distributed deposition rates. A time-distance-dependent deposition model without reversible deposition is developed to simulate the step-input injection column experiments. The systematic variations in the values of three parameters that govern this model identify precisely the effects of fluid velocity and the evolution of deposition rate with time and distance.

Continuous decrease of BTC plateau concentration implies that surface retained particles play an important role in retention in this work, especially at low velocities. The total α increases with velocity indicates that the contribution of straining and wedging to the total retention increases progressively with velocity. Great retention even at the highest velocity ($U5 = 0.160 \text{ cm/s}$) implies that straining and wedging play an important role in

deposition mechanisms at all velocities. S_c decreases with the velocity due to the reduced ripening at grain-to-grain contacts and the enhanced hydrodynamic shadow effects. ω_c decreased with increased d_g , reflecting the higher filtration efficiency of the finer porous medium due to the larger number of small pores and grain-to-grain contacts.

Global retention in the MIX sand is always the greatest in the three used sands at every tested fluid velocity. The Fine sand captures the most important retention at the inlet of the column and the amount of retention decrease promptly with the increasing distance from the entrance relative to the other two sands. Excess retained large particles ($d_p > 10 \mu m$) in the middle part of the MIX sand column indicates that the MIX sand reserves more conductive pore networks relative to the Fine sand and meanwhile has more small pore throats and grain-to-grain contacts relative to the Coarse sand. The distributions of k_{dep} have the similar profiles with retention profiles. The temporal and spatial evolutions of k_{dep} in the three porous media with different grain size distributions exhibit the effects of varied particle population sizes as well as straining and blocking on the polydispersed particle deposition. The spatial function with L_c reflects these effects. The interplay of the variation of the size distribution of mobile particle populations and the geometrical change in porous medium due to retention determines the deposition kinetics of polydispersed particles.

Perspectives

To further understand the particle transport behavior in porous media and deposition mechanisms, other research at pore scale and assemblage scale is needed to explore in the future. The sand column experiment is an indirect observation method, to verify our conclusions of this work, direct observation methods, such as impinging jet system with a high-speed camera (Johnson et al., 2010) and X-ray computed microtomography [Lindquist et al., 1996; Bhattad et al., 2011], should be employed in our research. The two methods can supply pore scale particle transport and deposition information, i.e. whether to exist deposition and reentrainment on grain surface. With

impinging jet system with a high-speed camera, we can directly observe particle transport and dynamics process and effects of different factors, such as increasing fluid velocities. Correspondingly, pore scale simulation, such the hemispheres-in-cell model using the grid surface integration (GIS) [Ma et al., 2011], is needed to realize to explore interaction forces and torques between particle and grain surface in the near-surface domain. X-ray computed microtomography can supply morphological characteristics of porous media, such as pore throat size and length, pore body diameter and so on. With these characteristics, porous media can be reconstructed based on different models, such as pore network models. Pore network models have been applied widely in non-Newtonian transport of particle and solute, which can bring insights to understanding of straining and size exclusion mechanisms [Shapiro et al., 2010; Yuan et al., 2010, 2011]. In addition, the study of co-transport of silt particle and dissolved contaminants, i.e. heavy metals and organic contaminants, can be considered for the future work.

References

Abbar, B., Alem, A., Pantet, A., Marcotte, S., Ahfir, N.-D., & Duriatti, D., 2017. Experimental investigation on removal of suspended particles from water using flax fibre geotextiles. *Environmental Technology*, 3330(January), 1–15. <http://doi.org/10.1080/09593330.2017.1284270>

Adamczyk Z, Siwek B, Zembala M, Belouschek P. Kinetics of localized adsorption of colloid particles. *Advances in Colloid and Interface Science*. 1994

Ahfir, N.D., Hammadi, A., Alem, A., Wang, H., Le Bras, G., Ouahbi, T., 2016. Porous media grain size distribution and hydrodynamic forces effects on transport and deposition of suspended particles. *J. Environ. Sci.* DOI 10.1016/j.jes.2016.01.032

Albarran N, Missana T, Alonso U, García-Gutiérrez M, López T. Analysis of latex, gold and smectite colloid transport and retention in artificial fractures in crystalline rock. *Colloids and Surfaces A: Physicochemical and Engineering Aspects*. 2013;435:115-26.

Alem, A., Elkawafi, A., Ahfir N.D., Wang, H., 2013. Filtration of kaolinite particles in a saturated porous medium: hydrodynamic effects. *Hydrogeology J.*, 21, 573–586.

Anderson, M. P., 1979, Using models to simulate the movement of contaminants through ground water flow systems, *Crit. Rev. Environ. Control.*, 9(2), 97-156.

Assemi, S., Nalaskowski, J., & Johnson, W. P., 2006. Direct force measurements between carboxylate-modified latex microspheres and glass using atomic force microscopy. *Colloids Surf. A Physicochem. Eng. Aspects*, 286(1–3), 70–77.

Auset, M., & Keller, A. A., 2006. Pore-scale visualization of colloid straining and filtration in saturated porous media using micromodels. *Water Resour. Res.*, 42(12), 1–9.

Bai, C., and Y. Li (2012), Modeling the transport and retention of nC60 nanoparticles in the subsurface under different release scenarios, *J. Contam. Hydrol.*, 136–137(0), 43–55.

Baptista, A. E. de M., 1987, Solution of Advection-dominated Transport by Eulerian-Lagrangian Methods using the backward method of characteristics, Ph. D. dissertation, MIT, Cambridge. MA.

Bauer, M., Blodau, C., 2009. Arsenic distribution in the dissolved, colloidal and particulate size fraction of experimental solutions rich in dissolved organic matter and ferric iron. *Geochim. Cosmochim. Ac* 73, 529e542.

Bendersky, M., and J. M. Davis (2011), DLVO interaction of colloidal particles with topographically and chemically heterogeneous surfaces, *J. Colloid Interface Sci.*, 353(1), 87–97.

Benosman, G. (2012). Migration de particules fines dans un milieu poreux : Application au phénomène de colmatage, (Doctoral thesis). Retrieved from <https://tel.archives-ouvertes.fr/tel-00997415/document>

S. BHATTACHARJEE and M. ELIMELECH : Surface element integration : A novel technique for evaluation of dlvo interaction between a particle and a flat plate. *Journal of Colloid and Interface Science*, 193(2):273–85, 1997.

Bolster, C.H., Mills, A. L., Hornberger, G., Herman, J., 1999. Spatial distribution of deposited bacteria following miscible displacement experiments in intact cores. *Water Resour. Res.*, 35, 1797-1807.

W.R. Bowen, T.A. Doneva and J.A.G. Stoton: The use of atomic force microscopy to quantify membrane surface electrical properties. *Colloids and Surfaces A: Physicochemical and Engineering Aspects*, 201(1):73–83, 2002.

Bradford, S.A., Yates, S.R., Bettahar, M., Simunek, J., 2002. Physical factors affecting the transport and fate of colloids in saturated porous media. *Water Resour. Res.*, 38(12), 63(1–12).

Bradford, S. A., Simunek, J., Bettahar, M., Van Genuchten, M. T., Yates, S. R., 2003. Modeling Colloid Attachment Straining and Exclusion in Saturated Porous Media. *Environ. Sci. Technol.*, 37(10), 2242-2250.

Bradford, S. A., Bettahar, M., Simunek, J., Van Genuchten, M. T., 2004. Straining and attachment of colloids in physically heterogeneous porous media. *Vadose Zone J.*, 3(2), 384–394.

Bradford, S.A., Simunek, J., Bettahar, M., Van Genuchten, M.T., Yates, S.R., 2006a. Significance of straining in colloid deposition: Evidence and implications. *Water Resour. Res.*, 42(12), 15(1–16).

Bradford, S.A., Tadassa, Y.F., Pachepsky, Y., 2006b. Transport of giardia and manure suspensions in saturated porous media. *J. Environ. Qual.*, 35(3), 749–57.

Bradford, S. A., Bettahar, M., 2006. Concentration dependent transport of colloids in saturated porous media. *J. Contam. Hydrol.*, 82(1–2), 99–117.

Bradford, S. A., Torkzaban, S., & Walker, S. L. (2007). Coupling of physical and chemical mechanisms of colloid straining in saturated porous media. *Water Research*, 41(13), 3012–3024.

Bradford, S.A., Kim, H.N., Haznedaroglu, B.Z., Torkzaban, S., Walker, S. L., 2009. Coupled factors influencing concentration-dependent colloid transport and retention in saturated porous media. *Environ. Sci. Technol.*, 43(18), 6996–7002.

Bradford, S. A., Torkzaban, S., Simunek, J., 2011. Modeling colloid transport and retention in saturated porous media under unfavorable attachment conditions. *Water Resour. Res.*, 47(10), 1–12.

Bradford, S.A., Torkzaban, S., 2012. Colloid adhesive parameters for chemically heterogeneous porous media. *Langmuir*, 28(38), 13643–13651.

Bradford, S. A., Torkzaban, S., 2013. Colloid interaction energies for physically and chemically heterogeneous porous media. *Langmuir*, 29(11), 3668–3676.

Bradford, S.A., Torkzaban, S., Shapiro, A., 2013. A theoretical analysis of colloid attachment and straining in chemically heterogeneous porous media. *Langmuir*, 29(23), 6944–6952.

Bradford, S. A., Torkzaban, S., 2015. Determining parameters and mechanisms of colloid retention and release in porous media. *Langmuir*, 31(44), 12096–12105.

Burdick, G.M., Berman, N.S., Beaudoin, S.P., 2005. Hydrodynamic particle removal from surfaces. *Thin Solid Films* 2005, 488, 116–123.

Camesano, T. A., and B. E. Logan (1998), Influence of fluid velocity and cell concentration on the transport of motile and non-motile bacteria in porous media, *Environ. Sci. Technol.*, 32, 1699–1708.

Canseco V., Djehiche A., Bertin H., Omari A. (2009). Deposition and re-entrainment of model colloids in saturated consolidated porous media: Experimental study. *Colloids and Surfaces A: Physicochem. Eng. Aspects*. 352, 5-11.

P.C. Carman, *Flow of gases through porous media*, Butterworths, London, 1956.

Chalk, P., Gooding, N., Hutten, S., You, Z., Bedrikovetsky, P., 2012. Pore size distribution from challenge coreflood testing by colloidal flow. *Chemical Engineering Research and Design*, 90(1), 63–77.

Chrysikopoulos CV, Katzourakis VE. Colloid particle size-dependent dispersivity. *Water Resources Research*. 2015.

Corapcioglu, M.Y., Jiang, S., 1993. Colloid-facilitated groundwater contaminant transport. *Water Resour. Res.* 29, 703, 2215–2226.

Cullen, E., D. M. O'Carroll, E. K. Yanful, and B. Sleep (2010), Simulation of the subsurface mobility of carbon nanoparticles at the field scale, *Adv. Water Resour.*, 33(4), 361–371.

Dale A, Casman EA, Lowry GV, Lead JR, Viparelli E, Baalousha MA. Modeling nanomaterial environmental fate in aquatic systems. *Environmental Science & Technology*. 2015.

Darbha, G. K., Fischer, C., Michler, A., Luetzenkirchen, J., Schäfer, T., Heberling, F., Schild, D., 2012. Deposition of latex colloids at rough mineral surfaces: An analogue study using nanopatterned surfaces. *Langmuir*, 28(16), 6606–6617.

de Jonge, L. W., C. Kjaergaard, and P. Moldrup (2004), Colloids and colloid-facilitated transport of contaminants in soils, *Vadose Zone J.*, 3(2), 321–325.

DeBorde, D. C., W. W. Woessner, Q. T. Kiley, and P. Ball (1999), Rapid transport of viruses in a floodplain aquifer, *Water Res.*, 33(10), 2229–2238.

Delachambre Y. (1966). Contribution à l'étude de l'écoulement d'une suspension à travers un milieu poreux et du mécanisme de filtration. Thèse – Faculté des Sciences de Nancy, France.

Denaix, L., Semlali, R.M., Douay, F., 2001. Dissolved and colloidal transport of Cd, Pb, and Zn in a silt loam soil affected by atmospheric industrial deposition. *Environ. Pollut.* 114, 29e38.

Derjaguin, B., and L. Landau (1941), Theory of the stability of strongly charged lyophobic sols and the adhesion of strongly charged particles in solutions of electrolytes, *Acta Physicochim. USSR*, 14, 633–662.

Drummond, J. D., Davies-Colley, R. J., Stott, R., Sukias, J. P., Nagels, J. W., Sharp, A., & Packman, A. I. (2015). Microbial Transport, Retention, and Inactivation in Streams: A Combined Experimental and Stochastic Modeling Approach. *Environmental Science and Technology*, 49(13), 7825–7833.

Duffadar, R., Kalasin, S., Davis, J.M., Santore, M.M., 2009. The impact of nanoscale chemical features on micron-scale adhesion: Crossover from heterogeneity-dominated to mean-field behavior. *J. Colloid Interface Sci.*, 337(2), 396–407.

M. Elimelech and C.R. O'melia: Kinetics of deposition of colloidal particles in porous media. *Environmental Science and Technology*, 24(10):1528–1536, 1990.

Elimelech, M., M. Nagai, C.-H. Ko, and J. N. Ryan (2000), Relative insignificance of mineral grain zeta potential to colloid transport in geochemically heterogeneous porous media, *Environ. Sci. Technol.*, 34(11), 2143–2148

Foppen, J.W.A., Mporokoso, A., Schijven, J. F., 2005. Determining straining of *Escherichia coli* from breakthrough curves. *J. Contam. Hydrol.*, 76(3–4), 191–210.

Foppen, J. W., van Herwerden, M., & Schijven, J. (2007). Measuring and modelling straining of *Escherichia coli* in saturated porous media. *J. Contam. Hydrol.*, 93(1-4), 236–254.

Flury, M.; Qiu, H. Modeling colloid-facilitated contaminant transport in the vadose zone. *Vadose Zone J.* 2008, 7, 682–697.

Gannon, J. T., V. B. Manilal, and M. Alexander (1991), Relationship between cell surface properties and transport of bacteria through soil, *Appl. Environ. Microbiol.*, 57, 190–193.

Grolimund D, Elimelech M, Borkovec M, Barmettler K, Kretzschmar R, Sticher H. Transport of in Situ Mobilized Colloidal Particles in Packed Soil Columns. *Environmental Science & Technology*. 1998;32:3562-9.

Gross, M., S. E. Cramton, F. Gotz, and A. Peschel (2001), Key role of Teichoic acid net charge in *Staphylococcus aureus* colonization of artificial surfaces, *Infect. Immun.*, 69, 3423–3426.

Hammadi, A. Transport and dépôt de particules en suspension dans un milieu poreux saturé: Effets du milieu et de la polydispersivité des particules. Ph.D Dissertation, Université Normandie, 2016.

Hammes, J., Gallego-Urrea, J.A., Hasselov, M., 2013. Geographically distributed classification of surface water chemical parameters influencing fate and behavior of nanoparticles and colloid facilitated contaminant transport. *Water Res.* 47, 5350e5361.

Han, P., Zhou, D., Tong, M., & Kim, H. (2016). Effect of bacteria on the transport and deposition of multi-walled carbon nanotubes in saturated porous media. *Environmental Pollution*, 213, 895–903.

Harter, T., S. Wagner, and E. R. Atwill (2000), Colloid transport and filtration of *Cryptosporidium parvum* in sandy soils and aquifer sediments, *Environ. Sci. Technol.*, 34(1), 62–70.

Hendry, M. J., Lawrence, J. R., Maloszewski, P., 1997. The role of sorption in the transport of *Klebsiella oxytoca* through saturated silica sand, *Ground Water*, 35, 574–584.

Herald, P. J., and E. A. Zottola (1989), Effect of various agents upon the attachment of *Pseudomonas fragi* to stainless steel, *J. Food Sci.*, 54, 461–464.

Herzig, J.P., D.M. Leclerc, P. Legoff, 1970. Flow of suspensions through porous media—Application to deep filtration. *Ind. Eng. Chem.*, 62, 8–35.

Honeyman, B.D., 1999. Geochemistry e colloidal culprits in contamination. *Nature* 397, 23e24.

HORIBA INSTRUMENTS (2016). A guidebook to particle size analysis. https://www.horiba.com/fileadmin/uploads/Scientific/eMag/PSA/Guidebook/pdf/PSA_Guidebook.pdf

Ikni, T., Benamar, A., Kadri, M., Ahfir, N.-D., Wang, H. (2013). Particle transport within water-saturated porous media: Effect of pore size on retention kinetics and size selection. *C R Geoscience*, 345: 392-400.

Jewett, D. G., T. A. Hilbert, B. E. Logan, R. G. Arnold, and R. C. Bales (1995), Bacterial transport in two porous media systems: Influence of ionic strength and pH on collision efficiency, *Water. Res.*, 29, 1673–1680.

Jiang, X., M. Tong, R. Lu, and H. Kim (2012), Transport and deposition of ZnO nanoparticles in saturated porous media, *Colloids Surf. A*, 401(0), 29–37.

Jin, C., Normani, S.D., Emelko, M. B., 2015a). Surface roughness impacts on granular media filtration at favorable deposition conditions: Experiments and modeling. *Environ. Sci. Technol.*, 49(13), 7879–7888.

Jin, C., Ren, C.L., Glawdel, T., Emelko, M.B., 2015b. Non-linear, non-monotonic effect of nano-scale roughness on particle deposition in absence of an energy barrier: Experiments and modeling. *Scientific Reports* 5:17747.

Jin, C., Ren, C.L., Emelko, M.B., 2016. Concurrent modeling of hydrodynamics and interaction forces improves particle deposition predictions. *Environ. Sci. Technol.*, 50(8). DOI: 10.1021/acs.est.6b00218

Johnson, R. L., J. T. Nurmi, G. S. O'Brien Johnson, D. Fan, R. L. O'Brien Johnson, Z. Shi, A. J. Salter-Blanc, P. G. Tratnyek, and G. V. Lowry (2013), Field-scale transport and transformation of carboxymethylcellulose-stabilized nano zero-valent iron, *Environ. Sci. Technol.*, 47(3), 1573–1580.

Johnson, W. P., Tong, M., 2006. Observed and simulated fluid drag effects on colloid deposition in the presence of an energy barrier in an impinging jet system. *Environ. Sci. Technol.*, 40(16), 5015–5021.

Johnson, W.P., Li, X., Assemi, S., 2007a. Deposition and re-entrainment dynamics of microbes and non-biological colloids during non-perturbed transport in porous media in the presence of an energy barrier to deposition. *Adv. Water Resour.*, 30(6–7), 1432–1454.

Johnson, W. P., Li, X., & Yal, G. (2007b). Colloid retention in porous media: Mechanistic confirmation of wedging and retention in zones of flow stagnation. *Environ. Sci. Technol.*, 41(4), 1279–1287.

Johnson, W. P., Pazmino, E., & Ma, H. (2010). Direct observations of colloid retention in granular media in the presence of energy barriers, and implications for inferred mechanisms from indirect observations. *Water Research*, 44(4), 1158–1169.

Johnson, W.P., Hilpert, M., 2013. Upscaling colloid transport and retention under unfavorable conditions: Linking mass transfer to pore and grain topology. *Water Resour. Res.*, 49(9), 5328–5341.

Keller AA, Sirivithayapakorn S, Chrysikopoulos CV. Early breakthrough of colloids and bacteriophage MS2 in a water-saturated sand column. *Water Resources Research*. 2004;40.

Keller AA, Auset M. A review of visualization techniques of biocolloid transport processes at the pore scale under saturated and unsaturated conditions. *Advances in Water Resources*. 2007;30:1392-407.

Keller AA, McFerran S, Lazareva A, Suh S. Global life cycle releases of engineered nanomaterials. *Journal of Nanoparticle Research*. 2013;15:1-17.

Keller AA, Lazareva A. Predicted releases of engineered nanomaterials: from global to regional to local. *Environmental Science & Technology Letters*. 2013;1:65-70.

Kersting, A. B., D. W. Efurud, D. L. Finnegan, D. J. Rokop, D. K. Smith, and J. L. Thompson (1999), Migration of plutonium in groundwater at the Nevada Test Site, *Nature*, 397,56-59.

Kinzelbach, W., 1986, *Groundwater Modeling, An introduction with sample programs in BASIC*, Elsevier, Amsterdam, Netherlands, 333p.

Ko, C. H., & Elimelech, M., 2000. The “shadow effect” in colloid transport and deposition dynamics in granular porous media: Measurements and mechanisms. *Environ. Sci. Technol.*, 34(17), 3681–3689.

Kocur, C. M., D. M. O’Carroll, and B. E. Sleep (2013), Impact of nZVI stability on mobility in porousmedia, *J. Contam. Hydrol.*, 145(0), 17–25.

Kocur, C. M., et al. (2014), Characterization of nZVI mobility in a field scale test, *Environ. Sci. Technol.*, 48(5), 2862–2869.

Kretzschmar, R., Schafer, T., 2005. Metal retention and transport on colloidal particles in the environment. *Elements* 1, 205e210.

Lamy, E., Lassabatere, L., Bechet, B., Andrieu, H., 2013. Effect of a nonwoven geotextile on solute and colloid transport in porous media under both saturated and unsaturated conditions. *Geotextiles and Geomembranes*, 36, 55–65.

K. Levenberg. A Method for the Solution of Certain Non-Linear Problems in Least Squares. *The Quarterly of Applied Mathematics*, 2: 164-168 (1944).

Li, J., Xie, X., & Ghoshal, S. (2015). Correlation Equation for Predicting the Single-Collector Contact Efficiency of Colloids in a Horizontal Flow. *Langmuir*, 31(26), 7210–7219.

Li, X., Scheibe, T.D., Johnson, W.P., 2004. Apparent decreases in colloid deposition rate coefficients with distance of transport under unfavorable deposition conditions: A general phenomenon. *Environ. Sci. Technol.*, 38(21), 5616–5625.

Li, X., Zhang, P., Lin, C.L., Johnson, W.P., 2005. Role of hydrodynamic drag on microsphere deposition and re-entrainment in porous media under unfavorable conditions. *Environ. Sci. Technol.*, 39(11), 4012–4020.

Li, X. Q., and W. P. Johnson (2005), Nonmonotonic variations in deposition rate coefficients of microspheres in porous media under unfavorable deposition conditions, *Environ. Sci. Technol.*, 39(6), 1658–1665.

Li, X., Lin, C. L., Miller, J. D., & Johnson, W. P. (2006). Role of grain-to-grain contacts on profiles of retained colloids in porous media in the presence of an energy barrier to deposition. *Environ. Sci. Technol.*, 40(12), 3769–3774.

Li, X., Li, Z., Zhang, D., 2010a. Role of low flow and backward flow zones on colloid transport in pore structures derived from real porous media. *Environ. Sci. Technol.*, 44(13), 4936–4942.

Li, X., Li, Z., Zhang, D., 2010b. Tracking colloid transport in porous media using discrete flow fields and sensitivity of simulated colloid deposition to space discretization. *Environ. Sci. Technol.*, 44(4), 1274–1280.

Li, Z., Zhang, D., & Li, X. (2012). Tracking colloid transport in real pore structures: Comparisons with correlation equations and experimental observations. *Water Resources Research*, 48(5), 1–11.

Liang, Y., S. A. Bradford, J. Simunek, H. Vereecken, and E. Klumpp (2013), Sensitivity of the transport and retention of stabilized silver nanoparticles to physicochemical factors, *Water Res.*, 47(7), 2572–2582.

Lin, S. H., Y. W. Cheng, Y. Bobcombe, K. L. Jones, J. Liu, and M. R. Wiesner (2011), Deposition of silver nanoparticles in geochemically heterogeneous porous media: Predicting affinity from surface composition analysis, *Environ. Sci. Technol.*, 45(12), 5209–5215.

Liu HH, Cohen Y. Multimedia environmental distribution of engineered nanomaterials. *Environmental science & Technology*. 2014;48:3281-92.

Liu, X. Y., D. M. O'Carroll, E. J. Petersen, Q. G. Huang, and C. L. Anderson (2009), Mobility of multiwalled carbon nanotubes in porous media, *Environ. Sci. Technol.*, 43(21), 8153–8158.

Liu, Y., Janjaroen, D., Kuhlenschmidt, M. S., Kuhlenschmidt, T. B., & Nguyen, T. H. (2009). Deposition of cryptosporidium parvum oocysts on natural organic matter surfaces: Microscopic evidence for secondary minimum deposition in a radial stagnation point flow cell. *Langmuir*, 25(3), 1594–1605.

Logan, B. E., D. G. Jewett, R. G. Arnold, E. J. Bouwer, and C. R. O'Melia, Clarification of clean-bed filtration models, *J. Environ. Eng.*, 121, 869– 873, 1995.

Ma, E., Ouahbi, T., Wang, H., Ahfir, N., Alem, A., Hammadi, A. (2017). Modeling of Retention and Re-Entrainment of Mono- and Poly-disperse Particles: Effects of Hydrodynamics, Particle Size and Interplay of Different-Sized Particles Retention. *Science of the Total Environment* 596-597C (2017) pp. 222-229. <http://doi.org/10.1016/j.scitotenv.2017.03.254>

Ma, H., Pazmino, E., Johnson, W.P., 2011. Surface heterogeneity on hemispheres-in-cell model yields all experimentally-observed non-straining colloid retention mechanisms in porous media in the presence of energy barriers. *Langmuir*, 27(24), 14982–14994.

Ma, J., Guo, H., Lei, M., Wan, X., Zhang, H., Feng, X., ... Han, X. (2016). Blocking effect of colloids on arsenate adsorption during co-transport through saturated sand columns. *Environmental Pollution*, 213, 638–647.

D.W. Marquardt. An algorithm for least-squares estimation of nonlinear parameters *Journal of the Society for Industrial and Applied Mathematics*, 11(2):431-441, 1963.

Martin, R. E., L. M. Hanna, and E. J. Bouwer (1991), Determination of bacterial collision efficiencies in a rotating disk system, *Environ. Sci. Technol.*, 25, 2075–2082.

Mattison, N. T., D. M. O'Carroll, R. Kerry Rowe, and E. J. Petersen (2011), Impact of porous media grain size on the transport of multi-walled carbon nanotubes, *Environ. Sci. Technol.*, 45(22), 9765–9775.

May, R., and Y. S. Li (2013), The effects of particle size on the deposition of fluorescent nanoparticles in porous media: Direct observation using laser scanning cytometry, *Colloid Surf. A*, 418, 84–91.

May, R., S. Akbariyeh, and Y. Li (2012), Pore-scale investigation of nanoparticle transport in saturated porous media using laser scanning cytometry, *Environ. Sci. Technol.*, 46(18), 9980–9986

Mcdowell-boyer, L.M., Hunt, J.R., Itar, N., 1986. Particle transport through porous media. *Water Resour. Res.*, 22(13), 1901–1921.

Meesters JAJ, Koelmans AA, Quik JTK, Hendriks AJ, Van de Meent D. Multimedia modeling of engineered nanoparticles with SimpleBox4nano: model definition and evaluation. *Environmental science & Technology*. 2014;48:5726-36.

Mesticou, Z., Kacem, M., & Dubujet, P. (2016). Coupling Effects of Flow Velocity and Ionic Strength on the Clogging of a Saturated Porous Medium. *Transport in Porous Media*, 112(1), 265–282. <http://doi.org/10.1007/s11242-016-0644-8>

Mirabolghasemi, M., Prodanović, M., DiCarlo, D., & Ji, H. (2015). Prediction of empirical properties using direct pore-scale simulation of straining through 3D microtomography images of porous media. *J. Hydrol.*, 529(P3), 768–778.

Molnar, I. L., C. S. Willson, D. M. O'Carroll, M. L. Rivers, and J. I. Gerhard (2014), Method for Obtaining Silver Nanoparticle Concentrations within a Porous Medium via Synchrotron X-ray Computed Microtomography, *Environmental Science and Technology.*, 48(2), 1114- 1122.

Molnar, I. L., Johnson, W. P., Gerhard, J. I., Willson, C.S., O'Carroll, D. M., 2015. Predicting colloid transport through saturated porous media: A critical review. *Water Resour. Res.*, 2(7), 1–10.

Muresan, B., Saiyouri N., Guefrech A. Hicher, PY. Internal erosion of chemically reinforced granular materials: A granulometric approach. *Journal of Hydrology*. (2011), Vol : 411, pp : 178-184.

Neukum, C., A. Braun, and R. Azzam (2014), Transport of stabilized engineered silver (Ag) nanoparticles through porous sandstones, *J. Con- tam. Hydrol.*, 158(0), 1–13.

Neuman, S. P., 1984, Adaptive Eulerian-Lagrangian numerical scheme for the dispersion-convection equation using conjugate space-time grids, *J. Comp. Phys.*, 41, 270-294.

D.A. Nield, A. Bejan, *Convection in porous media*, Third ed., Springer, New York, 2006.

Novikov, A. P., S. N. Kalmykov, S. Utsunomiya, R. C. Ewing, F. Horreard, A. Merkulov, S. B. Clark, V. V. Tkachev, and B. F. Myasoedov (2006), Colloid transport of plutonium in the far-field of the Mayak Production Association, Russia, *Science*, 314, 638-641.

O'Carroll, D., B. Sleep, M. Krol, H. Boparai, and C. Kocur (2013), Nanoscale zero valent iron and bimetallic particles for contaminated site remediation, *Adv. Water Resour.*, 51(0), 104–122.

Pazmino, E., Trauscht, J., Dame, B., Johnson, W. P., 2014a. Power law size-distributed heterogeneity explains colloid retention on soda lime glass in the presence of energy barriers. *Langmuir*, 30(19), 5412–5421.

Pazmino, E., Trauscht, J., Johnson, W. P., 2014b. Release of colloids from primary minimum contact under unfavorable conditions by perturbations in ionic strength and flow rate. *Environ. Sci. Technol.*, 48(16), 9227–9235.

Pfannkuch, H.O. (1963). Contribution à l'étude des déplacements de fluides miscibles dans un milieu poreux. *Rev Inst Fr Pétrol* 18 : 215–270

Phenrat, T., H.-J. Kim, F. Fagerlund, T. Illangasekare, R. D. Tilton, and G. V. Lowry (2009), Particle size distribution, concentration, and magnetic attraction affect transport of polymer-modified Fe₀ nanoparticles in sand columns, *Environ. Sci. Technol.*, 43(13), 5079–5085.

Pinder, G. G., and W. G. Gray, 1977, *Finite Elements in Surface and Subsurface Hydrology*, Academic Press, San Diego.

Porubcan, A. A., & Xu, S. (2011). Colloid straining within saturated heterogeneous porous media. *Water Research*, 45(4), 1796–1806.

Priket, T. A., T. G. Naymik, and C. G. Lonquist, 1981, A “random walk” solute transport model for selected groundwater quality evaluations, *Bulletin* 65, Illinois State Water Survey, Champaign. IL.

Quevedo I.R., Tufenkji N. (2009). Influence of solution chemistry on the deposition and detachment kinetics of a CdTe quantum dot examined using a quartz crystal microbalance. *Environ. Sci. Technol.*, 43(9), 3176-3182.

Rasmuson, A., Pazmino, E., Assemi, S., & Johnson, W. P. (2017). Contribution of Nano- to Microscale Roughness to Heterogeneity: Closing the

Gap between Unfavorable and Favorable Colloid Attachment Conditions. *Environmental Science & Technology*, acs.est.6b05911. <http://doi.org/10.1021/acs.est.6b05911>

Raychoudhury, T., G. Naja, and S. Ghoshal (2010), Assessment of transport of two polyelectrolyte-stabilized zero-valent iron nanoparticles in porous media, *J. Contam. Hydrol.*, 118(3–4), 143–151.

Raychoudhury, T., Tufenkji, N., Ghoshal, S., 2014. Straining of polyelectrolyte-stabilized nanoscale zero valent iron particles during transport through granular porous media. *Water Research*, 50, 80–89.

Ren, D., and J. A. Smith (2013), Protein-capped silver nanoparticle transport in water-saturated sand, *J. Environ. Eng.*, 139(6), 781–787.

Redman, J. A., Estes, M. K., Grant, S. B. Resolving macroscale and microscale heterogeneity in pathogen filtration. *Colloids Surf.*, A 2001, 191,57-70.

Ruckenstein E., Prieve D.C. (1976). Adsorption and desorption of particles and their chromatographic separation. *AIChE J.*, 22, 276–283.

Ryan, J. N., and M. Elimelech (1996), Colloid mobilization and transport in groundwater, *Colloids Surf. A*, 107(0), 1–56.

Sane, J. Effect of brownian forces and hydrodynamic interactions on colloids in confined flows. Ph.D Dissertation, University of Cambridge, Queen's College, 2005.

Saiers JE, Hornberger GM, Liang L. First- and second- order kinetics approaches for modeling the transport of colloidal particles in porous media. *Water Resources Research*. 1994;30:2499-506.

Sayler, G.S., Ripp, S., 2000. Field applications of genetically engineered microorganisms for bioremediation processes. *Curr. Opin. Biotechnol.* 11, 286-289.

Schafer, A., H. Harms, and A. J. B. Zehnder (1998), Bacterial accumulation at the air-water interface, *Environ. Sci. Technol.*, 32, 3704–3712.

Schets, F.M., During, M., Italiaander, R., Heijnen, L., Rutjes, S.A., van der Zwaluw, W.K., de Roda Husman, A.M., 2005. *Escherichia coli* O157:H7 in drinking water from private water supplies in The Netherlands. *Water Res.* 39, 4485-4493.

Sen, T. K., and K. C. Khilar (2006), Review on subsurface colloids and colloid-associated contaminant transport in saturated porous media, *Adv. Colloid Interface Sci.*, 119(2–3), 71–96.

Shang, J., M. Flury, G. Chen, and J. Zhuang (2008), Impact of flow rate, water content, and capillary forces on in situ colloid mobilization during infiltration in unsaturated sediments, *Water Resour. Res.*, 44, W06411

Shapiro, A. A., & Bedrikovetsky, P. G. (2010). A stochastic theory for deep bed filtration accounting for dispersion and size distributions. *Physica A: Statistical Mechanics and Its Applications*, 389(13), 2473–2494.

Shellenberger and B.E. Logan: Effect of molecular scale roughness of glass beads on colloidal and bacterial deposition. *Environmental Science and Technology*, 36(2):184–189, 2002.

Shen, C., Wang, L.-P., Li, B., Huang, Y., Jin, Y., 2012. Role of Surface Roughness in Chemical Detachment of Colloids Deposited at Primary Energy Minima. *Vadose Zone J.*, 11(1).

Shen, C., Jin, Y., Li, B., Zheng, W., Huang, Y., 2014. Facilitated attachment of nanoparticles at primary minima by nanoscale roughness is susceptible to hydrodynamic drag under unfavorable chemical conditions. *Science of the Total Environment*, 466–467, 1094–1102.

Srivithayapakorn S, Keller A. Transport of colloids in saturated porous media: A pore-scale observation of the size exclusion effect and colloid acceleration. *Water Resources Research*. 2003;39.

Sun, Y., Gao, B., Bradford, S. A., Wu, L., Chen, H., Shi, X., & Wu, J. (2015). Transport, retention, and size perturbation of graphene oxide in saturated porous media: Effects of input concentration and grain size. *Water Res.*, 68, 24–33.

Suresh, L., Walz, J.Y., 1996. Effect of surface roughness on the interaction energy between a colloidal sphere and a flat plate. *J. Colloid Interface Sci.*, 183 (1), 199–213.

Taghavy, A., A. Mittelman, Y. Wang, K. D. Pennell, and L. M. Abriola (2013), Mathematical modeling of the transport and dissolution of citrate-stabilized silver nanoparticles in porous media, *Environ. Sci. Technol.*, 47(15), 8499–8507.

Tang, X. Y., & Weisbrod, N. (2009). Colloid-facilitated transport of lead in natural discrete fractures. *Environmental Pollution*, 157(8–9), 2266–2274.

Tompson, A. F. B., and Gelhar, 1990, Numerical simulation of solute transport in three-dimensional, randomly heterogeneous porous media, *Water Resour. Res.*, 26(10), 2541-2562.

Tong, M., Johnson, W. P., 2006. Excess Colloid Retention in Porous Media as a Function of Colloid Size, Fluid Velocity, and Grain Angularity. *Environ. Sci. Technol.*, 40(24), 7725–7731.

Tong, M., Ma, H., Johnson, W.P., 2008. Funneling of flow into grain-to-grain contacts drives colloid-colloid aggregation in the presence of an energy barrier. *Environ. Sci. Technol.*, 42(8), 2826–2832.

Torkzaban, S., Tazehkand, S. S., Walker, S. L., Bradford, S. A., 2008. Transport and fate of bacteria in porous media: Coupled effects of chemical conditions and pore space geometry. *Water Resour. Res.*, 44(4), 3(1–12).

Torkzaban, S., Bradford, S. A., Vanderzalm, J. L., Patterson, B. M., Harris, B., Prommer, H. 2015. Colloid release and clogging in porous media: Effects of solution ionic strength and flow velocity. *J. Contam. Hydrol.*, 181, 161–171.

Torkzaban, S., Bradford, S. A., 2016. Critical role of surface roughness on colloid retention and release in porous media. *Water research*, 2016, vol. 88, p. 274-284.

Tosco, T., M. Petrangeli Papini, C. Cruz Viggi, and R. Sethi (2014), Nanoscale zerovalent iron particles for groundwater remediation: a review, *J. Cleaner Prod.*, 77(0), 10–21.

N. Tufenkji, J.A. Redman, M. Elimelech, Interpreting deposition patterns of microbial particles in laboratory-scale column experiments, *Environmental Science & Technology* 37 (3) (2003) 616–623

Tufenkji, N., Miller, G. F., Ryan, J. N., Harvey, R. W., Elimelech, M., 2004. Transport of *Cryptosporidium* oocysts in porous media: Role of straining and physicochemical filtration. *Environ. Sci. Technol.*, 38(22), 5932–5938.

Tufenkji, N., Elimelech, M., 2004. Correlation equation for predicting single-collector efficiency in physicochemical filtration in saturated porous media. *Environ. Sci. Technol.*, 38, 529-536

Tufenkji, N., & Elimelech, M. (2005a). Breakdown of Colloid Filtration Theory: Role of the Secondary Energy Minimum and Surface Charge Heterogeneities. *Langmuir*, 21(18), 841–852.

Tufenkji, N., & Elimelech, M. (2005b). Spatial distributions of *Cryptosporidium* oocysts in porous media: evidence for dual mode deposition. *Environ. Sci. Technol.*, 39(10), 3620–3629.

Tufenkji, N., 2007. Modeling microbial transport in porous media: Traditional approaches and recent developments. *Adv. Water Resour.*, 30(6–7), 1455–1469.

Van Genuchten, M. T. (1981). Analytical solutions for chemical transport with simultaneous adsorption, zero-order production and first-order decay. *Journal of Hydrology*, 49(3–4), 213–233.

van Loosdrecht, M. C. M., J. Lyklema, W. Norde, G. Schraa, and A. J. B. Zehnder (1987a), Electrophoretic mobility and hydrophobicity as a measure to predict the initial steps of bacterial adhesion, *Appl. Environ. Microbiol.*, 53, 1898–1901.

van Loosdrecht, M. C. M., J. Lyklema, W. Norde, G. Schraa, and A. J. B. Zehnder (1987b), The role of bacterial cell wall hydrophobicity in adhesion, *Appl. Environ. Microbiol.*, 53, 1893–1897.

Verwey, E. J. W., and J. T. G. Overbeek (1948), *Theory of the Stability of Lyophobic Particles*, Elsevier, Amsterdam, Netherlands.

Vieira, C. M. F., da Silva, P. R. N., da Silva, F. T., Capitaneo, J. L. and Monteiro, S. N. (2005), Microstructural Evaluation and Properties of a Ceramic Body for Extruded Floor Tile, *Revista Materia*, 10, 526-536.

Vigeant, M. A. S., R. M. Ford, M. Wagner, and L. K. Tamm (2002), Reversible and irreversible adhesion of motile *Escherichia coli* cells analyzed by total internal reflection aqueous fluorescence microscopy, *Appl. Environ. Microbiol.*, 68, 2794–2801.

Walker, S. L., J. A. Redman, and M. Elimelech (2004), Role of cell surface lipopolysaccharides in *Escherichia coli* K12 adhesion and transport, *Langmuir*, 20, 7736–7746.

Wang, C., A. D. Bobba, R. Attinti, C. Shen, V. Lazouskaya, L.-P. Wang, and Y. Jin (2012), Retention and transport of silica nanoparticles in saturated porous media: Effect of concentration and particle size, *Environ. Sci. Technol.*, 46(13), 7151–7158.

Wang D, Su C, Liu C, Zhou D. Transport of fluorescently labeled hydroxyapatite nanoparticles in saturated granular media at environmentally relevant concentrations of surfactants. *Colloids and Surfaces A: Physicochemical and Engineering Aspects*. 2014;457:58-66.

Wang, H. Q., & Lacroix, M. (1997). Optimal weighting in the finite difference solution of the convection-dispersion equation. *Journal of Hydrology*, 200, 228–242.

Wang, H., Alem, A., Wang, H.Q., & Beaudoin, A. (2014). Numerical modeling of deposition-release mechanisms in long-term filtration: Validation from experimental data. *Comptes Rendus - Mecanique*, 342(12), 739–746.

Wang, Z., Jin, Y., Shen, C., Li, T., Huang, Y., Li, B., 2016. Spontaneous detachment of colloids from primary energy minima by brownian diffusion. *PLoS ONE*, 11(1), 1–21.

Xie J, Lu J, Lin J, Zhou X, Xu Q, Li M, et al. Insights into transport velocity of colloid-associated plutonium relative to tritium in porous media. *Scientific reports*. 2014;4.

Xu, S., Gao, B., Saiers, J. E., 2006. Straining of colloidal particles in saturated porous media. *Water Resour. Res.*, 42(12), 1–10.

Xu, S., Liao, Q., Saiers, J. E., 2008. Straining of nonspherical colloids in saturated porous media. *Environ. Sci. Technol.*, 42(3), 771–778.

Xu, S., Saiers, J. E., 2009. Colloid straining within water-saturated porous media: Effects of colloid size nonuniformity. *Water Resour. Res.*, 45(5), 2–9.

Yang, X., Zhang, Y., Chen, F., Yang, Y., 2015. Interplay of Natural Organic Matter with Flow Rate and Particle Size on Colloid Transport: Experimentation, Visualization, and Modeling. *Environ. Sci. Technol.*, 49(22), 13385–13393.

Yao, K.M., Habibian, M. T., C. R. O'Melia C. R., 1971. Water and waste water filtration. Concepts and applications, *Environ. Sci. Technol.*, 5(11), 1105–1112.

Yeh, G. T., 1990, A Lagrangian-Eulerian method with zoomable hidden fine-mesh approach to solving advection-dispersion equations, *Water Resour. Res.*, 26(6), 1133-1144.

Yin, X., Gao, B., Ma, L.Q., Saha, U.K., Sun, H., Wang, G., 2010. Colloid-facilitated Pb transport in two shooting-range soils in Florida. *J. Hazard. Mater* 177, 620e625.

Yoon, J. S., Germaine, J. T., Culligan, P. J., 2006. Visualization of particle behavior within a porous medium: Mechanisms for particle filtration and retardation during downward transport. *Water Resour. Res.*, 42(6), 1–16.

Yuan, H., & Shapiro, A. A. (2010). Modeling non-Fickian transport and hyperexponential deposition for deep bed filtration. *Chemical Engineering Journal*, 162(3), 974–988.

Yuan, H., You, Z., Shapiro, A., & Bedrikovetsky, P. (2013). Improved population balance model for straining-dominant deep bed filtration using network calculations. *Chemical Engineering Journal*, 226, 227–237.

Indices

List of figures

Figure 1.1 Diagram of generalized divisions of subsurface groundwater.....	9
Figure 1.2 Diagram of different types of aquifers (Water Cycle and Fresh Water Supply).....	12
Figure 1.3 Porosity and Representative elementary volume.....	13
Figure 1.4 Diagram of porous medium tortuosity.....	15
Figure 1.5 Pore size distribution measured by mercury porosimetry (Vieira et al., 2005).....	16
Figure 1.6 Particle size ranges of bio- and nonbiological particles present in groundwater....	18
Figure 1.7 Diagram of different types of mechanical dispersion in porous media.....	21
Figure 1.8 Schematic showing the different regimes of a miscible displacement flow (Adapted by Pfannkuch, 1963).....	23
Figure 1.9 Diagram of different filtration types.....	24
Figure 1.10 Diagram of different types of retention sites.....	26
Figure 1.11 Interaction energy profiles of the function of separation distance between particle and collector surface.....	29
Figure 1.12 Dominant transport mechanisms of particles to the collector surface.....	30
Figure 1.13 BTCs and retention profiles under favorable and unfavorable conditions.....	33
Figure 1.14. Schematic illustration of different deposition mechanisms under unfavorable deposition conditions.....	36
Figure. 1.15 BTCs and retention profiles under unfavorable conditions.....	44
Figure 2.1 (a) Breakthrough curves of tracer and particle; (b) Average velocity distribution of tracer and particle.....	50
Figure 2.2 Discrete grid points.....	55
Figure 2.3 (a) An explicit finite-difference module; (b) an implicit finite-difference module; (c) A finite-difference module of Crank-Nicolson method.....	58
Figure 2.4 Comparisons of the exact and numerical solutions of a one-dimensional transport with a boundary condition of a continuous injection with (a) a low Peclet number ($P_e^{num} = 2$) and (b) a high Peclet number ($P_e^{num} = 25$).....	62
Figure 2.5 Flow chart of inverse method algorithm.....	68
Figure 2.6. (a) The squared errors as a function of kd and kr . (b) Top: the convergence of the parameters with each iteration, (b) Bottom: values of χ^2 and λ each iteration. (c) Top: Measured data C , curve-fit \hat{C} , curve-fit+error, and curve-fit-error; (c) Bottom: standard error of the fit, $\sigma_{\hat{C}}$. (d) Histogram of the errors between the data and the fit.....	70
Figure 3.1 Pulse input of latex suspension experimental set-up.....	76
Figure 3.2. Extended-DLVO Interaction energy profiles for all tested particles as functions of the separation distance between the particle and grain: (Φ_{min}) is the interaction energy	

associated with the primary minimum (Φ_{1min}) or the second minimum (Φ_{2min}), (Φ_{max}) is the interaction energy associated with the energy barrier.....77

Figure 3.3 BTCs at different fluid velocities of (a) 3 μm , (b) 10 μm , (c) 16 μm , and (d) MIX (3, 10 and 16 μm). C_r is the relative particle concentration in effluent, expressed as $C_r = \frac{C_e \cdot V_p}{m}$. Where, C_e is particle concentration in effluent, V_p is the pore volume equal to the product of the sand column volume and the porous medium porosity, m is the total injected particle mass.

.....79

Figure 3.4 BTCs of different-sized and mixed particles at U=U1 (a) and U=U3 (b).....79

Figure 3.5. A plot of fitted irreversible deposition rate ($k_{d,irr}$) (a) and reversible deposition ($k_{d,r}$) and re-entrainment ($k_{r,r}$) rate values (b) of different-sized and mixed particles as a function of fluid velocity.....81

Figure 3.6 Schematic illustration of particle behaviors and torques and forces exerted on the particles in fluid stagnation zones, near-surface and grain-to-grain contact. h_{2min} , h_{1min} and h_r represent separately the distance corresponding to the local secondary energy minimum, the distance corresponding to the local primary energy minimum and the height of roughness; T_h , T_{att} represent hydrodynamic and attachment (primary minimum) adhesive torques; F_h , F_{att} , F_{2min} represent hydro dynamic, attachment (primary minimum) and 'non-contact' (secondary minimum) adhesive forces (Modified from Bradford et al., 2013, Darbha et al., 2012, Johnson and Hilpert, 2013).....83

Figure 3.7. Comparison of irreversible deposition rate ($k_{d,irr}$) values of different-sized particles in monodisperse experiments and in polydisperse experiments. 3 μm /MIX means the 3 μm particle in the tridisperse particle.....87

Figure 3.8. Illustrations of 3 μm particle behaviors near grain-to-grain contact of (a) without and (b) with retained 10 and 16 μm particles. U_{bulk} represents the bulk fluid velocity.....89

Figure 3.9 Step input of kaolinite particle suspension experimental set-ups.....91

Figure 3.10. Extended-DLVO Interaction energy profiles for kaolinite particles with characteristic diameters of d_{10} , d_{50} and d_{90} as functions of the separation distance between the particle and grain: (Φ_{min}) is the interaction energy associated with the primary minimum (Φ_{1min}) or the second minimum (Φ_{2min}), (Φ_{max}) is the interaction energy associated with the energy barrier.....92

Figure 3.11 Effluent breakthrough curves (a) and retention profiles (b) at the Darcy velocity of U4 in the Coarse sand column. Simulations with constant deposition rate (dashed line) are contrasted against those with time-distance-dependent deposition rate (solid line).....97

Figure 3.12. Observed and simulated effluent breakthrough curves and retention profiles of the Coarse, Fine and MIX sand at Darcy velocities of U1 (a,b) and U4 (c,d).....99

Figure 3.13 Plots of fitted values of a) the initial deposition rate (k_0), b) the single-collector contact efficiency for the Coarse sand, and c) the sticking efficiency of different porous media as a function of fluid velocity.....102

Figure 3.14 PSD of the particles in the effluent at 3 pore volumes: (a) with different Darcy velocities of Coarse sand and in different porous media at (b) U1 and (c) U4.....105

Figure 3.15 Evolution of the deposition rate with time in the Coarse sand column at the Darcy velocity of U1.....108

Figure 3.16 Evolution of the deposition rate with time in the Coarse sand column at the Darcy velocity of U1.....109

Figure 3.17 Retention distribution with particle size of the three parts of the sand columns: 0-10 cm (a), 10-30 cm (b) and 30-62 cm (c).111

List of tables

Table 2.1. Parameter values and standard errors.....	69
Table 2.2. Parameter correlation matrix.....	70
Table 3.1 Optimal Parameter Values Estimated from BTCs of monodisperse and polydisperse particles. M_E (%) refers to percent recovery of injected microspheres via effluent.....	81
Table 3.2 Optimal Parameter Values Estimated from BTCs and Retention. r_e^2 , r_s^2 : coefficients of determination for BTC and retained profile, respectively; the Recovered Effluent (M_E), Sand (M_S) and the Total Particle Mass Fraction (M_T).....	100

List of publications

Journal publications:

1. Ma, E., Ouahbi, T., Wang, H., Ahfir, N.-D., Alem, A., & Hammadi, A. (2017). Modeling of retention and re-entrainment of mono- and poly-disperse particles: Effects of hydrodynamics, particle size and interplay of different-sized particles retention. *Science of The Total Environment*, 596, 222–229.
2. Ma, E., Ouahbi, T., Wang, H., Ahfir, N. D., Alem, A., & Hammadi, A. (2017). Modeling of the transport and deposition of polydispersed particles: Effects of hydrodynamics and spatiotemporal evolution of the deposition rate. *Environmental Pollution*, 1–12.
<http://doi.org/10.1016/j.envpol.2017.11.017>

Conferences presentations:

1. Ma, E., Ouahbi, T., Wang, H., (2016). Modeling of transport and retention of suspended particles in saturated porous media. Oral presentation in English at the 9th International Association of Hydrological Sciences (IAHS) Groundwater Quality Conference, July, 2016, Shenzhen, China.
2. Ma, E., Ouahbi, T., Wang, H., (2016). Modeling of transport and deposition of polydispersed particles: effects of hydrodynamics and grain size distribution. Paper and oral presentation in French at 34ème Rencontres Universitaires de Génie Civil de l'AUGC, May, 2016, Liège, Belgium.

Poster presentations:

1. Modélisation de Transferts de matières dissoutes et particulaires en milieux hétérogènes. Poster presentation at SCALE 2016.
2. Modélisation du transport et du dépôt de particules en suspension dans un milieu poreux saturé. Poster presentation at SCALE 2017.

Abstract

Understanding of particle transport and deposition behavior in porous media is of significant interests in numerous domains, such as subsurface groundwater contamination and soil remediation. In this work, modified models based on the general transport-deposition-reentrainment model are applied to simulating a series column experiments to study the effects of different factors on the particle transport behavior in porous media.

For pulse-input injection experiments of artificial latex particle suspension, numerical simulations of experimental data were performed with constant kinetic rate coefficients to characterize the retention and re-entrainment dynamics under different hydrodynamic conditions for monodisperse and polydisperse latex particles (3, 10, 16 μm and the mixture). The results show that drastic increase in fluid velocity provokes hardly any remarkable decrease in retention in the presence of large energy barriers ($>2000 kT$). Systematical increases in deposition and re-entrainment dynamic rates were observed with fluid velocity and/or particle size. Increased irreversible deposition rate indicates straining and wedging dominate deposition in this study. Excess retention of 3 μm particle in the polydisperse particle suspension was observed. The origins are reckoned that deposited larger particles may hinder the re-entrainment of smaller particles near the grain-to-grain contact and can provide additional sites of attachment.

For step-input injection experiments of natural kaolinite particle suspension, a time-distance-dependent deposition model is built to investigate the effects of hydrodynamic forces on the transport and deposition of polydispersed particles and the evolution of deposition rates with time and distance. Straining and the heterogeneity of the particle population are considered to play important roles in the decreasing distribution of deposition rates. Numerical simulations were applied in a series of sand column experiments at different fluid velocities for three different porous media. The effects of hydrodynamics forces are elaborated with the systematic variations of deposition dynamic parameters of the proposed model. With retention distributions with particle size as well as temporal and spatial evolutions of deposition rates, the transport and deposition mechanisms of polydispersed particles will be elucidated through the interplay of the variation of the particle size distribution of mobile particle populations and the geometrical change of the porous medium due to retention (straining and blocking).

Résumé

La compréhension des mécanismes de transport et de dépôt de particules dans les milieux poreux présente un intérêt important dans de nombreux domaines, tels que la contamination des eaux souterraines et l'assainissement des sols. Dans ce travail, des modèles modifiés basés sur le modèle général de transport-dépôt-relargage ont été développés et appliqués à la simulation numérique d'expériences en colonnes de laboratoire. Ces modèles numériques ont permis d'étudier les effets de différents facteurs sur le comportement de transport de particules dans différents milieux poreux.

Des expériences d'injection instantanée de suspension de particules de latex artificiel ont été modélisées dans la première partie de ce travail. Les simulations numériques du modèle de couplage transport-dépôt ont été réalisées avec des coefficients cinétique de dépôt et de relargage constants. Cela a permis de caractériser la dynamique de rétention et de relargage dans différentes conditions hydrodynamiques pour des particules de latex mono-disperses (de diamètre 3, 10 et 16 μm) et poly-disperses (mélange des trois populations mono-disperses 3, 10 ou 16 μm).

Les résultats montrent qu'une augmentation importante de la vitesse du fluide ne provoque pratiquement aucune diminution notable de la rétention en présence de grandes barrières énergétiques ($> 2000 \text{ kT}$). Des augmentations systématiques des coefficients cinétiques de dépôt et de relargage ont été observées avec la vitesse du fluide et/ou la taille des particules. L'augmentation du cinétique de dépôt irréversible indique que le blocage mécanique (straining et wedging) domine le dépôt dans cette étude. Lors de l'injection de la suspension de particules poly-disperses (mélange des trois populations mono-disperses 3, 10 ou 16 μm) une rétention excessive des particules de taille 3 μm a été observée. Cela peut être expliqué par le fait que les particules plus grosses (10 et 16 μm) déposées peuvent gêner le relargage des plus petites particules (3 μm) à proximité du contact grain-grain et peuvent fournir des sites de fixation supplémentaires à ces particules.

Dans la seconde partie de ce travail, des expériences d'injection continue de particules de kaolinite naturelles ont été modélisées. Un modèle de dépôt dépendant de la distance de parcours des particules a été développé pour étudier les effets des forces hydrodynamiques sur le transport et le dépôt de particules poly-disperses et l'évolution dans l'espace et dans le temps des cinétiques de dépôt. Les résultats obtenus montrent que le blocage mécanique (straining) et l'hétérogénéité de la population de particules jouent un rôle important dans la distribution décroissante, avec la profondeur, du coefficient cinétique de dépôt.

Des simulations numériques ont été appliquées sur une série d'expériences de colonnes de laboratoire. Différentes vitesses de fluides et trois milieux poreux de granulométries différentes ont été considérées. Les effets des forces hydrodynamiques ont été analysés à partir des variations des paramètres de dépôt du modèle proposé. En tenant compte des distributions de la rétention, de la distribution des tailles des particules retenues dans le milieu à différentes profondeurs ainsi que des évolutions spatio-temporelles des coefficients cinétique de dépôt, les mécanismes de transport et de dépôt des particules poly-disperses ont été expliqués et clarifiés. Les rôles importants de la variation de la distribution granulométrique des populations de particules mobiles et du changement géométrique des porosités du milieu poreux dû à la rétention ont été soulignés.